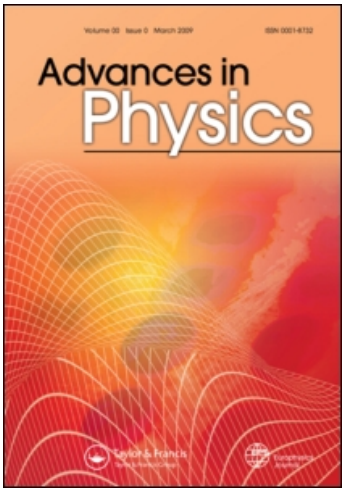

Advances in Physics
Publication details, including instructions for authors and subscription information:
http://www.informaworld.com/smpp/title~content=t713736250

Properties of graphene: a theoretical perspective

D. S. L. Abergel[a]; V. Apalkov[b]; J. Berashevich[a]; K. Ziegler[c]; Tapash Chakraborty[a]
[a] Department of Physics and Astronomy, University of Manitoba, Winnipeg, MB R3T 2N2, Canada [b] Department of Physics and Astronomy, Georgia State University, Atlanta, GA 30303, USA [c] Institut für Physik, Universität Augsburg, D-86135 Augsburg, Germany

Online publication date: 03 August 2010

To cite this Article Abergel, D. S. L. , Apalkov, V. , Berashevich, J. , Ziegler, K. and Chakraborty, Tapash(2010) 'Properties of graphene: a theoretical perspective', Advances in Physics, 59: 4, 261 — 482
To link to this Article: DOI: 10.1080/00018732.2010.487978
URL: http://dx.doi.org/10.1080/00018732.2010.487978

Advances in Physics
Vol. 59, No. 4, July–August 2010, 261–482

Taylor & Francis
Taylor & Francis Group

RESEARCH ARTICLE

Properties of graphene: a theoretical perspective

D.S.L. Abergel[a], V. Apalkov[b], J. Berashevich[a], K. Ziegler[c] and Tapash Chakraborty[a]*

[a]*Department of Physics and Astronomy, University of Manitoba, Winnipeg, MB R3T 2N2, Canada;* [b]*Department of Physics and Astronomy, Georgia State University, Atlanta, GA 30303, USA;* [c]*Institut für Physik, Universität Augsburg, D-86135 Augsburg, Germany*

(*Received 17 November 2009; final version received 8 April 2010*)

The electronic properties of graphene, a two-dimensional crystal of carbon atoms, are exceptionally novel. For instance, the low-energy quasiparticles in graphene behave as massless chiral Dirac fermions which has led to the experimental observation of many interesting effects similar to those predicted in the relativistic regime. Graphene also has immense potential to be a key ingredient of new devices, such as single molecule gas sensors, ballistic transistors and spintronic devices. Bilayer graphene, which consists of two stacked monolayers and where the quasiparticles are massive chiral fermions, has a quadratic low-energy band structure which generates very different scattering properties from those of the monolayer. It also presents the unique property that a tunable band gap can be opened and controlled easily by a top gate. These properties have made bilayer graphene a subject of intense interest. In this review, we provide an in-depth description of the physics of monolayer and bilayer graphene from a theorist's perspective. We discuss the physical properties of graphene in an external magnetic field, reflecting the chiral nature of the quasiparticles near the Dirac point with a Landau level at zero energy. We address the unique integer quantum Hall effects, the role of electron correlations, and the recent observation of the fractional quantum Hall effect in the monolayer graphene. The quantum Hall effect in bilayer graphene is fundamentally different from that of a monolayer, reflecting the unique band structure of this system. The theory of transport in the absence of an external magnetic field is discussed in detail, along with the role of disorder studied in various theoretical models. Recent experminental observations of a metal–insulator transition in hydrogenated graphene is discussed in terms of a self-consistent theory and compared with related numerical simulations. We highlight the differences and similarities between monolayer and bilayer graphene, and focus on thermodynamic properties such as the compressibility, the plasmon spectra, the weak localization correction, quantum Hall effect and optical properties. Confinement of electrons in graphene is non-trivial due to Klein tunnelling. We review various theoretical and experimental studies of quantum confined structures made from graphene. The band structure of graphene nanoribbons and the role of the sublattice symmetry, edge geometry and the size of the nanoribbon on the electronic and magnetic properties are very active areas of research, and a detailed

*Corresponding author. Email: tapash@physics.umanitoba.ca

ISSN 0001–8732 print/ISSN 1460–6976 online

DOI: 10.1080/00018732.2010.487978
http://www.informaworld.com

review of these topics is presented. Also, the effects of substrate interactions, adsorbed atoms, lattice defects and doping on the band structure of finite-sized graphene systems are discussed. We also include a brief description of graphane – gapped material obtained from graphene by attaching hydrogen atoms to each carbon atom in the lattice.

Keywords: monolayer graphene; bilayer graphene; Dirac fermions; quantum Hall effect; electron-electron interaction; plasmon dispersion; zero-field transport; metal-insulator transition; quantum dots; graphene nanoribbons; edge-states; graphane

Contents

1. Introduction

Everything about graphite involves a mix of the very old and very young. Known to man since ancient times (*ca* 1500CE), graphite is as ubiquitous as the *lead* in a pencil, and yet the subject of our current review, graphene, being a single atomic layer of graphite, was isolated only in 2004! That discovery marked the beginning of the academic equivalent of a gold rush which has become a major topic of research for the condensed matter and materials physics community, along with chemists, electrical engineers and device specialists. Several thousand papers have been written in the past couple of years that have attempted to explain every aspect of the electronic properties of graphene. There are review articles, long and short (see, e.g. [1–5]), special journal issues [6] and popular magazine articles (see, e.g. [7]). This development at 'Mozartian speed' is primarily due to the fact that a two-dimensional system of electrons in graphene behaves rather uniquely as compared to its counterpart in semiconductor systems. In fact, many of the fundamental properties of graphene that were crucial for the present developments were already reported in the early part of the past century, merely waiting to be confirmed experimentally until now.

In graphene, one finds a new class of low-dimensional system, only one atom thick, with vast potential for applications in future nanotechnology. Our review is organized as follows. In this section, we introduce graphene by describing its crystal structure, and discussing its band structure via the frequently-used tight-binding model. We also discuss the low-energy properties of this material, and in particular we focus on the linear (Dirac-like) nature of the energy dispersion near the edges of the Brillouin zone, and on the chiral nature of the low-energy electrons. We also briefly discuss fabrication techniques for graphene, and whet the appetite for study of this material by describing some of the devices utilizing the unique properties of graphene which have already been created in the laboratory.

Section 2 deals with the quantum Hall effect, i.e. quantization of Hall conductance as a function of the magnetic field or the electron density, that was initially discovered in conventional non-relativistic two-dimensional electron systems. The effect is a direct manifestation of the Landau quantization of electron dynamics. An electron system in graphene, being a two-dimensional system, also

shows Landau quantization of electron motion and the corresponding quantum Hall effect, which has been observed experimentally. The relativistic massless nature of the energy dispersion law in graphene results in striking differences between the quantum Hall effect observed in graphene and in conventional two-dimensional systems. In graphene, the quantum Hall effect can be observed even at room temperature, while in non-relativistic systems it is observable only at low temperatures. The quantized Hall effect in graphene occurs not at integer values as in the conventional Hall effect, but at half-integer values. Such anomalous behavior of the quantum Hall effect is due to massless relativistic nature of the charge carrier dispersion and the electron–hole symmetry of the system. In addition to anomalous half-integer values of the Hall conductance, a rich structure of Hall plateaus has been observed experimentally. This structure is associated with the lifting of valley and spin degeneracy of the Landau levels. Different many-body mechanisms of lifting of the degeneracy of the Landau levels have been proposed in the literature. These mechanisms are reviewed in detail. The specific features of the many-particle excitations of the quantum Hall states, the fractional quantum Hall effect in graphene and the unique structure of the quantum Hall state edge states are also discussed in this article.

In Section 3, we discuss specific aspects of bilayer graphene, and try to highlight the similarities and differences between this and the monolayer material. We introduce experimental techniques for distinguishing the number of layers in a graphene flake. We present the tight-binding formalism in order to derive the quadratic low-energy spectrum, and to discuss the influence of trigonal warping and the formation of a band gap. We describe the quantum Hall effect and the formation of the zero-energy level with doubled degeneracy, which is unique to this system. The interactions between electrons are fascinating in this material, and several properties are distinct from both the monolayer and traditional two-dimensional electron systems, and we describe the formation of spin-polarized and other ordered states. The interactions between electrons and phonons are also important (e.g. in the context of Raman scattering experiments), so we briefly describe the phonon anomalies and the electron–phonon interaction. Lastly, we review some of the proposals for devices which utilize bilayer graphene in their design.

Electronic properties that are intimately related to electron–electron interactions, namely, the compressibility and plasmon dispersion in a two-dimensional electron gas shows unique behavior in graphene. The compressibility of a two-dimensional electron gas is an important physical quantity which can be deduced from the ground state energy. It provides important information about the electron correlations, the chemical potential, the stability of the system, and so on. In Section 4, we discuss the unique behavior of the electron compressibility in monolayer and bilayer graphene. In that section, we also describe the excitation spectra of graphene in the presence of the spin–orbit interaction (SOI) within the random-phase approximation (RPA). The SOI opens a gap between the valence and conduction bands and between the intraband and inter-band electron–hole excitation continuum (EHC) of the semimetal Dirac system. As a result, one sees a dramatic change in the long-wavelength dielectric function of the system. An undamped plasmon mode appears in the EHC gap reflecting the interplay between the intraband and interband electron

correlations. In undoped bilayer graphene, the static screening effect is anisotropic and much stronger than that in monolayer graphene. The dynamic screening shows the properties of a Dirac gas in the low-frequency limit and of Fermi gas in the high-frequency limit. A similar transition from the Dirac gas to the Fermi gas is also observed in the plasmon spectrum. In doped bilayer graphene, the plasmon spectrum is quite similar to that of Fermi gas for momentum less than half the Fermi momentum while becoming softer at higher momentum. We close this section with a discussion of the properties of graphene in a strong external electromagnetic field (EMF). The possibility of inducing valley-polarized currents by irradiating gapped bilayer graphene is described.

In Section 5, we review the transport behavior of monolayer and bilayer graphene in the absence of an external magnetic field, focusing on properties in the vicinity of the charge neutrality points. Beginning with the classical Boltzmann approach, we compare the latter with the more general linear-response (Kubo) approach. The effect of electron–electron and electron–phonon interactions as well as the effect of different types of disorder are discussed. Of all these effects, disorder seems to be the most important. We present and compare several schemes of approximation: perturbation theory, self-consistent and saddle-point approximations and numerical simulations. Finally, the properties of a random gap and a related metal–insulator transition are investigated.

Quantum dots (QDs) or *artificial atoms* [8,9] are crucial building blocks in many nanoscale semiconductor applications. Their unique properties, such as superior transport and tunable optical spectra, originate from their zero dimensionality, which results in discrete energy spectra and sharp density of states. In conventional 'non-relativistic' semiconductor systems, the natural way to realize nanoscale QDs is through a confinement potential or as nanoscale islands of semiconductor material. In both cases the QDs have discrete energy spectra and electrons are localized within the QD regions. In graphene, the massless relativistic nature of the dispersion law results in unique properties of graphene QDs. That is, the above two approaches of the realization of QDs have very different outcomes in graphene. While the QDs as isolated islands of graphene have been successfully realized experimentally and have all the properties of zero-dimensional systems with discrete energy spectra, the conventional QDs realized through the confinement potential do not exist in graphene. This is due to Klein's tunnelling, which provides an efficient escape channel from a confinement potential of any strength. Therefore electrons in graphene cannot be localized by a confinement potential. Different approaches have been proposed to overcome this problem: generation of an electron effective mass through interaction with a substrate, introducing a confinement potential in a double-layer system, in which electrons have non-zero mass under applied gate voltage, or considering special types of confinement potentials, e.g. smooth cylindrically symmetric potentials, for which not the problem of localization but the problem of efficient electron trapping is discussed. In Section 6, we review different approaches to overcome the Klein's tunnelling and realize graphene QDs through a confinement potential. Even for QDs realized as islands of materials, the graphene islands show some unique properties. Although the main manifestations of a two-dimensional quantization, such as the Coulomb blockade and discrete energy spectra, are observed in experiments, the graphene nanoscale islands show specific

features. Such features are degenerate zero-energy edge states with unique magnetic properties, specific energy level statistics related to the Dirac billiard and so on. These special properties of nanoscale graphene islands are also discussed. Finally, we also present a brief review of QDs in bilayer graphene.

In Section 7, we review the band structure of graphene nanoribbons which is known to be modified by the presence of edges where the alteration of the sp^2 network due to the mixture of the sp and sp^2 hybridization occurs. The nature of the zigzag edges impose localization of the electron density with the maximum at the border carbon atoms leading to the formation of flat conduction and valence bands near the Fermi level when the wave vector, $k \geq 2\pi/3$. The localized states are spin-polarized and in the case of ordering of the electron spin along the zigzag edges, graphene can be established in ferromagnetic or antiferromagnetic phases. The antiferromagnetic spin ordering of the localized states at the opposite zigzag edges breaks the sublattice symmetry of graphene that changes its band structure and opens a gap. Because the energetics, localization and spin ordering of the edge states can be modified by the size of graphene nanoribbon, edge geometry, orbital hybridization at the edges and an external electric field, their influence on the electronic and magnetic properties of graphene are discussed. Finally, we turn to finite-sized bilayer graphene systems, e.g. nanoribbons, and describe how the confinement and edge structures affect the properties of this system.

Graphene in the real world would interact with a substrate and the surrounding environment. If these interactions cause an imbalance of the charge or spin distribution between graphene sublattices or modify the graphene lattice, the sublattice or lattice symmetry of graphene will be broken, resulting in a change of the electronic and magnetic properties of the graphene. The edges of graphene are chemically active and prone to structural modifications and interactions with gas dissolved in the environment, thereby influencing the properties of graphene as well. Therefore, in Section 8, we discuss the influence of the changes brought by the external sources into the electronic and magnetic properties of graphene and prospects of their manipulation in a controllable way.

1.1. *A sheet of molecular chicken wire*

Graphene can be considered as the building block of many carbon allotropes. It is a two-dimensional crystal with hexagonal structure consisting of a bipartite lattice of two triangular sublattices (Figure 1a). Each atom is tied to its three nearest neighbors via strong σ bonds that lie in the graphene plane with angles of 120°. The σ bond is a result of the sp^2 hybridization of the 2s, $2p_x$, and $2p_y$ orbitals for the three valence electrons. The fourth valence electron is in the $2p_z$ orbital that is orthogonal to the graphene plane. A weak π bond is formed by the overlap of half-filled $2p_z$ orbitals with other $2p_z$ orbitals. The transport properties of graphene are determined by these delocalized π electrons.

The crystal structure of graphite consists of layers of graphene, with strong intralayer covalent coupling and weak interlayer binding. The weak interlayer coupling supposedly arises due to van der Waals interaction (the separation between the adjacent layers (0.34 nm) is much larger than the nearest neighbor distance

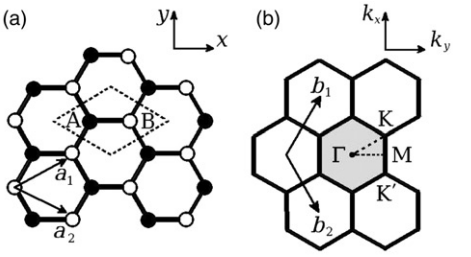

Figure 1. (a) Graphene lattice in real space, and (b) the corresponding reciprocal lattice. The unit cell of graphene contains two atoms A and B. The first Brillouin zone is drawn as shaded hexagon. The basis vectors of the direct lattice and the reciprocal lattice are a_i and b_i, $i = 1, 2$, respectively. The high-symmetry points Γ, M and K in the Brillouin zone are also indicated.

between two carbon atoms ($a_{cc} = 0.142$ nm)) and the particular bonding mechanism along the direction normal to the plane. Similarly, if a graphene sheet is rolled up along one axis, it forms a carbon nanotube and it can be formed into a ball to create a fullerene. Due to this, graphene has long been considered a starting point for band structure calculations of graphite [10] and carbon nanotubes, and also for the calculation of their magnetic properties [11,12]. In what follows, we shall present a very brief description of the band structure. A detailed description can be found, for example in [13,14].

As mentioned above, graphene is a honeycomb lattice of carbon atoms. It is a bipartite lattice with two sublattices A and B that are triangular Bravais lattices (Figure 1a). Considering only the xy plane, the unit vectors in real space, $\vec{a}_1$ and $\vec{a}_2$, and the reciprocal lattice vectors $\vec{b}_1$ and $\vec{b}_2$ are shown in Figure 1. The real space lattice vectors are written as

$$\vec{a}_1 = \frac{a}{2}\left(\sqrt{3}, 1\right), \quad \vec{a}_2 = \frac{a}{2}\left(\sqrt{3}, -1\right),$$

where $a = |\vec{a}_1| = |\vec{a}_2| = 0.246$ nm is the lattice constant. The corresponding unit vectors in the reciprocal lattice are

$$\vec{b}_1 = \frac{2\pi}{a}\left(\frac{1}{\sqrt{3}}, 1\right), \quad \vec{b}_2 = \frac{2\pi}{a}\left(\frac{1}{\sqrt{3}}, -1\right),$$

with a reciprocal space lattice constant $4\pi/\sqrt{3}a$. The first Brillouin zone is a hexagon (Figure 1b), where the corners are called the K points. The six corners form two inequivalent groups of K points, traditionally labelled K and K′.

The energy dispersion of π electrons in graphene was first derived in 1947 by Wallace [10] within the tight-binding approximation. In this case, the wave function of graphene is a linear combination of Bloch functions for sublattice A

$$\Phi_A = \frac{1}{\sqrt{N}} \sum_{\vec{R}_A} e^{i\vec{k}\cdot\vec{R}_A} \varphi(\vec{r} - \vec{R}_A),$$

and an equivalent function Φ_B for the B sublattice. Here N is the number of unit cells, $\vec{R}_A$ are the positions of the atom A and $\varphi(\vec{r} - \vec{R}_A)$ is the $2p_z$ orbital of the atom at $\vec{R}_A$. The sum runs over all unit cells, i.e. all possible lattice vectors.

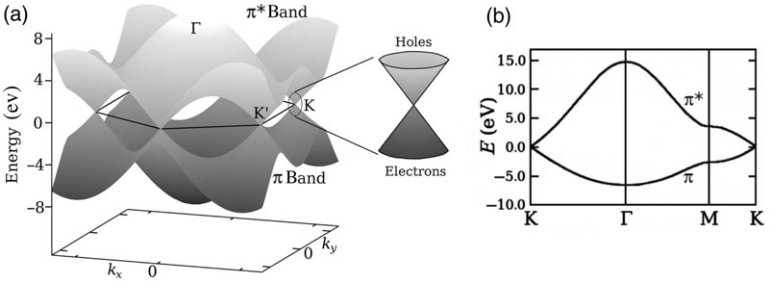

Figure 2. (a) Energy dispersion relation for graphene, drawn in the entire region of the Brillouin zone. Since we ignore the coupling between the graphene sheets, the bands depend only on k_x and k_y. The π band is completely filled and meets the totally empty π^* band at the K points. Near these points both bands have linear dispersion as described in the text. (b) The dispersion along the high-symmetry points ΓMK.

In the nearest neighbor approximation (every A site has three nearest B sites, and vice versa), the energy eigenvalues can be obtained in a closed form [13,14]

$$\mathcal{E}(k_x, k_y) = \pm\gamma_0\left[1 + 4\cos\frac{\sqrt{3}k_x a}{2}\cos\frac{k_y a}{2} + 4\cos^2\frac{k_y a}{2}\right]^{\frac{1}{2}}, \tag{1}$$

where γ_0 is the transfer integral between the nearest neighbors. The energy dispersion of two-dimensional graphene according to this formula is plotted in Figure 2(a) as a function of the wave vector $\vec{k}$. The upper half of the curves is called the π^* or the anti-bonding band while the lower one is π or the bonding band. The two bands degenerate at the two K points given by the reciprocal space vectors $\vec{K} = (2\pi/a)(1/3, 1/\sqrt{3})$ and $\vec{K'} = (2\pi/a)(-1/3, 1/\sqrt{3})$ points where the dispersion vanishes. This is also the Fermi energy level E_F in intrinsic (undoped) graphene. There are two atoms per unit cell and hence there are two electrons per unit cell. The lower π band is therefore completely filled, which leaves the upper π^* band completely empty.

The derivation of this formula neglected the overlap integral between electron orbitals on adjacent lattice sites. Restoring this additional parameter introduces an electron–hole asymmetry to the π bands away from the K points. This is shown in Figure 2(b) for parameters quoted in [13].

A full description of the band structure in graphene should also include the consideration of the σ bands, since they are the lowest energy bands near the center of the Brillouin zone. However, since most transport properties of bulk graphene are determined by the low-energy band structure near the K points, we mention them only in passing. A description of their inclusion in the tight-binding model can be found in [13], and the presence of these bands within first-principles calculations are discussed in Section 7.

1.2. *Massless Dirac fermions*

We now describe how the tight-binding model discussed in the previous section yields the famous *massless Dirac fermions* which have made the study of monolayer

graphene so enticing. In this Section, we give a brief overview of the main points: detailed discussion of these results will be given where appropriate in the rest of this review. As noted above, the Fermi energy corresponds to $\mathcal{E}=0$ at the K points. The low-energy properties, corresponding to the electronic states near the Fermi energy, can be described by expanding the energy dispersion around the K points. Writing the graphene wave vector $\vec{q}=\vec{K}+\vec{k}$, such that $|\vec{k}|a \ll 1$, one can write a Taylor expansion of $\mathcal{E}_{\pm}(\vec{q})$ near $\vec{K}$ which yields

$$\mathcal{E}_{\pm}(\vec{k}) = \pm\frac{\sqrt{3}}{2}\gamma_0 ak = \pm v_{\mathrm{F}}\hbar k,$$

where $v_{\mathrm{F}} = \sqrt{3}\gamma_0 a/2\hbar \approx 10^6\,\mathrm{m\,s^{-1}}$ is the Fermi velocity. This velocity is independent of the carrier density, therefore the energy dispersion corresponds to two cones meeting at the K point (see the inset to Figure 2a) with *linear* dependence on the wave vector. The corresponding density of states is

$$\rho(\mathcal{E}) \propto |\mathcal{E}|,$$

i.e. the density of states is linear and vanishes at zero energy. This is a direct consequence of the linear dispersion near K, in marked contrast to conventional two-dimensional electron gas, where the density of states is a constant.

The unique band structure of graphene just described, brings about profound changes in the electronic properties of the system. In the continuum limit and in the effective-mass approximation, the Hamiltonian in the vicinity of the K point is [15]

$$\mathcal{H}_{\mathrm{K}}(\vec{k}) = \hbar v_{\mathrm{F}}\begin{pmatrix} 0 & k_x - \mathrm{i}k_y \\ k_x + \mathrm{i}k_y & 0 \end{pmatrix} = \hbar v_{\mathrm{F}}\vec{\sigma}\cdot\vec{k} = -\mathcal{H}^T_{\mathrm{K}'}(\vec{k}), \tag{2}$$

where the $\vec{\sigma}=(\sigma_x,\sigma_y)$ is a vector of Pauli matrices. The Hamiltonian therefore describes two-dimensional massless neutrinos [15] with a linear energy dispersion, $\mathcal{E}_{\pm}(k)=\pm v_{\mathrm{F}}\hbar k$. The wave functions of these relativistic-like (Dirac) particles have a spinor structure. For the K and K′ points, they are (without normalization)

$$\Psi^{\mathrm{K}}_{s,\vec{k}} = \mathrm{e}^{\mathrm{i}\vec{k}\cdot\vec{r}}\begin{pmatrix} s \\ \mathrm{e}^{\mathrm{i}\theta_{\vec{k}}} \end{pmatrix}; \qquad \Psi^{\mathrm{K}'}_{s,\vec{k}} = \mathrm{e}^{\mathrm{i}\vec{k}\cdot\vec{r}}\begin{pmatrix} \mathrm{e}^{\mathrm{i}\theta_{\vec{k}}} \\ s \end{pmatrix}, \tag{3}$$

where $s=+1$ for the upper band (electrons) and -1 for the lower band (holes), $\tan\theta_{\vec{k}} = k_y/k_x$. The upper and lower terms correspond to the quantum mechanical amplitudes (or *pseudospin*) of finding the particle on one of the two sublattices, A and B. There is a convenient alternative representation of the graphene Hamiltonian which allows the Hamiltonians of the two valleys to be combined into one expression. The basis is written as $\{\phi_A, \phi_B\}$ in the K valley with index $\xi=1$, and $\{\phi_B, \phi_A\}$ in the K′ valley with $\xi=-1$. Then, the Hamiltonian and wave functions for either valley can be written as the 2×2 matrix

$$\mathcal{H}_{\xi}(\vec{k}) = \xi\hbar v_F\begin{pmatrix} 0 & k_x - \mathrm{i}k_y \\ k_x + \mathrm{i}k_y & 0 \end{pmatrix}; \quad \Psi^{\xi}_{s,\vec{k}} = e^{\mathrm{i}\vec{k}\cdot\vec{r}}\begin{pmatrix} \xi s \\ e^{\mathrm{i}\theta_{\vec{k}}} \end{pmatrix}. \tag{4}$$

Interestingly, in graphene, the pseudospin direction is associated with the momentum of the particles. This means that the wave functions in the vicinity of the

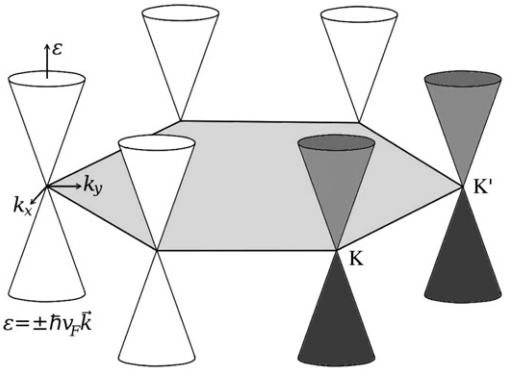

Figure 3. Dirac cones at the Dirac points.

K and K′ points (Dirac points) are *chiral*, or *helical fermions*. One consequence of this is that any backscattering, i.e. scattering of particles from the wave vector $\vec{k}$ to $-\vec{k}$, is suppressed [16]. Particles have opposite chirality in the K or K′ *valleys* or in the electron or hole bands. The energy bands in the vicinity of these Dirac points are two cones meeting at $k = 0$ (Figure 3). The charge carriers in graphene are usually described as *massless Dirac fermions* [17]. Experimental observation of full Dirac cone dispersion has been reported recently [18]. The transformation of electrons in graphene to relativistic-like objects have led to many novel effects: anomalous integer quantum Hall effect, Klein's paradox, novel effects at the edges, etc. They are all subjects of our present review.

1.3. *How it's made*

Monolayer, bilayer and few-layer graphenes[1] are primarily fabricated in one of three ways. Although this review will focus on the theoretical study of graphene, we shall briefly describe these methods here.[2]

The first method is the mechanical exfoliation of single layers from a bulk graphite sample [21,22]. Due to its weakly-bound layered structure, dry cleaving of highly oriented pyrolytic graphite or single graphite crystals has been very successfully utilized by Novoselov *et al.* to synthesize single-, double- and triple-layer flakes up to 10 μm in size. This technique (also called the *Scotch tape* method) involves peeling flakes from bulk graphite using adhesive tape [21], or cleavage by mechanical rubbing [22]. The number of layers in the resulting flakes can be determined by optical spectroscopy and Raman spectroscopy [23] (Section 3.1). The technical details about the preparation and characterization can be found in the excellent review article by the pioneers of this technique [1]. Mechanically exfoliated graphene flakes were important in determining most of the fundamental properties of Dirac fermions that are expected in an isolated graphene plane.

Exfoliated graphene can be processed to create samples of suspended graphene [24–26] where the monolayer flake is not in contact with a substrate. These samples can be created either by placing a metal grid on top of exfoliated graphene [24] or by depositing metallic electrodes [25,26] before etching away the silicon dioxide

substrate from below the graphene. The measured electron mobility is as large as 185,000 $cm^2 V^{-1} s^{-1}$ at 100 K [26] and 230,000 $cm^2 V^{-1} s^{-1}$ at 5 K [25]. This is approximately a factor of 10 higher than the largest reported mobility in exfoliated graphene, and matches predictions based on the measurement of phonon-induced disorder and extrapolation from transport measurements on exfoliated graphene samples [27].

The other main route to fabricate graphene samples has been developed by de Heer *et al*. [28–31]. In this method, hexagonal silicon carbide crystals are heated to approximately 1300°C in ultra-high vacuum which allows the Si atoms to evaporate from the surface leaving behind a purely graphitic film. The properties of the residual film vary depending on which face of the SiC crystal is used in the procedure. If the SiC(0001) (silicon-terminated) face is used, high-quality graphene films are deposited which show Dirac cones in their low-energy band structure, although interaction between the graphene and the substrate induces *n*-type doping which shifts the Fermi energy above the Dirac point. Experimental data suggests that the graphene is covalently bound to the substrate via a buffer layer [32] which does not show graphene-like π bands due to the additional strain caused by a dilated C–C bond length in this layer [33]. In contrast, when the SiC(000$\bar{1}$) (carbon-terminated) face is used, the graphene is not seperated by a buffer layer, but is bound directly to the substrate by weak dispersion forces. Also, multi-layer graphenes grown on this face still exhibit the monolayer-like linear low-energy dispersion because the layers show rotational disorder which minimizes the interactions between them. Magnetospectroscopy of few-layer carbon-face epitaxial graphene [34] also showed the Landau level dispersion characteristic of graphene monolayers. It has been suggested that the interaction between the graphene and the SiC(0001) substrate is not the same for the two sites in the graphene unit cell [35]. This has the effect of opening a band gap at the Dirac points of $\sim$0.26 eV, although this is still controversial as other authors [33,36] claim that many-body effects are the cause of this gap.

Lastly, chemical vapor deposition can be utilized to grow thin graphite films [37,38], and graphene layers [39] which may be patterned and transferred to semiconducting or insulating substrates. In this method [40], hydrocarbon gas is placed near a metal foil surface where the hydrocarbon molecules can be decomposed and carbon atoms are dissolved into the metal. The foil is then allowed to cool (at a predetermined rate) and a carbon film may be formed on the surface. This film can be transferred to a polymer or semiconducting substrate via chemical etching [39]. Graphene monolayers grown in this way can be fully coherent over step edges in the underlying substrate and contain few defects [41,42]. The large size of flakes produced and accompanying high mobility ($\sim$4000 $cm^{-2} V^{-1} s^{-1}$) make chemical vapor deposition a very promising avenue for the future industrial fabrication of graphene devices.

1.4. *Graphene devices*

The relatively short life of experimental research in graphene has limited the number of proposals for devices which might utilize this material. We briefly introduce some device concepts which have been implemented experimentally.

Obviously, the first concept is that of the graphene field effect transistor (FET), but as this is discussed elsewhere in this review, we do not dwell on it now. A comprehensive report on the current state of graphene transitor devices has been written by Lemme [43]. However, two variants do deserve to be mentioned, and they are the high-frequency performance of graphene FETs, and single-electron transistors (SETs). Lin *et al*. [44] demonstrate that a graphene transistor with a gate length of 150 nm may have peak cutoff frequency of 26 GHz, representing a significant step towards utilizing graphene in high-frequency applications, although the authors found the regular $1/f$ behavior of the gain, suggesting that graphene cannot change the operational paradigm of these devices. Other works on high-frequency FETs have been published by Meric *et al*. [45] and Moon *et al*. [46]. Also, Stampfer *et al*. [47] fabricated a fully-tunable single electron transistor from a monolayer graphene nanoribbon and extracted device characteristics from the observed Coulomb diamonds. Additionally, room-temperature spin transport has been measured through graphene transistors [48], with spin polarization to be approximately 10%.

The adsorption of gas molecules on the surface of a graphene flake changes the Hall resistivity, and this effect has been used to develop graphene-based chemical sensors [49]. Micrometer-sized sensors were fabricated which were sensitive to the attaching or detaching of a single gas molecule, producing step-like changes in the resistance. The high sensitivity is a result of the impact of the adsorption on the electronic properties of the graphene flake, which is discussed in detail in Section 8.2.

The mechanical properties of graphene may also be employed in the creation of devices. For example, Bunch *et al*. [50] have created the 'world's thinnest balloon' and claim that it is impermeable to gases. They suggest that this property may be utilized in membrane sensors for pressure changes in small volumes, as selective barriers for filtration of gases, as a platform for imaging of graphene-fluid interfaces and for providing a physical barrier between two phases of matter. Similarly, Stolyarova *et al*. [51] demonstrated that gaseous bubbles can be trapped between a graphene monolayer and the surface of an SiO_2 substrate, and subsequently manipulated by an AFM tip. This has the potential to be applied in 'lab-on-a-chip' devices.

Graphene may also be used as a novel information storage device, as suggested by Standley *et al*. [52]. Retention times of over 24 h, and operation over many thousands of cycles without significant degradation of the device were reported. Finally, the high transparency, large conductivity, high chemical and thermal stability and good flexibility make 'graphene window devices' [53] a natural candidate for solar cells and other next-generation optoelectronic devices. Blake *et al*. [54] argued that graphene, with its low resistivity, high transparency and chemical stability would offer improved durability and simpler technology for future optoelectronic devices.

The properties of graphene are so fascinating that there are reports of attempts to recreate many of those exotic properties in a high-mobility modulated two-dimensional electron gas confined in an AlGaAs/GaAs quantum well [55]. The electronic dispersion in this hexagonal superlattice is expected to be Dirac-like with the pseudospin degree of freedom. Creation of such artificially engineered systems has the obvious advantages over natural graphene because of the possibility to tune the parameters. This would provide unique opportunities to study

Dirac-fermion physics in a conventional two-dimensional electron gas confined in semiconductor systems nanopatterned with honeycomb geometry.

The physics of graphene is a challenging and fascinating subject at the nanoscale. Its impact is already felt both in fundamental scientific research and potential industrial applications. From Dirac electrons in condensed matter to future 'valleytronics' in graphene nanodevices, graphene has unleashed limitless potential to impact our lives as we look through the magical quantum world at the nanoscale, a world that is not much different from an Alice-in-Wonderland world that plays by its own rules.[3] We are yet to completely understand most of those rules, but we hope that this review will help understand some.

2. Graphene in a magnetic field

2.1. *Landau levels in graphene*

Just as for non-relativistic particles, the motion of relativistic charges in graphene in a strong perpendicular magnetic field is quantized, which results in discrete energy levels (Landau levels). In a conventional electron gas (non-relativistic) Landau quantization produces equidistant energy levels, which is due to the parabolic dispersion law of free electrons. In graphene the electrons have relativistic dispersion law, which strongly modifies the Landau quantization of the energy levels and the positions of the levels.

The Landau quantization of the energy levels in graphene in a perpendicular magnetic field has been studied [11] within the tight-binding model [56,57] and within the effective-mass relativistic model [15,58]. The tight-binding approach is the more fundamental one and it is valid for a wider energy range. In many applications of graphene in a magnetic field only the low-energy processes are important, which can be efficiently described within the effective-mass approximation.

The effective-mass Hamiltonian of a single electron in graphene in a uniform perpendicular magnetic field has a form of a 4×4 matrix [15,58]

$$\mathcal{H}_{\mathrm{Dirac}} = v_{\mathrm{F}} \begin{pmatrix} 0 & \pi_x - \mathrm{i}\pi_y & 0 & 0 \\ \pi_x + \mathrm{i}\pi_y & 0 & 0 & 0 \\ 0 & 0 & 0 & \pi_x + \mathrm{i}\pi_y \\ 0 & 0 & \pi_x - \mathrm{i}\pi_y & 0 \end{pmatrix}, \tag{5}$$

where $\vec{\pi} = \vec{p} + e\vec{A}$ is the generalized momentum and $\vec{A}$ is the vector potential. In the above expression we disregard the spin of the electron, taking into account the fact that all energy levels obtained will have additional twofold degeneracy due to spin. For a single electron this degeneracy can be lifted by the Zeeman interaction.

The four-component wave functions corresponding to the Hamiltonian (5) have the form

$$\Psi = \begin{pmatrix} \Psi_{\mathrm{A}}^{\mathrm{K}} \\ \Psi_{\mathrm{B}}^{\mathrm{K}} \\ \Psi_{\mathrm{A}}^{\mathrm{K}'} \\ \Psi_{\mathrm{B}}^{\mathrm{K}'} \end{pmatrix}, \tag{6}$$

where Ψ_A^K and Ψ_B^K are envelope wavefunctions at A and B sites for the valley K, and $\Psi_A^{K'}$ and $\Psi_B^{K'}$ are envelope wavefunctions at A and B sites for the valley K′. For a magnetic field orthogonal to the graphene layer, the vector potential can be chosen in the Landau gauge, $\vec{A} = (0, Bx)$. Then the eigenfunctions of the Hamiltonian (5) are labelled by (j, n, k). Here j=K, K′ is the valley index, which describes the valley pseudospin, $n = 0, \pm1, \pm2, \pm3, \ldots$ is the Landau level index and k is the wave vector along the y axis. If we take into account the electron spin then we need to multiply the wavefunction (6) by the two-component spin function.

The Hamiltonian (5) can be easily diagonalized, which results in the discrete Landau energy level. The energies of the Landau levels depend only on the index n and have the following form:

$$\varepsilon_n = \hbar\omega_B^{\text{Dirac}} \operatorname{sgn}(n)\sqrt{|n|}, \tag{7}$$

where $\omega_B^{\text{Dirac}} = \sqrt{2}v_F/l_B$ and $l_B = \sqrt{\hbar/eB}$ is the magnetic length. The Landau level index, n, can be positive or negative. The positive values correspond to electrons (conduction band), while the negative values correspond to holes (valence band). This expression shows that, in contrast to the case of conventional 2DES, the Landau levels in graphene are not equidistant and the largest energy separation is between the zero and the first Landau level. The typical energy separation between the Landau levels in graphene achieved in experiments is much larger than the corresponding inter-level separation in normal 2D layers. For example, the energy difference between the lowest Landau levels ($n = 0$) and the next Landau levels ($n = \pm1$) is $\Delta E \approx 400\,\text{K}\sqrt{B(\text{Tesla})}$, which for $B = 20$ Tesla is 1800 K. In what follows, we will see that such a large electron energy gap allows one to observe the quantum Hall effect in graphene, even at room temperature.

The wavefunctions corresponding to the Landau levels (7) are given by the following expressions [15,58]:

$$\Psi_{n,k}^K = \frac{C_n}{\sqrt{L}}\exp(-\mathrm{i}ky)\begin{pmatrix} \operatorname{sgn}(n)(-\mathrm{i})\phi_{|n|-1,k} \\ \phi_{|n|,k} \\ 0 \\ 0 \end{pmatrix}, \tag{8}$$

for valley K and

$$\Psi_{n,k}^{K'} = \frac{C_n}{\sqrt{L}}\exp(-\mathrm{i}ky)\begin{pmatrix} 0 \\ 0 \\ \phi_{|n|,k} \\ \operatorname{sgn}(n)(-\mathrm{i})\phi_{|n|-1,k} \end{pmatrix}, \tag{9}$$

for valley K′. Here $C_n = 1$ for $n = 0$, and $C_n = 1/\sqrt{2}$ for $n \neq 0$,

$$\phi_{n,k} = (2^n n!\sqrt{\pi}l_B)^{-\frac{1}{2}}\mathrm{e}^{-z^2/2}H_n[(x - kl_B^2)/l_B] \tag{10}$$

is the standard wavefunction for a non-relativistic electron at the nth Landau level, $H_n(x)$ are the Hermite polynomials, and

$$\mathrm{sgn}(n) = \begin{cases} 0 & (n = 0), \\ n/|n| & (n \neq 0). \end{cases} \tag{11}$$

In terms of the occupation of the sublattices A and B, the wavefunctions (8,9) have an interesting property. Specifically, the wavefunctions at Landau levels $n \neq 0$ always have non-zero amplitudes on both sublattices A and B, while the wavefunctions at the Landau level $n = 0$ have non-zero amplitude only on one sublattice: B sublattice for valley K or A sublattice for valley K′. This property of the wavefunctions of the Landau levels in graphene makes the $n = 0$ Landau level very special for different magnetic applications of graphene.

Taking into account the spin degree of freedom, we can conclude that each Landau level has fourfold degeneracy, which corresponds to twofold degeneracy due to spin and twofold degeneracy due to the valley, i.e. the *flavor* [59], or valley pseudospin [60]. The above description is a single-electron picture of pure graphene. In a many-electron system of real graphene the inter-electron interactions and disorder are important and can introduce splitting of the levels and lift their degeneracy. These topics will be discussed below.

In the presence of an uniform electric field, Lukose *et al.* [61] predicted that the Landau levels are profoundly modified, leading to a collapse of the spectrum when the value of the electric to magnetic field ratio exceeds a certain critical value.

Experimentally, the Landau levels in graphene have been observed by measuring cyclotron resonances of the electrons and holes in infrared spectroscopy experiments [34,62,63], and by measuring tunneling current in scanning tunneling spectroscopy experiments [64–66]. In infrared spectroscopy experiments the Landau level optical transitions were studied. There is a crucial difference between the Landau level optical transitions for non-relativistic electrons in conventional 2DES and relativistic electrons in graphene. For non-relativistic electrons there is the Kohn theorem, which states that the energy of Landau level transitions is equal to the cyclotron energy, regardless of the number of electrons (i.e. the filling factor of the Landau levels), and uninfluenced by the inter-electron interactions. The frequencies of all optical transitions in non-relativistic system are equal to the cyclotron frequency. In the graphene system the Kohn theorem [67] is not applicable. In this case, the frequencies of optical transitions are influenced by the interaction between electrons and the number of electrons, i.e. the filling factor. Since the Landau levels in graphene are not equidistant, all frequencies of optical transitions in graphene are different from each other. The cyclotron optical transitions in a graphene system are of two types: (i) intraband transitions, i.e. transitions between the electron (hole) states; (ii) interband optical transitions, i.e. transitions between the electron and hole states (conduction and valence bands). Since in graphene both conduction and valence bands have the same symmetry, the optical transition selection rule has the same form for both intra- and inter-band transition, and is given by the relation [63]

$$\Delta n = |n_2| - |n_1| = \pm 1. \tag{12}$$

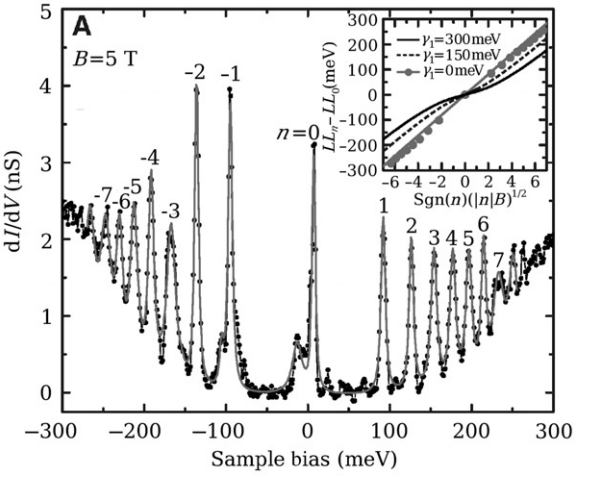

Figure 4. Direct measurement of Landau quantization in epitaxial graphene. Data points show the tunnelling differential conductance spectra versus sample bias of Landau levels in multilayer graphene at $B = 5$ Tesla. Landau level indices are marked. The grey line shows a fit to a series of Voigt line shapes at the Landau level peak positions. Inset: Landau level peak position versus square root of Landau level index and applied field from the peak position in A. Errors in peak positions are smaller than the symbol size (Reprinted figure with permission from D.L. Miller *et al.*, Science, 324, p. 924, 2009 [64]. Copyright © (2009) The American Association for Advancement of Science.).

For example, the allowed optical transitions (absorption) from the Landau level $n = -1$ are $n = -1 \rightarrow n = 0$ (intra-band transition) and $n = -1 \rightarrow n = +2$ (inter-band transition). In usual non-relativistic systems the selection rule for inter-band optical transitions is $n_1 = n_2$.

In scanning tunnelling spectroscopy experiments, the Landau levels are directly observed as the pronounced peaks in the tunnelling spectra [64–66]. From the positions of these peaks the energy of the Landau levels are directly extracted. In Figure 4, typical experimental results of scanning tunneling measurements are shown, where the peaks in the tunneling differential conductance reveal the positions of the Landau levels.

From the experimentally measured cyclotron resonances, the electron Fermi velocity has been obtained [34,62–66]. The electron velocity $v_F \approx 1.1 \times 10^6\,\mathrm{m\,s^{-1}}$ was obtained in [34,62–64], but a smaller value $v_F \approx 0.79 \times 10^6\,\mathrm{m\,s^{-1}}$ was reported in [65]. The reduction of v_F in [65] was attributed to electron–phonon interaction due to strong coupling with the graphite substrate.

The effective-mass approximation of the electron dynamics in graphene in a uniform magnetic field is valid only at low energies, i.e. for low-lying Landau levels. The properties of higher Landau levels can be described within the tight-binding model [56,57]. The Hamiltonian of the tight-binding model has the following form:

$$\mathcal{H}_{\text{tight-binding}} = \sum \varepsilon_i c_i^\dagger c_i + \sum_{<i,j>} t_{ij} c_i^\dagger c_j, \tag{13}$$

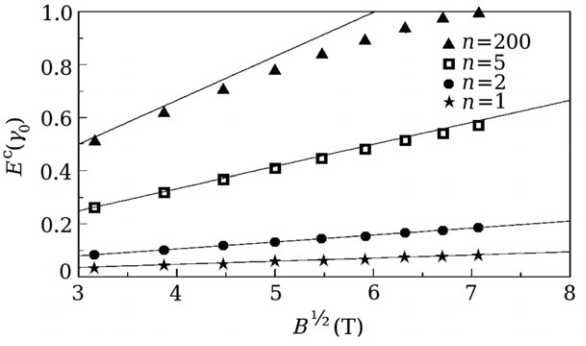

Figure 5. The variation of the low Landau-level energies with square root of magnetic field. The Landau-level energy are obtained within the effective-mass approximation (solid lines) and tight-binding model (symbols). Magnetic field is in Tesla (T) (Reprinted from Physica E, 40, J.H. Ho *et al*., Landau levels in graphene, 1722–1725 [57]. Copyright © (2008), with permission from Elsevier.).

where c_i is the electron annihilation operator. The magnetic field in the tight-binding model is incorporated through the Peierls substitution

$$c_i^\dagger c_j \to c_i^\dagger c_j \exp\left(\int_i^j \vec{A}\mathrm{d}\vec{r}\right). \tag{14}$$

The Landau levels within the tight-binding model have been obtained numerically [56,57]. The results of the calculations show that the effective-mass approximation is valid at low energies, $\varepsilon \lesssim 1\,\mathrm{eV}$, but at higher energies there are deviations from Equation (7). For example, at $B = 30$ Tesla the deviation from Equation (7) occurs at the Landau level $n = 5$ (Figure 5). At high energies the magnetic field also affects the degeneracy of the levels [57]. For example, at energies $\varepsilon \gtrsim 2.5\,\mathrm{eV}$ the valley degeneracy is lifted, resulting in twofold (spin only) degeneracy of the Landau levels.

The non-linear features of the energy dispersion law in graphene have been studied experimentally by magneto-optical transmission spectroscopy [68]. The graphene system has been studied in magnetic fields up to 32 Tesla and within the energy range from the far infrared to the visible. It was found that the low-energy part of the energy spectrum is well described by the linear relativistic equation, while at energies higher than 0.5 eV the deviation from the linear dispersion was observed. For example, at the highest studied energy of 1.25 eV, the deviation from the linear dispersion is around 40 meV.

The parameter which controls the magnetoelectronic properties of graphene within the tight-binding model is the magnetic flux passing through a hexagonal ring of the graphene lattice [69]. As a function of this flux the energy dispersion, the density of states, and magnetoabsorption spectra all have the oscillating behavior [69]. The lattice model of graphene in a magnetic field, introduced beyond the Peierls substitute, was studied in [70,71]. Taking into account the higher order magnetic terms, i.e. the diamagnetic shift and shrinkage of the wave functions, in the lattice Hamiltonian these authors found lifting of two-fold degeneracy of the lowest Landau levels in high magnetic fields.

2.2. *Anomalous quantum Hall effect*

2.2.1. *Experimental observation of the quantum Hall effect in graphene*

Just as for the conventional non-relativistic electron systems [72,73], the Landau quantization of the energy levels in graphene results in the quantization of the Hall conductance, i.e. the quantum Hall effect. In the quantum Hall effect regime, the Hall conductance exhibits a plateau when the Fermi energy, E_F, falls between the Landau levels. Every time the Fermi energy crosses a Landau level, the Hall conductance, σ_{xy}, jumps by an amount of $g_s\, e^2/h$, where g_s is the degeneracy of the Landau level. In graphene, each Landau level has fourfold degeneracy due to valley and spin, i.e. $g_s = 4$. Based on this simple picture of the quantum Hall effect, we expect that the Hall conductance in graphene should show plateaus at $\sigma_{xy} = (4e^2/h)N$, where N is an integer. It so happens that the unique properties of the lowest Landau level ($n = 0$) introduces a shift in quantization of the Hall conductance. This shift is related to the electron–hole symmetry of the graphene layer. The Landau level with $n = 0$ is robust, i.e. it has zero energy regardless of the value of the magnetic field, and it has the properties of both electrons and holes. This quantum anomaly of the $n = 0$ Landau level makes this level effectively twofold degenerate for electrons and twofold degenerate for holes [74]. As a result, the quantization of the Hall conductance occurs at half-integer values

$$\sigma_{xy} = (4e^2/h)\left(N + \frac{1}{2}\right). \tag{15}$$

The half-integer (or anomalous) quantum Hall effect corresponds to the filling factors $\nu = 4(N + \frac{1}{2}) = \pm 2, \pm 6, \pm 10, \ldots$. This sequence of filling factors is different from that of the conventional semiconductor quantum Hall effect (where the plateaus are at $\nu = \pm 4, \pm 8, \pm 12, \ldots$) and this anomalous behavior gives the phenomenon its name (see, e.g. [75]). This quantization rule can be derived from the Kubo formalism [76–79] applied to relativistic electrons in graphene [74,80–82]. The half-integer quantum Hall effect has been observed experimentally [17,83–85]. The typical experimental results for the magnetoresistance and Hall resistance are shown in Figure 6. The Hall resistance shows plateaus at filling factors $\nu = 4(N + \frac{1}{2})$, while the magnetoresistance vanishes. A good quality sample studied in [85] (mobility of electrons was higher than $10^4\,\mathrm{cm^2\,V^{-1}\,s^{-1}}$) allows one to observe plateaus at large filling factors. The quantum Hall effect is clearly seen at filling factors $\nu = \pm 2$ and $\nu = \pm 6$. A developing plateau at $\nu = 10$ is also visible.

An important breakthrough has occured recently. The quantum Hall effect has been observed in epitaxial graphene layers grown on silicon carbide [86,87], thus illustrating the similarity of fundamental electronic properties of epitaxial and exfoliated graphene films. The growth conditions and electrical characteristics of epitaxial graphene films strongly depend on the type of the face of SiC. The growth of graphene on the C-face is rapid and results in graphene films with high mobility around $20{,}000\,\mathrm{cm^2\,V^{-1}s^{-1}}$ [86]. The formation of graphene films on the Si-face is slower and can be easily controlled, but the mobility of the carrier is much smaller with the typical value around $1500\,\mathrm{cm^2\,V^{-1}\,s^{-1}}$. For the high-mobility epitaxial graphene on the C-face, the quantum Hall plateaus corresponding to filling factors $\nu = 2, 6, 10$, and 14 have been observed [86]. For low-mobility epitaxial graphene

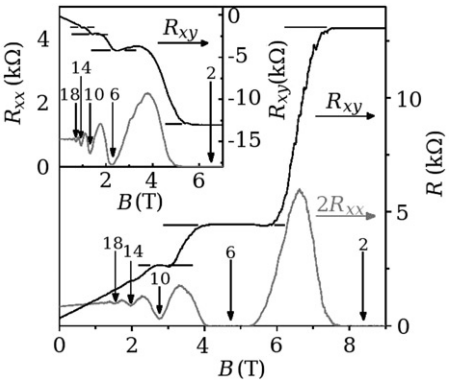

Figure 6. Hall resistance (R_{xy}) and magnetoresistance (R_{xx}) versus the magnetic field at $T = 30$ mK. The vertical arrows and the numbers on them indicate the values of the corresponding filling factor, ν, of the quantum Hall state. The horizontal lines correspond to $h/e^2\nu$ values. The inset shows the quantum Hall effect for a hole gas, measured at 1.6 K (Reprinted with permission from Y. Zhang *et al.*, Nature, 438, p. 201, 2005 [85]. Copyright © (2005) Nature Publishing Group.).

grown on the Si-face, only the lowest quantum Hall effect with filling factors $\nu = 2$, 6, and 10 have been reported [87]. These results bring epitaxial graphene a step closer to becoming a scalable platform for graphene-based electronics.

One important difference between the quantum Hall effect in graphene and that in usual non-relativistic systems is that the quantum Hall effect in graphene survives even at room temperature [83,84,88]. The reason for such robust behavior of the quantum Hall states is the large activation energy, i.e. the cyclotron energy. For example, at $B = 45$ Tesla the energy gap is 2800 K, which exceeds the thermal energy at room temperature by a factor of 10. The quantum Hall effect has been observed at room temperatures even in a sample with low mobility, $\mu = 4000\,\mathrm{cm^2\,V^{-1}\,s^{-1}}$ [83]. These properties of the quantum Hall effect in graphene are in stark contrast to what we have seen in non-relativistic systems, where the quantum Hall effect can be realized only at low temperatures and in samples with high electron mobility.

In [89,90] the activation energies of the quantum Hall states have been extracted from the Arrhenius plots (temperature dependence). The excitation gaps for $\nu = \pm 2$ and $\nu = 6$ quantum Hall states have been analyzed. The excitation gaps are affected by the Landau level broadening, which depends on the magnetic field and the strength of the disorder. Without any Landau level broadening the excitation gaps are equal to the energy gaps between the nearest sharp Landau levels. The broadening of the Landau levels introduces a constant offset of the excitation gaps from the theoretical value for the sharp Landau levels (Figure 7). For the quantum Hall state at $\nu = 6$, the experimental results are consistent with the picture of broad Landau levels with the broadening around 400 K. The $\nu = \pm 2$ gap, however, behaves totally differently. For example, at a high magnetic field the $\nu = \pm 2$ gap, approaches the bare Landau-level separation. This behavior can only be explained by the unique nature of the $n = 0$ Landau level: with increasing magnetic field the $n = 0$ Landau level becomes very sharp. The density of states, which illustrates the sharp nature of the $n = 0$ Landau level, is shown schematically in Figure 7.

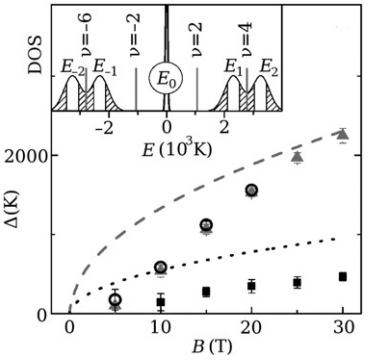

Figure 7. Energy gap between two Landau levels as a function of magnetic field for $\nu = 2$ (full triangles), $\nu = -2$ (open circles), and $\nu = 6$ (full squares) as deduced from the Arrhenius plots. The dashed and dotted lines are the expected (theoretically) energy gaps for sharp Landau levels. The inset shows schematically the density of states for a sharp $n = 0$ Landau level and broadened higher Landau levels for electrons and holes at 30 Tesla. The form and width of the higher Landau levels were extracted from the experimental data. Extended states are represented by the white areas, localized states by the dashed areas (Reprinted figure with permission from A.J.M. Giesben *et al.*, Physical Review Letters, 99, 206803, 2007 [89]. Copyright © (2007) by the American Physical Society.).

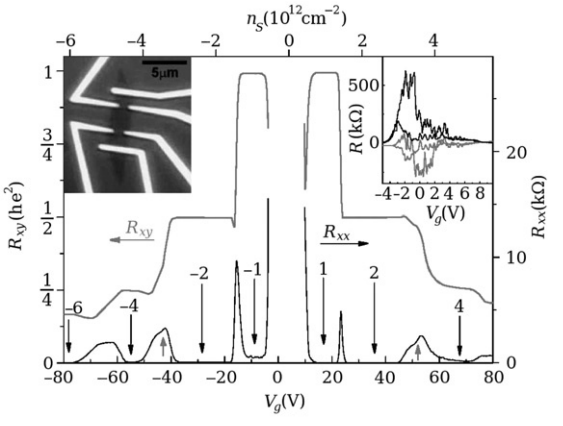

Figure 8. R_{xx} and R_{xy} measured in the device shown in the left inset, as a function of gate voltage, V_g, at $B = 45$ T and $T = 1.4$ K. $-R_{xy}$ is plotted for $V_g > 0$. The numbers with the vertical arrows indicate the corresponding filling factor, ν. Gray arrows indicate developing quantum Hall states at $\nu = \pm 3$. n_s is the sheet carrier density derived from the geometric consideration. Right inset: R_{xx} and R_{xy} or another device measured at $B = 30$ T and $T = 1.4$ K in the region close to the Dirac point. Left inset: an optical microscope image of a graphene device used in this experiment (Reprinted figure with permission from Y. Zhang *et al.*, Physical Review Letters, 96, 136806, 2006 [92]. Copyright © (2006) by the American Physical Society.).

At large magnetic fields, $B > 20$ Tesla, and in high-mobility samples (mobility as high as 5×10^4 cm^2 V^{-1}s^{-1}), new quantum Hall plateaus at filling factors $\nu = 0, \pm 1, \pm 4$ have been reported in the literature [86,91,92]. The new quantum Hall plateaus are shown in Figure 8 with clear quantization of the Hall resistance and vanishing

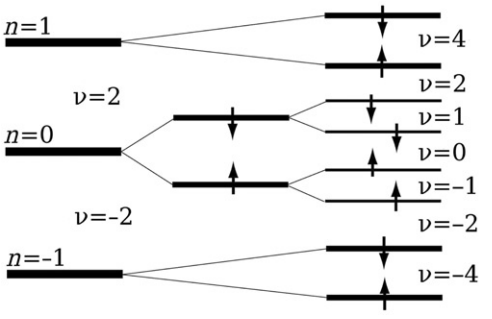

Figure 9. Schematic illustration of the hierarchy of the lifting the degeneracy of the Landau levels in strong magnetic fields. Here n is the Landau level index and ν describes the corresponding quantum Hall effect. The arrows next to the lines illustrate the direction of the spin at the corresponding energy levels. The fourfold degeneracy of the Landau level $n=0$ is completely lifted. For the $n=\pm1$ Landau levels only the twofold spin degeneracy is lifted and each level remains twofold valley degenerate.

magnetoresistance. Such plateaus originate from lifting of the fourfold degeneracy of the Landau levels. The quantum Hall effect at $\nu=0, \pm1$ indicates that the fourfold degeneracy of the Landau level $n=0$ is completely lifted [86,91,92], so that the Hall conductance, σ_{xy}, increases in steps of e^2/h as the Fermi level passes through the Landau levels. The fact that only $\nu=\pm4$ quantum Hall plateaus are observed means that the fourfold degeneracy of the Landau levels $n=\pm1$ is only partially resolved. The experiments in a tilted magnetic field [86,92] show that for the Landau level $n=1$ the twofold spin degeneracy is lifted, leaving the twofold valley degeneracy unbroken.

To distinguish the origin of the broken symmetry (either spin or valley), experiments in a tilted magnetic field have been performed [91]. The spin splitting, which is related to the Zeeman energy, depends on the total magnetic field, while the valley (sublattice) splitting depends only on the perpendicular component of the magnetic field. This is because the valley splitting is caused by the electron–electron interaction and the corresponding ground state is the valley ferromagnet (see the next section). The results of magnetotransport measurements show that the minimum magnetoresistance, which is determined by the inter-level splitting, depends on the total magnetic field for $\nu=\pm4$, and depends on the perpendicular component of the magnetic field for $\nu=\pm1$ [91]. These results show that the states $\nu=0$ and $\nu=\pm1$ arise from the lifting of the spin and valley degeneracy of the Landau level $n=0$, respectively [91]. The order of the lifting of the degeneracy of the Landau levels $n=0$ and $n=\pm1$ in graphene is illustrated in Figure 9.

Although the behavior of the Hall conductance, σ_{xy}, is consistent with the lifting of the degeneracy of the Landau level $n=0$, the properties of the magnetoresistance, R_{xx}, are unexpected. For the usual quantum Hall effect in non-relativistic systems the magnetoresistance, R_{xx}, shows a minimum at the quantum Hall plateaus and activated behavior as a function of temperature. Such a behavior is observed in graphene for $\nu=\pm1$ Hall states, but the $\nu=0$ Hall state does not show the minimum resistance [91]. There is also no activated behavior at $\nu=0$. In Figure 10 the magnetoresistance of a graphene sample is shown for three values of magnetic field.

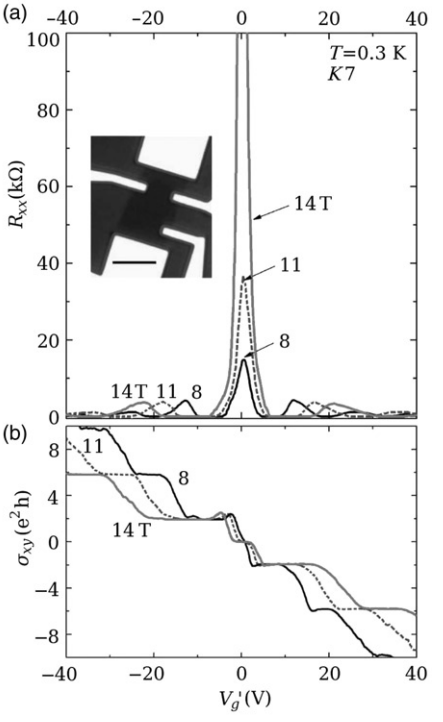

Figure 10. The magnetoresistance R_{xx} (a) and Hall conductivity σ_{xy} (b) versus gate voltage, V_g', at 0.3 K with the magnetic field fixed at 8, 11, and 14 T. Peaks of R_{xx} at finite gate voltage correspond to the filling of the $n=1$ and $n=2$ Landau levels. At zero bias voltage the peak in R_{xx} grows to $190\,k\Omega$ at 14 Tesla. The inset shows the sample with Au leads deposited. The bar indicate 5 μm. Panel (b) shows the quantization of Hall conductance at the values $(4e^2/h)(n+\frac{1}{2})$. At 0.3 K, $\sigma_{xy}=0$ in a 2-V interval around $V_g'=0$ (Reprinted figure with permission from J.G. Checkelsky *et al.*, Physical Review Letters, 100, 206801, 2008 [93]. Copyright © (2008) by the American Physical Society.).

The magnetoresistance maximum (not minimum) is clearly seen at zero filling factor (zero bias).

The $\nu=\pm1$ are the usual quantum Hall states with a minimum resistance and activation behavior. The activation energy at $\nu=\pm1$ has a non-linear magnetic field dependence, which was attributed to the many-body effects indicating a many-body origin of the $\nu=\pm1$ states [91].

A detailed analysis of the $\nu=0$ quantum Hall state has shown that this state can be in two phases: metallic or insulating, which are characterized by finite and infinitely large values of the magnetoresistance, R_{xx} [93,94], respectively. The transition from the metallic to the insulating phase occurs with increasing magnetic field at some critical value B_c. In all samples studied in [94] the critical magnetic field is around $B_c \approx 30$ Tesla. The actual value of the critical magnetic field depends on the disorder strength in a non-trivial way, namely, with increasing disorder the critical magnetic field increases [94]. The phase transition of the $\nu=0$ quantum Hall state was identified as the Berezinskii–Kosterlitz–Thouless phase transition, for which the magnetic field plays the role of the effective temperature. In two-dimensional systems

such a transition is described by the XY model. Within this model the ordered phase is destroyed at the transition point by unbinding of pairs of topological excitations, the corresponding separation (correlation length), ξ, depends on the deviation of the magnetic field (effective temperature) from the critical value in the following form:

$$\xi = a \exp[b/\sqrt{1 - B/B_c}], \tag{16}$$

where a is the lattice constant and b is a number of the order 1. The expression (16) fits the experimental data [94], which indicates that at $\nu = 0$ the system shows the Berezinskii–Kosterlitz–Thouless phase transition to a high-field insulating ordered state.

Recent experiments performed in ultraclean suspended graphene samples [95,96] illustrate an insulating nature of the $\nu = 0$ quantum Hall state. The device is fully insulating at high magnetic fields ($B > 5$ Tesla) and at low temperature ($T < 10$ K), while at higher temperature the system shows an activated behavior with an energy of 60 K [96]. The distinctive features of the suspended graphene compared to the graphene on substrate are very high quality of graphene samples and enhanced inter-electron interaction strength. The enhancement of the electron–electron interactions is due to the small value of dielectric constant ($\epsilon = 1$) of suspended graphene.

A strong increase in low-temperature resistivity, ρ_{xx}, in graphene samples with a relatively large amount of disorder have been observed in [97]. In terms of the conductivity, the graphene system at the charge neutrality point has shown a zero-value plateau in the Hall conductivity, σ_{xy}, and a minimum in the longitudinal conductivity, σ_{xx}. Such a behavior was explained in [97] as due to opening of a gap, e.g. due to the Zeeman splitting, in the density of states at the $n = 0$ Landau level. Due to the presence of large disorder, the opening of the gap was observed only for the $n = 0$ Landau level, for which the width of the Landau level is much smaller compared to that in higher Landau levels.

2.2.2. *Symmetry breaking: theoretical models*

Experimental observation of the $\nu = 0, \pm 1, \pm 4$ quantum Hall effect opens the question of a mechanism of a symmetry breaking in graphene, which results in lifting of the degeneracy of the Landau levels and the additional quantum Hall plateau. The problem of symmetry breaking in graphene systems in a magnetic field has been studied theoretically in detail [59,75,98–111]. A review of the different aspects of spontaneous symmetry breaking in graphene is available in [107]. Here we discuss only the main mechanisms of symmetry breaking and lifting of the Landau level degeneracy in graphene. In general, the following mechanisms can break the symmetry in graphene quantum Hall systems: (i) disorder can lift the twofold valley degeneracy. (ii) Electron–electron interactions can lift both valley and spin degeneracies. For example, the exchange part of the electron–electron interaction favors the quantum Hall ferromagnetic state. (iii) Zeeman interaction, which is an explicit symmetry breaking term in the Hamiltonian. The Zeeman interaction can lift only the spin degeneracy. (iv) Explicit terms in the Hamiltonian, which can lift the valley symmetry. These terms originate from the graphene lattice structure.

2.2.3. *Symmetry breaking: disorder effects*

Within the noninteracting electron system the main mechanism of symmetry breaking is the interaction with the disorder potential, which introduces the intervalley coupling and splits the valley subbands. Such a potential should be short-ranged with the length scale of the order of the lattice constant [75,105]. An example of a short-range potential is a scatterer localized at a particular A or B site with a random amplitude. Such a potential introduces the following term into the relativistic Hamiltonian (5)

$$U(r) = \begin{pmatrix} 1 & 0 & z_{\mathrm{A}}^{*} z'_{\mathrm{A}} & 0 \\ 0 & 0 & 0 & 0 \\ z'^{*}_{\mathrm{A}} z_{\mathrm{A}} & 0 & 1 & 0 \\ 0 & 0 & 0 & 0 \end{pmatrix} u_s \delta\left(\vec{r} - \vec{R}_{\mathrm{A}}\right) + \begin{pmatrix} 0 & 0 & 0 & 0 \\ 0 & 1 & 0 & z_{\mathrm{B}}^{*} z'_{\mathrm{B}} \\ 0 & 0 & 0 & 0 \\ 0 & z'^{*}_{\mathrm{B}} z_{\mathrm{B}} & 0 & 1 \end{pmatrix} u_s \delta\left(\vec{r} - \vec{R}_{\mathrm{B}}\right), \tag{17}$$

where $z_X = \mathrm{e}^{\mathrm{i}\vec{K}\vec{R}_X}$, $z'_X = \mathrm{e}^{\mathrm{i}\vec{K}'\vec{R}_X}$, $X = \mathrm{A}$, B and $u_s = (\sqrt{3}a^2/2)U_s$, U_s is the random amplitude of the on-site potential. The first and second terms in Equation (17) correspond to the scatterer on sites A and B, respectively (Figure 11).

It is easy to see that the short-range potential (17) has very different effects on the lowest Landau level, $n = 0$, and on higher Landau levels, $|n| > 0$. Indeed, the amplitudes of the wavefunctions in the $n = 0$ Landau level is non-zero only on one

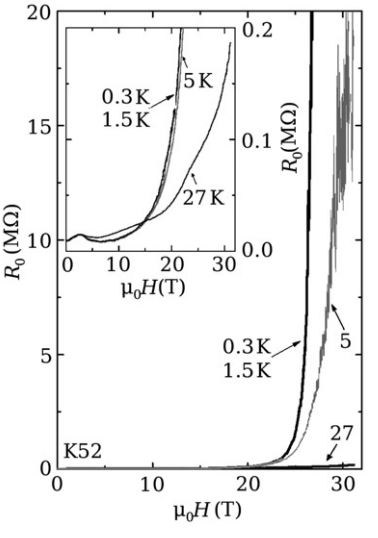

Figure 11. Main panel: divergence of the maximum magnetoresistance, R_0, at the Dirac point with B at $T = 0.3$, 1.5, 5, and 27 K. At 27 K, the increase in R_0 is quite moderate (to 190 $k\Omega$ at $H = 31$ Tesla). At $T = 0.3$ K, however, R_0 exceeds 20 $M\Omega$ above 27 T. The curves at 0.3 and 1.5 K undergo a 1000-fold increase (40 $k\Omega$ to 40 $M\Omega$) in the narrow field interval $17 - 27$ T. In high B, the 5 K curve deviates significantly from them. The inset shows the behavior of R_0 versus B in greatly expanded scale ($\times 100$) (Reprinted figure with permission from J.G. Checkelsky *et al.*, Physical Review B, 79, 115434, 2009 [94]. Copyright © (2009) by the American Physical Society.).

of the sublattices, either A or B. As a result the intervalley matrix element of the potential (17) is zero for the states of the lowest Landau level, $n=0$. Therefore, if the Landau level mixing is disregarded then the random on-site (short-range) potential does not lift the valley degeneracy for the $n=0$ Landau level [105]. For higher Landau levels even the on-site potential introduces intervalley coupling, which results in lifting of the valley degeneracy. If the Landau level mixing is taken into account then even at the lowest Landau level, the short-range potential introduces the intervalley coupling [75].

Disorder-induced intervalley coupling and mixture in the lowest Landau level results also in anomalous electron localization properties [110]: increasing the strength of the on-site random potential introduces *delocalization*, instead of localization in the lowest Landau level. This anomalous behavior is closely related to the Landau level mixing and it is correlated with the disorder-induced valley depolarization of the Landau level states [110] due to mixing of the valleys.

In the lowest Landau level, the intervalley coupling can be introduced even without the Landau level mixing through the randomness in the hopping intergral between two neighboring sites [104,105,112]. Such randomness can be realized through the local lattice distortion or due to scatterers localized between the neighboring sites. The shift from t to $t+\delta t$ in the hopping integral between the neighboring atoms at sites A and B results in the following potential term in the relativistic Hamiltonian [105]

$$U(r)=\begin{pmatrix} 0 & z_{\mathrm{A}}^{*}z_{\mathrm{B}} & 0 & z_{\mathrm{A}}^{*}z_{\mathrm{B}}' \\ z_{\mathrm{B}}^{*}z_{\mathrm{A}} & 0 & z_{\mathrm{A}}^{*}z_{\mathrm{A}}' & 0 \\ 0 & z_{\mathrm{A}}'^{*}z_{\mathrm{B}} & 0 & z_{\mathrm{A}}'^{*}z_{\mathrm{B}}' \\ z_{\mathrm{B}}'^{*}z_{\mathrm{A}} & 0 & z_{\mathrm{B}}'^{*}z_{\mathrm{A}}' & 0 \end{pmatrix} u_h \delta\left(\vec{r}-\vec{r}_i\right), \tag{18}$$

where $u_h=(\sqrt{3}a^2/2)\delta t$. It is easy to see that even in the lowest Landau level the intervalley matrix elements are non-zero.

The randomness in intervalley hopping integrals can be reformulated in terms of an effective random magnetic field [104]. If the variations of the hopping integrals between the site j and the nearest neighbor sites (there are three such sites) are δt_i, $i=1,2,3$, then a vector potential for valleys K and K′ at point j is [104]

$$a_X=\frac{c}{e}\sum_{i=1,2,3}\delta t_i \mathrm{e}^{\mathrm{i}X\vec{e}_i}, \tag{19}$$

where $X=\mathrm{K}$ or K′. Such a vector potential introduces a random magnetic field, δh, pointing in the z direction (orthogonal to the graphene layer), which results in a Zeeman-like interaction for the pseudospin order parameter. The typical fluctuation of the random magnetic field is around 0.1–1 Tesla [104]. Although the weak random magnetic field, δh, is orthogonal to the graphene plane, it produces an easy-plane anisotropy which favors the XY valley ferromagnetic state [104]. The XY ferromagnetic system shows the Berezinskii–Kosterlitz–Thouless transition to the ordered state. Due to the valley anisotropy-induced random magnetic field, the twofold valley degeneracy of the Landau level is lifted. The Zeeman energy lifts the twofold spin degeneracy. Taking into account both the effective random

magnetic field and the Zeeman interaction, we obtain a complete lifting of the fourfold degeneracy of the Landau level. In the lowest Landau level the valley anisotropy induced by the random magnetic field is around few degrees of Kelvin at an uniform magnetic field of 30 Tesla, while the Zeeman splitting at $B = 30$ Tesla is around 50 K. This energy scale is consistent with the hierarchy of lifting the degeneracy of the $n = 0$ Landau level, as shown in Figure 9. Therefore the $\nu = 1$ quantum Hall state is valley and spin polarized while the $\nu = 0$ state is spin-polarized and valley-unpolarized.

The disorder in graphene not only results in valley symmetry breaking but also destroys the quantum Hall effect as in non-relativistic systems. The effect of disorder on the existence of the quantum Hall states and electron localization in a strong magnetic field has been studied numerically within the tight-binding model with random on-site potential [99,106,110]. The corresponding Hamiltonian has the following form:

$$\mathcal{H}_{\text{tight-binding}} = \sum \varepsilon_i c_i^\dagger c_i + t \sum_{<i,j>} c_i^\dagger c_j, \tag{20}$$

where the hopping integral t is assumed to be constant and the disorder is introduced through the randomness in the values of the on-site energies, ε_i. In this approach, the mixing between the Landau levels is taken into account automatically and the intervalley coupling is introduced for all Landau levels. It was found that the most robust quantum Hall state against the disorder strength is the $\nu = \pm 2$ state [99] for a system without symmetry breaking and the $\nu = \pm 1$ state [106] for a system with lifted degeneracy of the Landau levels.

2.2.4. *Symmetry breaking: the effect of electron–electron interaction*

The disorder potential does not affect the twofold spin degeneracy. The simplest mechanism of breaking the spin symmetry is the Zeeman interaction, $g\mu_B B$, which splits the single particle spin levels. The g-factor of electrons in graphene is close to 2, resulting in the Zeeman energy $g\mu_B B \approx 1.5B$[Tesla] K. Another mechanism of breaking the spin symmetry is related to the long-range Coulomb interaction through the formation of the ferromagnetic state [59,98,101,103,106]. The quantum ferromagnetic state is stabilized by the exchange part of the Coulomb interaction. This symmetry breaking mechanism works well for both spin and valley symmetries.

In the case of the valley symmetry the Coulomb interaction Hamiltonian has also explicit lattice symmetry-breaking terms [59,101,103]. These terms can be obtained from the exact expression for the Coulomb repulsion Hamiltonian within the lattice model

$$\mathcal{H}_S = \frac{1}{2} \sum_{\vec{x}, \vec{x}'} V(\vec{x} - \vec{x}') n_x n_{x'}, \tag{21}$$

where $V(r)$ is the Coulomb interaction potential and n_x is the total electron number operator. Rewriting the above expression in the continuum approximation, one can

obtain the following terms in the interaction Hamiltonian in a continuum theory [59,103]:

(i) SU(4) spin and valley symmetric Hamiltonian, $\mathcal{H}_S$.

$$\mathcal{H}_S = \frac{1}{2}\int d^2\vec{x}d^2\vec{x}'\rho_{\text{total}}(\vec{x})V(\vec{x}-\vec{x}')\rho_{\text{total}}(\vec{x}'), \tag{22}$$

where ρ_{total} is the total electron density operator.

(ii) Valley symmetry breaking term, $\mathcal{H}_{BS,1}$, is due to backscattering processes and has the following form [59,103]:

$$\mathcal{H}_{BS,1} = -u_2\Big[J_+^\dagger J_+ + J_-^\dagger J_-\Big], \tag{23}$$

where $u_2 \approx (4/3)a^2(e^2/4\pi\epsilon a_0)$, $J_+ = \psi^\dagger_{\text{K,A}}\psi_{\text{K}',B}$ and $J_- = \psi^\dagger_{\text{K,B}}\psi_{\text{K}',\text{A}}$. Here $\psi_{X,A}$ and $\psi_{X,B}$ are annihilation operators for valley $X = \text{K}, \text{K}'$ corresponding to sublattices A and B, respectively.

(iii) Valley symmetry breaking term, $\mathcal{H}_{BS,2}$, reflects the lattice-scale physics [59,103]. These terms originate from the fact that the two sublattices are shifted with respect to each other. As a result, two electrons at the same continuous point interact stronger if they belong to the same sublattice than if they belong to different sublattices. This symmetry breaking term has the following form:

$$\mathcal{H}_{BS,2} = -\int d^2\vec{x}\sum_{\vec{r}} v_1(\vec{r})\rho_{\text{stag}}(\vec{x}+\vec{r})\rho_{\text{stag}}(\vec{x}). \tag{24}$$

Here $\vec{r}$ corresponds to the positions of sites of one of the sublattice, ρ_{stag} is the staggered electron density between sublattices A and B [59,103] and

$$v_1(\vec{r}) = \frac{\sqrt{3}a^2}{8}\Big[V(\vec{r}+1/\sqrt{3}\hat{y}) - V(r)\Big], \tag{25}$$

for $r \neq 0$. This symmetry breaking term is algebraically small and is of the order of (a/l_B) compared to the Coulomb energy, $(e^2/\epsilon l_B)$ [59,101,103], where a is the lattice constant in graphene. This lattice symmetry breaking term can also be understood in terms of the analogy of the two valley system and the usual bilayer non-relativistic electron system. Here each layer corresponds to a single valley, and the distance between the layers is of the order of the lattice constant, a. Therefore, the asymmetry is controlled by the small parameter $a/l_B \sim 0.03$ at $B \approx 30$ Tesla. The interaction described by the Hamiltonian $\mathcal{H}_{BS,2}$ is short-ranged, but one should be careful when dealing with the lowest Landau level, $n = 0$. As we discussed in the previous section, at the lowest Landau level the short-range interaction does not introduce the intervalley coupling, i.e. the intervalley matrix element is zero. Therefore, when considering the lowest Landau level the finite range of the interaction potential v_1 should be taken into account. As a result, the valley symmetry breaking term becomes additionally suppressed by a factor of a/l_B in the lowest Landau level [59,103]. There are also interaction-induced umklapp scattering processes, which also introduce the valley symmetry breaking terms. These processes are exponentially small in a/l_B and are considered in [101].

The SU(4) symmetric interaction Hamiltonian (22) results in spin and valley ferromagnetic ordering, i.e. spontaneous symmetry breaking at corresponding Landau filling factors [98,106]. The direction of spin or pseudospin ordering in the quantum ferromagnetic state is determined by small explicit symmetry breaking terms in the Hamiltonian. Such symmetry breaking terms can result in easy axis or easy plane ferromagnetic states with ferromagnetic order perpendicular or parallel to the graphene layer, respectively [59,103]. In the case of spin, the explicit symmetry breaking term is the Zeeman Hamiltonian, which results in easy axis ferromagnetic ordering.

For valley pseudospin we need to consider the lattice-related symmetry breaking Hamiltonians (23), (24). It was shown that at odd filling factors the symmetry breaking Hamiltonian (24) provides the leading symmetry breaking interaction. This type of Hamiltonian results in easy axis valley ferromagnetic state at the lowest Landau level ($\nu = \pm 1$ quantum Hall states) and easy plane ferromagnetic state at the Landau level $n = \pm 1$ ($\nu = 3$ and 5 quantum Hall states) [59,103]. The explicit numerical analysis of a finite electron system within the tight-binding model with Coulomb interaction supports this conclusion [106].

The easy axis valley ferromagnetic state at $n = 0$ Landau level ($\nu = \pm 1$) means that all electrons at filling factor $\nu = 1$ occupy one valley only:

$$|\nu = -1\rangle = \prod_m c^{\dagger}_{\uparrow \mathrm{K},m} |\mathrm{vac}\rangle. \tag{26}$$

Since the wavefunctions of a single valley at $n = 0$ Landau level occupy only one sublattice, the easy axis valley ferromagnetic ordering means that the electrons reside on one sublattice producing a charge density wave. For the easy plane ferromagnetic state realized at $\nu = 3$ and $\nu = 5$ the Berezinskii–Kosterlitz–Thouless transition is expected [59,103]. The effect of the symmetry breaking Hamiltonian (23) has been studied in [101]. It was shown that this type of valley symmetry breaking term results in easy-plane valley ferromagnetic ordering.

Disorder suppresses the exchange ferromagnetic ordering and there is a critical disorder strength above which the corresponding quantum Hall effect is destroyed. A numerical analysis of the tight-binding model of graphene in a strong magnetic field shows that the critical disorder strength for the $\nu = 3$ ferromagnetic state ($n = 1$ Landau level) is much smaller than the critical disorder strength for the $\nu = 1$ state ($n = 0$ Landau level). A similar conclusion was reached in [98] using the Stoner criterion for the formation of quantum Hall ferromagnetism. In [98] the inter-electron interaction was treated within the Hartree–Fock approximation and the disorder was introduced within the self-consistent Born approximation. Within this approach the phase diagram (Figure 12), illustrating the sensitivity of quantum Hall states to the strength of the disorder, was obtained [98].

The stability of exchange-induced ferromagnetic ordering is determined by the strength of inter-electron interactions. Without the disorder the inter-electron interactions completely characterize the energy. Formation of the ferromagnetic ordering within the finite-size system has been studied numerically in [113], where only the spin degree of freedom was taken into account. For the Landau levels $n = 0$, 1, 2, and 3 the formation of spin-ordered states, i.e. ferromagnetic states, for a partially occupied Landau level, the corresponding filling factor $\frac{1}{2}$ has been obtained.

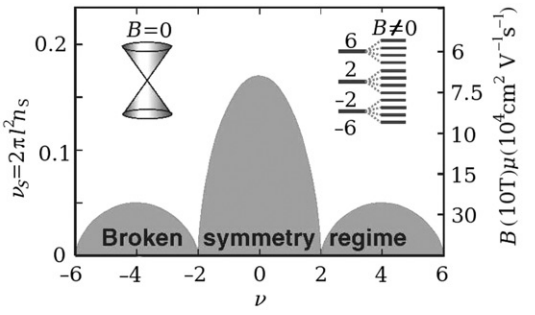

Figure 12. Phase diagram for SU(4) quantum Hall ferromagnetism in the $n=0$ and $n=1$ Landau levels of graphene. The ordered region is bounded by a maximum value of ν_s, the ratio of the density of Coulomb scatterers to the density of a full Landau level. ν_s is inversely proportional to the product of the sample mobility and the external field strength and order near integer filling factors requires the minimum values for this product indicated on the right-hand vertical axis (Reprinted figure with permission from K. Nomura and A.H. MacDonald, Physical Review Letters, 96, 256602, 2006 [98]. Copyright © (2006) by the American Physical Society.).

For each quantum Hall state, both the ground state Coulomb energy and the activation gaps have been found. The activation gap is one of the important parameters, which characterizes the stability of the corresponding quantum Hall state with respect to disorder and temperature. Due to the unique structure of the Landau wavefunctions in graphene, the interaction-induced activation energy of the spin-ordered states is largest for the $n=1$ Landau level. These results illustrate that the electron correlations are dominant for the $n=1$ Landau level and the ferromagnetic ordered quantum Hall state should be the most stable. This behavior is different from the non-relativistic system, where the largest excitation gap is expected in the lowest Landau level.

The charged excitations of the quantum ferromagnetic states are skyrmions, which are similar in structure to the skyrmionic states in usual multi-component non-relativistic systems. The properties of skyrmions at the nth Landau level are determined by the relative strength of the Coulomb interaction within the nth Landau level and a symmetry breaking term, e.g. the Zeeman coupling. The interaction within that Landau level is obtained from the expression (22) by taking the projection of the Hamiltonian $\mathcal{H}_S$ onto the nth Landau level. Due to the special structure of the wavefunctions belonging to different Landau levels (Equations (8) and (9)), the projection of the Coulomb interaction Hamiltonian onto the nth Landau level takes the following form [98,101]:

$$\mathcal{H}_{S,n} = \frac{1}{2}\sum_{\sigma,\sigma'}\sum_{q}\frac{2\pi e^2}{\epsilon q}[F_n(ql_B)]^2\rho_{n,\sigma}(-\vec{q})\rho_{\sigma^n\sigma^{n\prime}}(\vec{q}), \tag{27}$$

where the form factor is given by the following expression:

$$F_0(x) = L_0(x^2/2) \tag{28}$$

$$F_n(x) = \frac{1}{2}\left[L_n\left(x^2/2\right) + L_{n-1}\left(x^2/2\right)\right], \tag{29}$$

where $x = ql_B$, and $L_m(x)$ are the Laguerre polynomials. In the above expressions (27)–(29), a magnetic field specific Gaussian factor, $\exp[-(ql_B)^2/4]$, is absorbed in the definition of the electron density. Therefore the form factors have a polynomial form [101]. The Gaussian factor can also be introduced not only in the electron density but also in the form factors themselves [98].

In the usual two-component non-relativistic systems the skyrmionic excitations exist only in the lowest Landau level (filling factor $\nu = 1$). In graphene the Coulomb interaction is several times stronger than in non-relativistic systems, e.g. GaAs. As a result, the skyrmion excitations survive even in higher Landau levels, $|n| \leq 3$ [59,102]. The charge of such excitations is ± 1 for any integer filling [102].

Another interaction-induced mechanism for spontaneous symmetry breaking was introduced in a series of publications [100,108,109,111]. The order parameter in this approach is the gap (the Dirac mass) in the energy dispersion of relativistic electrons. This gap originates from the spontaneous excitonic condensation catalyzed by the magnetic field (magnetic catalysis). The presence of the gap, Δ, in the energy dispersion splits the lowest Landau level, but does not affect the degeneracy of the highest Landau level. For example, the energies of the lowest Landau levels become $\pm\Delta$ and each level is twofold spin degenerate, while the energies of the higher Landau levels are

$$\varepsilon_n = \pm\sqrt{2\hbar v_F^2 |n| eB + \Delta^2}. \tag{30}$$

Therefore for the higher Landau levels the gap changes only the dispersion relation, but does not change the level degeneracy. This fact has a straightforward effect on the quantization of the Hall conductance. Due to the splitting of only the lowest Landau level, there is an additional Hall plateau at $\nu = 0$. Therefore the graphene system with a dynamically generated gap shows Hall conductance quantization at $\nu = 0$ and $\nu = \pm 4(N + \frac{1}{2})$. Taking the Zeeman splitting into account, Gusynin *et al.* [100] reproduced the quantum Hall effect at $\nu = 0, \pm 1, \pm 2N$, $N = 1, 2, \ldots$. The degeneracy of the highest Landau levels is lifted only by the Zeeman interaction. In Figure 13, a schematic illustration of the Landau quantization with dynamical excitonic gap, Δ, and Zeeman splitting, $\mu_B B$, is shown. There are two types of mass order parameters (dynamical gaps), which can be introduced into the model. The dynamical gaps correspond to singlet and triplet contributions with respect to the valley symmetry group [108,109,111]. In general, the dynamical gap order parameters coexist with quantum ferromagnetic order parameters and should be considered simultaneously [108].

Generation of the dynamical gap in a strong magnetic field was studied in [114] within the extended Hubbard model on a honeycomb lattice. The extended Hubbard model takes into account both on-site and nearest neighbor repulsions. The transition to the charge density wave state and an antiferromagnetic state has been illustrated within the model of [114]. Similar to the magnetic catalysis model [100,108,109,111], the generation of the dynamical gap explains the quantum Hall effect at $\nu = 0$ and ± 1.

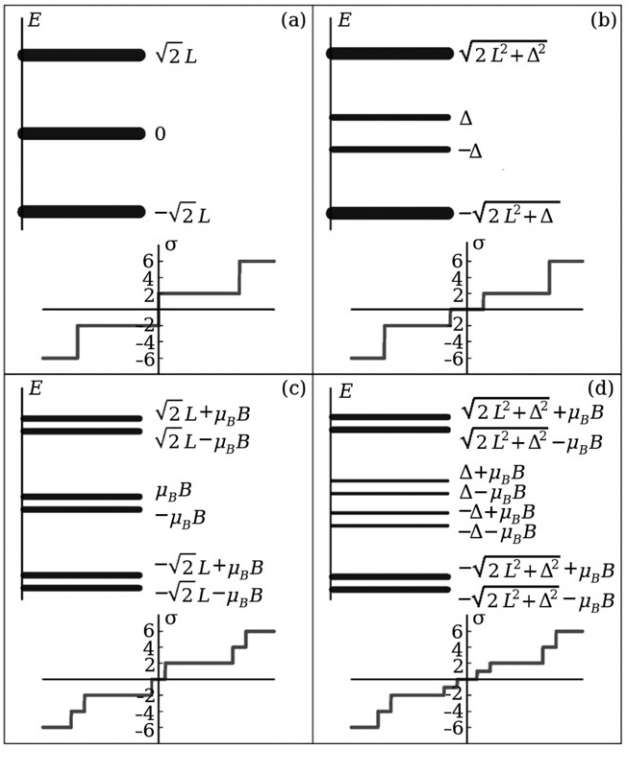

Figure 13. Schematic illustration of the spectrum of the Hall conductivity in $n=0$ and $n=1$ Landau levels for four different cases. (a) $\Delta=0$ and no Zeeman term. (b) Non-zero Δ and no Zeeman term. (c) $\Delta=0$ and the Zeeman term is taken into account. (d) Both Δ and the Zeeman term are non-zero. Thickness of the lines represents the degeneracy $\times 4$, $\times 2$ and $\times 1$ of the level; $L=\sqrt{\hbar v_F^2 eB}$. (Reprinted with permission from V.P. Gusynin *et al.*, Physical Review B, 74, 195429, 2006 [100]. Copyright © by the American Physical Society.)

2.2.5. *Symmetry breaking: lattice distortion*

The twofold valley degeneracy in graphene can be lifted by an out-of-plane lattice distortion [115]. In a perpendicular magnetic field the distortion of the lattice can lower the total energy of the system. This energy includes both the elastic energy of the lattice and the energy of the electronic system. The distortion of the lattice is described as the relative shift of the sublattices A and B towards and away from a substrate by some distance [115]. Due to interaction with the substrate, the sublattices A and B acquire different on-site energies, which effectively results in effective mass of electrons in graphene and lower the energy of electron in the system. Therefore the electrons preferably occupy the sublattice with the lower on-site energy, spontaneously breaking the valley symmetry.

The gain in the energy of electronic system in graphene due to the distortion of the lattice is determined by the strength of the distortion and increases with the magnetic field [115]. This gain should be compared with the energy cost of the distortion, i.e. with the elastic energy of the lattice. Minimization of the total energy

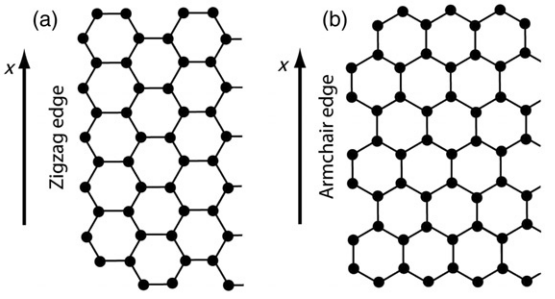

Figure 14. Graphene honeycomb lattice with (a) zigzag and (b) armchair edge terminations.

of the system, which includes the elastic energy of the lattice and the energy of electrons, determines the strength of the spontaneous lattice distortion. A detailed analysis of the graphene system in a magnetic field shows that spontaneous lattice distortion lifts the valley degeneracy only in the lowest Landau level, $n=0$ [115], while the $n>0$ Landau levels remain twofold valley degenerate.

The mechanism of lifting of twofold valley degeneracy based on magnetic-field-induced lattice distortion crucially depends on the asymmetric interaction of graphene layer with substrate. If the interaction with substrate is suppressed, e.g. in a suspended graphene, then the spontaneous lattice distortion does not occur.

The magnetic field can also induce lattice instability and lift the valley degeneracy in a suspended graphene even without a substrate if the graphene surface is curved. The example of such a system is the carbon nanotube. A strong magnetic field perpendicular to the nanotubes axis results in lattice instability towards in-plane or out-of-plane distortions [116–119]. The in-plane instability has the Kekule pattern, which is a network of hexagons with alternating short and long bonds.

2.2.6. *Edge states in a strong magnetic field*

The half-integer quantum Hall effect in graphene can be understood from the viewpoint of the edge states as well. In the edge state description of the quantum Hall effect, the Hall conductance is determined by the number of edge state bands crossing the Fermi level. In graphene there are two main types of edges: (i) armchair edge and (ii) zigzag edge (Figure 14). Even without a magnetic field, these edges have different properties, e.g. at the zigzag edge, zero energy surface states are observed. In a magnetic field the structure of the quantum Hall edge modes also depends on the type of the edge [104,109,120–125].

Within the continuum model, the difference between the two types of edges originates from different boundary conditions imposed at the edge. For the zigzag edges, the wavefunction vanishes on a single sublattice across the edge, while for the armchair edge, the wavefunction vanishes on both sublattices at the edge [122,123]. To find the structure and the energy dispersion of the edge states, the relativistic Dirac equation with appropriate boundary conditions should be solved. For each valley the corresponding wavefunctions are the two-component functions, i.e. ($\psi_{K,A}$, $\psi_{K,B}$) and ($\psi_{K',A}$, $\psi_{K',B}$) for valleys K and K′, respectively. Excluding one of the

components from the Dirac equations, we obtain the system of equations for valleys K and K′ in the following form [123]:

$$\frac{1}{2}\left(-\partial_y^2 + (y - y_p)^2 + 1\right)\psi_{\mathrm{K,A}} = \lambda\psi_{\mathrm{K,A}}; \tag{31}$$

$$\frac{1}{2}\left(-\partial_y^2 + (y - y_p)^2 - 1\right)\psi_{\mathrm{K',A}} = \lambda\psi_{\mathrm{K',A}}, \tag{32}$$

where the edge is along the x axis, the vector potential is $A_x = -By$, $A_y = 0$, and along the x axis the wavefunctions are propagating waves, $\exp(\mathrm{i}p_x x)$. Here $\lambda = (\varepsilon/\varepsilon_0)^2$, $\varepsilon_0 = \hbar v_0 (2eB/\hbar c)^{\frac{1}{2}}$, $y_p = -p_x$, and y and p_x are measured in units of l_B and $\hbar/l_B$, respectively.

Equations (31) and (32) determine the wavefunctions and corresponding energies of the Landau levels in graphene. Without any boundaries the Landau quantization with $\lambda \propto n$, i.e. $\varepsilon \propto \sqrt{n}$, and wavefunctions in the form of Hermite polynomials, $H_n(y - y_p)$, localized at y_p, can be obtained from Equations (31) and (32). The energies of the states do not depend on the electron position, y_p, within the layer, resulting in high degeneracy of the Landau levels. When y_p becomes close to the boundary of the system, the degeneracy of the Landau levels is lifted. Such dispersive edge states can be obtained from Equations (31) and (32) by introducing the corresponding boundary conditions.

Then for the armchair edge termination the boundary condition takes the form

$$\psi_{\mathrm{K,A}} = \psi_{\mathrm{K',A}}, \quad \psi_{\mathrm{K,B}} = \psi_{\mathrm{K',B}} \tag{33}$$

at the boundary and for the zigzag edge the boundary condition is

$$\psi_{\mathrm{K,A}} = 0, \quad \psi_{\mathrm{K',A}} = 0. \tag{34}$$

For higher Landau levels, $|n| > 0$, there is not much difference in the energies of the edge states between the zigzag and armchair terminations. In both cases, the edge boundary conditions violate the valley symmetry at the edge, resulting in lifting of the twofold valley degeneracy at the boundary, shown schematically in Figure 15. For the armchair edge the boundary condition introduces inter-valley mixing, while for the zigzag edge the boundary condition itself violates the valley symmetry, but does not introduce the mixture between the K and K′ valleys. Thus only for the zigzag edge the valley indexes, K and K′, can be assigned to the edge states (Figure 15).

The lowest Landau level ($n = 0$) behaves differently for zigzag and armchair edges. For the armchair edge, the lowest Landau band disperses and there is one pair of particle-like and one pair of hole-like edge states [104,109,120–125]. The appearance of both particle-like and hole-like edge states at $n = 0$ Landau level is a direct manifestation of the relativistic nature of electrons in graphene and can be understood from Equations (27) and (28). The solutions of these equations provide the value of the effective energy, λ, which is proportional to the square of the real energy, $\lambda = (\varepsilon/\varepsilon_0)^2$. Therefore any positive solution of Equations (27) and (28) produce two real solutions: one with positive energy, $\varepsilon = \varepsilon_0\lambda^{\frac{1}{2}}$, and another with the negative energy, $\varepsilon = -\varepsilon_0\lambda^{\frac{1}{2}}$. The states with the positive and negative energies

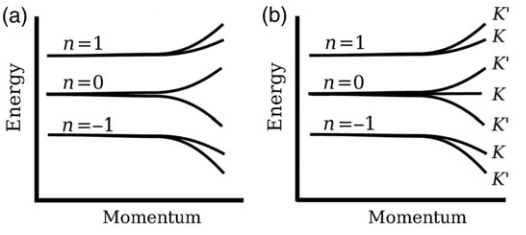

Figure 15. Graphene energy spectrum shown schematically as a function of momentum, p_x, near the armchair (a) and zigzag (b) edges. Here n is the Landau level index. (a) For the armchair edge the boundary condition at the edge introduces inter-valley mixing. In this case the valley indexes, K or K′, cannot be assigned to the edge states. (b) For the zigzag edge the boundary condition violates the valley symmetry and lifts the valley degeneracy. There is no inter-valley mixture for the zigzag edge and each edge state belongs to a specific valley. The corresponding valleys are shown by labels K and K′.

correspond to the particle-like and hole-like states, respectively. By counting the number of edge bands at different positions of the Fermi level, it is easy to see that the existence of particle-like and hole-like states at the zero Landau level explains the half-integer quantum Hall effect.

For the zigzag edge, there are two types of edge states: dispersionless (with zero energy) and current-carrying surface states [104,109,120–125]. These two surface states belong to different valleys. The existence of zero-energy state can be understood from the special structure of the electron wavefunctions at the lowest Landau level. That is, in the K valley the $n=0$ Landau states reside on the B sublattice only which automatically satisfies zigzag boundary conditions, $\psi_{\mathrm{K,A}}=0$. For the K′ valley we obtain the dispersive states, which satisfy $\psi_{\mathrm{K',A}}=0$. Similar to the armchair edge, such boundary condition result in two types of edge states: particle-like and hole-like states. The edge states at the lowest Landau level are shown schematically in Figure 15.

The effect of disorder and electron–electron interactions on the structure of the edge states have been studied in [124], where edge reconstruction has been observed. Such reconstruction is more pronounced for a partially occupied Landau level, i.e. in the regime of the fractional quantum Hall effect.

The properties of the $\nu=0$ quantum Hall state are closely related to the structure of the edge states at the lowest Landau level [126]. The $\nu=0$ state can be attributed to either valley or spin splitting. Depending on whether the spin or valley symmetry is broken, the $\nu=0$ quantum Hall state has completely different properties. The system becomes either quantum Hall metal or quantum Hall insulator. We consider the armchair edge termination, for which the lowest Landau band consists of particle-like and hole-like edge states belonging to two different valleys (Figure 15a). Both types of states are twofold spin degenerate. Therefore the valley symmetry in this case is broken near the edge. If the valley symmetry is also broken in the bulk of the system (Figure 16a), then there are no current-carrying edge states at zero energy (Fermi level) and the system shows insulating properties. The edge levels in this case are twofold spin degenerate. If the spin symmetry is broken in the bulk of the graphene layer (Figure 16b) then at zero energy there are counter-propagating

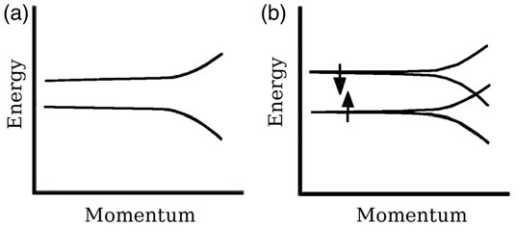

Figure 16. Energy spectrum of graphene shown schematically as a function of momentum, p_x, near the armchair edge for the lowest Landau level: (a) the case of broken valley symmetry (valley-polarized $\nu = 0$ quantum Hall state); (b) the case of broken spin symmetry (spin-polarized $\nu = 0$ quantum Hall state). The arrows next to the lines illustrate the direction of spin at the corresponding energy levels.

gapless edge modes [126]. In the experiments [92] the $\nu = 0$ quantum Hall system shows a peak in the magnetoresistance near the Dirac point (zero energy). This observation supports the picture of spin symmetry breaking as the origin of $\nu = 0$ quantum Hall state [126]. In [127], a simple technique has been proposed to measure the chirality of the quantum Hall edge states. This method can be used to clarify the nature of the edge states at the $\nu = 0$ quantum Hall effect.

The properties of counterpropagating edge states of opposite spin at $n = 0$ Landau level have been explored in [128] to explain the results of the experiment reported in [94], where the transition from the metallic to an insulating $\nu = 0$ quantum Hall state was observed. In [128], magnetic impurities were also introduced. Such impurities can flip the electron spin and introduce backscattering between the counterpropagating edge states. Each edge model is described as a one-dimensional Luttinger liquid with Luttinger parameter $\mathcal{K}$. The value of the parameter depends on the magnetic field strength and the details of the edge potential. In such a system the Kondo (magnetic) impurities introduce the critical value, $\mathcal{K}_c$, of the parameter $\mathcal{K}$, so that for $\mathcal{K} > \mathcal{K}_c$ the system is in an insulating state, while for $\mathcal{K} < \mathcal{K}_c$ it is in a metallic phase.

The condition of the existence of the gapless edge states in graphene with zigzag and armchair edges was analyzed in [109] within the approach based on the dynamical generation of the Dirac mass gap due to the magnetic catalysis. The condition is determined by the relative strength of the mass order parameters and the quantum Hall ferromagnetic order parameters.

2.3. *Fractional quantum Hall effect*

Observation of the fractional quantum Hall effect [72,73] in high-mobility planar electron gas at large magnetic fields allows one to study the collective behavior of two-dimensional electrons. Theoretical aspects of this problem in graphene have been addressed in a few publications [129–133], where a finite size system has been studied within the scheme of direct diagonalization of the Hamiltonian matrix or within the trial-wavefunction approach. The properties of the fractional quantum Hall effect in graphene can be determined by Haldane's pseudopotentials, V_m [134],

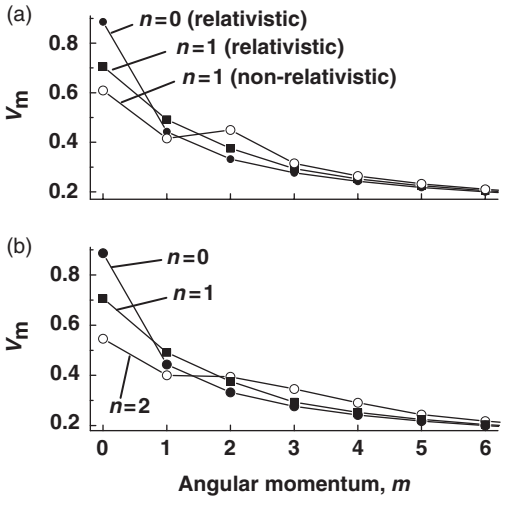

Figure 17. Pseudopotentials calculated from Equation (35) are shown as a function of the relative angular momentum (a) for relativistic and for non-relativistic two-dimensional electrons in the first two Landau levels, and (b) for relativistic electrons in various Landau levels. The energies are measured in units of $e^2/\varepsilon l_B$ (reproduced from [129]).

which are the interaction energies of two electrons with relative angular momentum m. The pseudopotentials for the nth Landau level has the following form [129,130,132,133]

$$V_m^{(n)} = \int_0^\infty \frac{\mathrm{d}q}{2\pi} q V(q) [F_n(q)]^2 L_m(q^2) \mathrm{e}^{-q^2}, \tag{35}$$

where $V(q) = 2\pi e^2/(\epsilon l_B q)$ is the Coulomb interaction in the momentum space, and $F_n(q)$ is the form factor corresponding to the nth Landau level (see Equations (28) and (29)). For non-relativistic electrons in graphene, the corresponding form factors are $F_n(q) = L_n(q^2/2)$. Comparing this expression with Equations (28) and (29), it is possible to see that the inter-electron interactions for the relativistic and non-relativistic electrons are same for $n = 0$ and different for $n > 0$.

In Figure 17 the pseudopotentials for relativistic and non-relativistic systems are shown. The behavior of the relativistic and non-relativistic pseudopotentials are clearly different. For relativistic electrons, the suppression of the pseudopotential for $n = 1$ as compared to $n = 0$ occurs only for $m = 0$, while for all other values of m, we have $V_m^{(1)} > V_m^{(0)}$. For non-relativistic electrons, there is also a suppression of the pseudopotential for $m = 1$. The behavior of relativistic pseudopotentials for different Landau levels is shown in Figure 17(b). At all values of the relative angular momentum, m, except for $m = 1$, there is a monotonic dependence of the pseudopotentials on the Landau level index, n: the pseudopotential decreases with increasing n for $m = 0$ and increases with increasing n for $m > 1$. In contrast, for the angular momentum $m = 1$, the dependence of the pseudopotential on the Landau index is non-monotonic: the pseudopotential has the maximum value at $n = 1$.

The special dependence of the relativistic pseudopotential on the angular momentum and Landau level index has a profound influence on the interaction energy scale of the fractional quantum Hall states at different Landau levels [129,130,132,135]. By looking at the values of the pseudopotentials we can reach a conclusion about the relative strength and stability of the fractional quantum Hall effect in graphene, as compared to the conventional non-relativistic systems. For example, since the electron wave functions at the lowest Landau level in graphene are identical to the lowest Landau level wavefunctions in the conventional (non-relativistic) electron systems, the relativistic pseudopotentials at $n=0$ in graphene are exactly equal to the corresponding pseudopotentials of the non-relativistic systems [129]. Therefore, without the inter-Landau level coupling, the properties of the fractional quantum Hall state at $n=0$ Landau level in graphene are the same as for the non-relativistic systems. The specific feature of the quantum Hall system in graphene is that the electrons now have spin and valley degrees of freedom, which would open up the possibility for spin and valley-polarized or unpolarized ground states and the corresponding excitations. The relativistic pseudopotentials at $n>0$ Landau levels are different from those in the non-relativistic systems. As a result, the fractional quantum Hall states at the $n>0$ Landau levels should have different properties compared to the non-relativistic systems [129]. Since at the $n=1$ Landau level the pseudopotentials are enhanced compared to the non-relativistic ones, the fractional quantum Hall states at the $n=1$ Landau level should be more stable in the relativistic graphene system.

Apalkov and co-workers [129,130] investigated the energy spectra of the fractional quantum Hall states in graphene for a finite-size system within the spherical geometry [72], where the magnetic field strength is determined by the magnetic field fluxes, $2S$, though the sphere in units of the flux quanta. Here $2S$ is an integer and S is also the angular momentum of the single-electron states. It was shown that the ground state of $\nu=\frac{1}{3}$ and $\nu=\frac{1}{5}$ are spin and valley polarized at both $n=0$ and $n=1$ Landau levels [130]. The excitation gaps in the fractional quantum Hall systems are determined by the interaction strength at the corresponding Landau levels. The results shown in Figures 18 and 19 for $\nu=\frac{1}{3}$ and $\frac{1}{5}$ quantum Hall states at $n=0$ and $n=1$ Landau levels clearly illustrate the enhancement of the energy scale at the $n=1$ Landau level compared to that at the $n=0$ Landau level. That is, both valley-polarized and valley unpolarized excitation gaps at the $n=1$ Landau level are larger than those at the $n=0$ Landau level. This enhancement is especially pronounced for the $\nu=\frac{1}{3}$ state, for which the pseudopotential at small values of the angular momentum determine the inter-electron interaction strength. At $\nu=\frac{1}{5}$ the excitation spectra for the $n=1$ and $n=0$ Landau levels are almost the same. Although larger energy gaps at $n=1$ Landau level are observed for the $\nu=1/m$ states, this is not a general rule for other fractional Hall states. The pseudopotential at zero relative angular momentum, $m=0$, is the strongest for the $n=0$ Landau level. Therefore, for the fractional quantum Hall states for which the on-site interaction with $m=0$ is dominant, the energy gap in the $n=0$ Landau level is the largest. An example of such a fractional quantum Hall state is the $\nu=\frac{2}{3}$ state. The excitation gap of the valley-unpolarized $\nu=\frac{2}{3}$ state is larger in the $n=0$ Landau level than that for the $n=1$ Landau level.

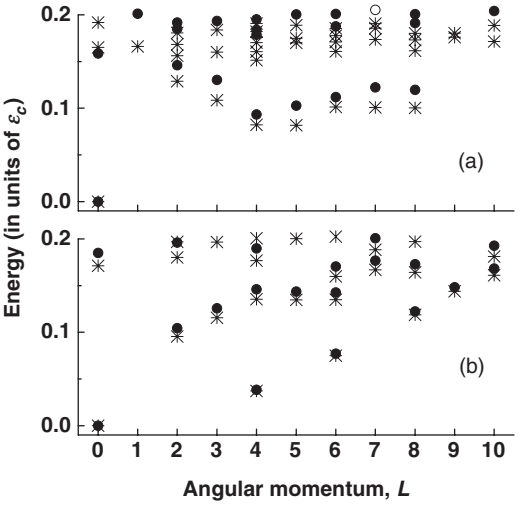

Figure 18. The energy spectra of an eight-electron valley-polarized $\nu = \frac{1}{3}$ fractional quantum Hall system obtained in spherical geometry are shown for different Landau levels: $n = 0$ (stars) and $n = 1$ (full circles). The flux quanta is $2S = 21$. (b) The energy spectra of a six-electron valley-polarized $\nu = \frac{1}{5}$ system is shown for different Landau levels: $n = 0$ (stars) and $n = 1$ (full circles). The flux quanta is $2S = 25$. The energy is shown in units of the Coulomb energy, $\varepsilon_C = e^2/\varepsilon l_B$ (reproduced from [130]).

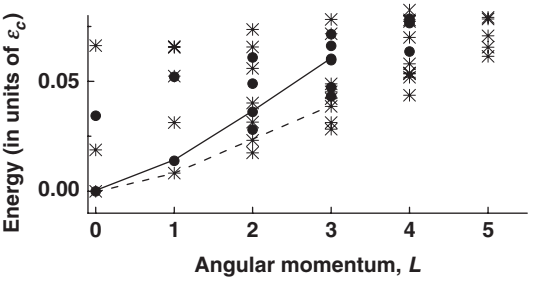

Figure 19. The energy spectra of a six-electron valley-unpolarized $\nu = \frac{1}{3}$ fractional quantum Hall system obtained in the spherical geometry, are shown for different Landau levels: $n = 0$ (stars) and $n = 1$ (full circles). The flux quanta is $2S = 15$. The spin-wave excitations are illustrated by solid ($n = 1$) and dashed ($n = 0$) lines. The energy is shown in units of the Coulomb energy, $\varepsilon_C = e^2/\varepsilon l_B$ (reproduced from [130]).

The single-particle excitations of the fractional quantum Hall states were studied in [135] within a numerical approach. It was shown that at $\nu = \frac{1}{3}$ the excitations are valley skyrmions both at $n = 0$ and $n = 1$ Landau levels. A more complicated situation occurs for the $\nu = \frac{2}{3}$ and $\nu = \frac{2}{5}$ fractional quantum Hall states. The ground states in these two cases are valley-unpolarized at $n = 0$ Landau level and valley-polarized in the $n = 1$ Landau level. The single-particle excitations are valley-unpolarized except at the $\nu = \frac{2}{5}$ state in the $n = 1$ Landau level, for which the excitation has the skyrmion-like valley texture.

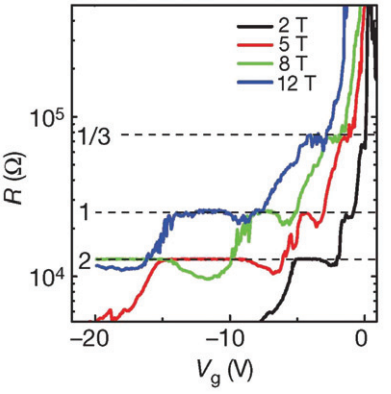

Figure 20. Gate voltage dependence of resistance for a suspended graphene sample is shown at different magnetic fields and at temperature 1.2 K. The plateaus at $\nu = 1, 2$ and $\frac{1}{3}$ are clearly visible. (Reprinted with permission from X. Du *et al.*, Nature, 462, p.192, 2009 [95]. Copyright © (2009) Nature Publishing Group.)

In [136], the ground state of the electron system with partial filling factor was studied within a mean-field approach. The competition between the uniform state, Wigner crystal (with one electron per unit cell) and the bubble crystal (with more than two electrons per unit cell) was considered. It was shown that at all filling factors (except integer) the Wigner crystal state has the lowest energy at the lowest Landau levels, $n = 0, 1$. At $n > 1$ a bubble crystal with two electrons per unit cell is realized at intermediate values of the filling factor, while at all other filling factors the Wigner crystal state occurs. This approach does not take into account the strongly correlated fractional quantum Hall states (Laughlin liquids) [72,73] realized at special fractional filling factors, e.g. $\nu = \frac{1}{3}$. Such states will have the lowest energy at these filling factors.

The fractional quantum Hall effect has been recently observed experimentally [95,96] in specially prepared suspended graphene samples. In such suspended samples, the disorder, which is usually due to the substrate, is strongly suppressed, which has made it possible to observe the fractional quantum Hall effect at the filling factor $\frac{1}{3}$ (Figure 20). The fractional quantum Hall state is a strongly correlated electron state, which at $\nu = \frac{1}{3}$ is the Laughlin liquid state [137]. The activation gap of such a state is determined by the strength of the inter-electron interaction, i.e. by the Coulomb energy, $\varepsilon_C = e^2/\varepsilon l_B$. The activation gap of the $\nu = 1/3$ quantum Hall state was analyzed in [138] based on the two-terminal conductance measurements [95,96]. The activation gap was found to be around 4.4 K and the corresponding fractional quantum Hall effect is clearly visible up to 10 K (the fractional quantum Hall effect in conventional 'non-relativistic' systems usually appear at much lower temperatures, i.e. below 1 K). The experimentally obtained activation gap is much smaller than the theoretically predicted value which, for the experimental parameters of [95,96] is around 40 K [138]. This discrepancy can be attributed to the presence of disorder in the system. Observation of the strong enhancement of interaction effects in suspended graphene can be clearly attributed to the small value of the dielectric constant, $\varepsilon \approx 1$, in suspended graphene.

3. Bilayer graphene

Bilayer graphene consists of two graphene monolayers, typically arranged in the Bernal (AB) stacking arrangement. It is a fascinating and complex system in its own right, distinct from both the monolayer and the traditional two-dimensional electron system (2DES) even though it shares some characteristics of each. The study of bilayer graphene started in 2006 with the publication of three papers describing its properties for the first time [139–141]. McCann *et al*. [139] demonstrated that the low-energy band structure of neutral bilayer graphene is gapless and exhibits a variety of second-order effects, and described an unusual sequence of Landau levels. Experimental descriptions of this material were published by Ohta [140], who described the low-energy band structure as well as the formation of a gap at the K point when a transverse electric field is applied (in this case by negatively charged dopants), and by Novoselov *et al*. [141] who measured the quantized Hall conductance as predicted by McCann and Falko. In addition to the quadratic low-energy band structure, with its associated effective mass, the chiral nature of the charge carriers is manifest in the Berry's phase and other properties. The bilayer shares many other physical properties with the monolayer, such as the exceptionally high electron mobility (with mean free path in the sub-micron range), and high mechanical stability. Massive chiral particles do not exist in standard field theory, and this makes the bilayer graphene system a promising venue in which the effects of chirality can be distinguished from those of the Dirac spectrum in comparison with monolayer graphene and traditional 2DESs. One unique feature of bilayer graphene is the ability to open a tunable band gap by engineering a potential difference between the two layers. This may be done either by gating, or by external dopants. This tunable gap (as opposed to the gap in a 2DES which is an intrinsic effect of the crystal structure and therefore not tunable), along with the high electron mobility and simplicity of fabrication techniques opens the possibility of many applications of bilayer graphene in the construction of devices.

Here we present a summary of the properties of this material, and in particular seek to show the similarities and differences between it and the monolayer. We begin in Section 3.1 by discussing the fabrication and identification of bilayer flakes from an experimental point of view. Then, in Section 3.2, the commonly-used tight-binding model is introduced including the effective low-energy description. In Section 3.3 we review the theoretical predictions for the opening of a band gap at the K points, and discuss the experimental evidence for this gap. When bilayer graphene is placed in a strong magnetic field, it exhibits a unique integer quantum Hall effect, and this is reviewed in detail in Section 3.4. The impact of electron–electron interactions is often neglected in the theoretical work, but they may have important consequences and we review analytical and numerical studies of their effects in Section 3.5. Phonon anomalies in this material, and the coupling between electrons and phonons are discussed in Section 3.6, and finally we present a few of the devices which have been proposed to utilize bilayer graphene in Section 3.7.

3.1. *Sample fabrication and identification*

Fabrication techniques for bilayer graphene are similar to those for the monolayer material. In the case of mechanically exfoliated flakes, the 'Scotch tape' part of the

process deposits many flakes of varying thicknesses onto the substrate, so the process of identifying which flakes are mono- or bilayers becomes the key part of the technique. Bilayer samples have also been made on silicon carbide substrates by the sublimation of the silicon atoms on heating, a process called epitaxial growth. In this section, we describe the optimization of the visibility of graphene, and in particular the ideal conditions for distinguishing the number of layers of exfoliated flakes. We then review other diagnostic techniques, such as atomic force microscopy and Raman spectroscopy which proved to be useful tools in characterizing graphene.

3.1.1. *Optical identification of exfoliated bilayer graphene*

The visibility of graphene is a key issue for the mechanical microcleavage fabrication technique, and in 2007, four papers were published [142–145] discussing the visibility of graphene and few-layer graphene on dielectric substrates. Defining the optical contrast (or visibility) to be

$$V = (R - R_0)/R_0,$$

where R_0 is the reflection coefficient of the bare substrate, and R is the reflection coefficient of the substrate with a graphene flake present, all authors reported that the visibility of the bilayer is twice as high as that of the monolayer in the visible frequency range. All authors also recommended using substrates with SiO_2 of width $\approx$280 nm. While Blake *et al.* [142] modelled the enhanced reflection of visible light due to constructive interference of light caused by the additional optical path length introduced by the presence of graphene, Abergel *et al.* [143] gave a complimentary analysis considering the effect of the conductivity of the graphene flake at the boundary between the air and the substrate. They gave an analytical condition for the peak visibility, finding that the frequency of incident light ω, the oxide width d, and dielectric function ε_o should be arranged such that

$$\omega \approx \frac{c\left(n + \frac{1}{2}\right)\pi}{d\sqrt{\epsilon_o}\cos\alpha_o}, \tag{36}$$

where n is an integer which labels the resonance, c is the speed of light and $\sin\alpha_o = \sin\alpha/\sqrt{\epsilon_o}$. This approach was supplemented by Nair *et al.* [146] in the publication of measurements of the absorption of visible light by suspended graphene, showing that the absorption scales linearly with the number of layers for energies below about 1 eV and that the constant of proportionality is exactly the fine structure constant $\alpha = e^2/\hbar c$ (Figure 21). Abergel *et al.* [143] noted that since the optical conductivity of bilayer graphene has a peak at $\gamma_1 \approx 400$ meV, then the visibility of the bilayer will be enhanced with respect to the monolayer in the far infra-red frequency range. This was subsequently observed by Kuzmenko *et al.* [147].

Wang *et al.* [148] discussed several pertinent differences between the monolayer and bilayer optical properties, including the van Hove singularity which is present in the bilayer, but not in the monolayer. This effect causes the sign of the peak normalized reflectivity to be opposite in the two materials. Additionally, the normalized reflectance exhibits a peak when the photon energy is

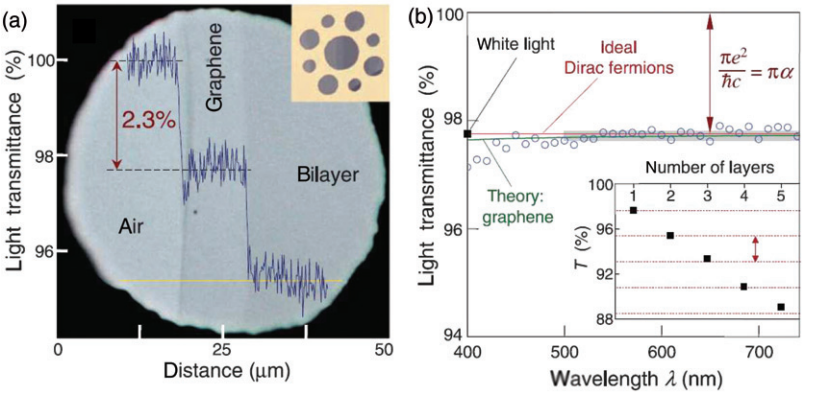

Figure 21. (Colour online) Looking through one-atom-thick crystals. (a) Photograph of a 50 μm aperture partially covered by graphene and its bilayer. The line scan profile shows the intensity of transmitted white light along the yellow line. (Inset) The sample design: A 20 μm thick metal support structure has several apertures of 20, 30, and 50 μm in diameter with graphene crystallites placed over them. (b) Transmittance spectrum on single layer graphene (open circles). Slightly lower transmittance for $\lambda < 400$ nm is probably due to hydrocarbon contamination. The red line is the transmittance $T = (1 + 0.5\pi\alpha)^{-2}$ expected for two-dimensional Dirac fermions, whereas the green curve takes into account a non-linearity and triangular warping of graphene's electronic spectrum. The gray area indicates the standard error for the measurements. (Inset) Transmittance of white light as a function of the number of graphene layers (squares). The dashed lines correspond to an intensity reduction by $\pi\alpha$ with each added layer (Reprinted figure with permission from R.R. Nair *et al.*, Science, 320, 1308, 2008 [146]. Copyright © (2008) The American Association for the Advancement of Science.).

equal to the interlayer coupling energy γ_1 corresponding to the inter-band excitations becoming accessible. The gate-induced changes in the reflectivity are also significantly different, with the monolayer showing a difference which is roughly constant with the photon energy, but the bilayer peaking at γ_1. Note that the detail explanation of the theory of optical conductivity can be found in [149–151].

Ni *et al.* [152] measured the visibility of multi-layered graphene on an SiO_2 substrate, and fitted their data to the bulk graphite refractive index ($n_G = 2.6 - 1.3i$). They did not find good agreement between the calculations using Fresnel's equations and the experiment, and instead found that the refractive index $n = 2.0 - 1.1i$ fitted better.

Abergel *et al.* [143] also discussed the visibility of graphene on SiC substrates, Roddaro *et al.* [144] presented computations of the observed color of the graphene flakes, Casiraghi *et al.* [145] discussed Raleigh spectroscopy and flakes with larger numbers of layers, and also the dependence of the visibility on the aperture size of the detection device. Gaskell *et al.* [153] measured the contrast in reflection for graphene flakes mounted on glass substrates and also found a linear increase in visibility with the number of layers, linking this to the fine structure constant (Figure 22), after Nair *et al.* [146]. Gao *et al.* proposed a method for flake identification which utilized the color difference between the substrate and the graphene, and discussed various alternative dielectric materials for use in the substrate.

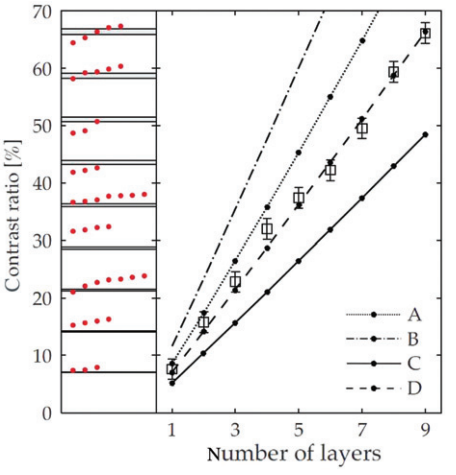

Figure 22. Left: Measured contrast ratios for 41 unique graphitic flakes. Theoretical contrast ratios based on the Fresnel theory with m-layer graphene conductance $Z_0G = m\pi\alpha$ are plotted as bands for a substrate refractive index $n_s = 1.522 \pm 0.004$. Right: Contrast ratios for each layer, including error due to camera non-linearity and lamp power fluctuation, compared with Fresnel theory with reported graphite induces (A) $n_g = 2.675 - 1.35i$ [154], (B) $n_g = 2.52 - 1.94i$ [155], graphene index reported by Ni *et al.* [152] (C), and universal conductance (D) (Reprinted figure with permission from P.E. Gaskell *et al.*, Applied Physics Letters, 94, 143101, 2009 [153]. Copyright © (2009) American Institute of Physics.).

3.1.2. *Atomic force microscopy and miscellaneous diagnostic techniques*

Atomic force microscopy is a technique which can be employed to measure the relative height of a graphene flake above the substrate, and thus determine the number of layers present in the flake. Obraztsova *et al.* [156] carried out a statistical analysis of the atomic force microscopy (AFM) measurements of the height of many graphene flakes to determine the systematic dependence of the height on the number of layers. They demonstrated (Figure 23) that the peaks in the histograms of measured heights occur at 0.35 nm intervals, corresponding to the predicted interlayer spacing in few-layer graphite flakes. The height of the first layer in a given flake varies due to the differing strength of interactions between the substrate and the flake, and the height of graphene in one plateau varies due to the intrinsic rippling or corrugation of the flake. Their study shows that the flake height is a reliable way of determining the number of layers on a plateau on a given flake, but the low throughput of the AFM technique means that other diagnostic techniques are more promising for the identification stage of the exfoliation fabrication method.

Stacking faults have been observed by Warner *et al.* [157] in exfoliated bilayer and few-layer samples by tunnelling electron microscopy (TEM) measurements. The relative rotation of the layers can be distinguished and the experimental data is fitted well by considering two decoupled monolayers. High-resolution TEM is a good tool for determining the stacking faults for flakes up to six layers thick.

When bilayer graphene is deposited on a (metallic) ruthenium substrate [158], the upper layer is screened from the substrate by the lower layer, which couples strongly to the metal. The authors claim that the linear band structure is regained in the upper

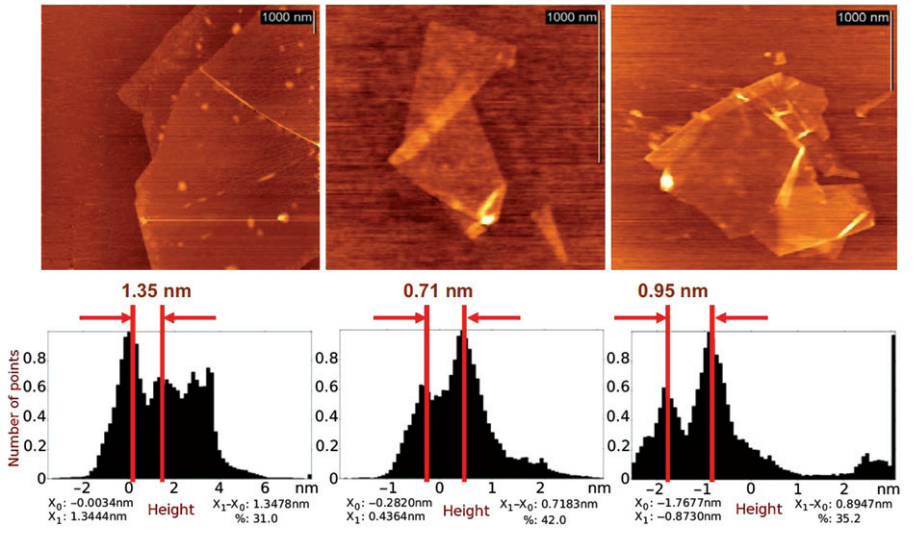

Figure 23. The atomic force microscopy images of three different arbitrary graphene flakes and the distribution of the height values over their surface points (Reprinted with permission from E.A. Obraztsova, A.V. Osadchy, E.D. Obratztsova, S. Lefrant, and I.V. Yaminsky, Physica Status Solidi b, 245, p. 2055, 2008 [156]. Copyright © (2008) Wiley-VCH Verlag GmbH & Co. KGaA.).

layer, and that scanning tunnelling microscopy (STM) images of the flake show both carbon sublattices indicating that the AB symmetry is restored.

3.1.3. *Raman spectroscopy*

Both the optical imaging and AFM methods of determining the number of layers in a graphene flake are time-consuming processes. Raman spectroscopy has a much higher throughput, and is therefore a promising candidate for a much faster identification technique, and several authors have claimed that it can reliably distinguish the number of layers in a flake. Raman spectroscopy is intimately related to the phonon modes in the sample being probed. Ferrari *et al.* [23] have shown that the doubly-degenerate 2*D* peak in monolayer graphene splits into four non-degenerate modes in the bilayer. This splitting causes the 2*D* peak to broaden in a systematic way (Figure 24a), to gain a shoulder on its low-energy tail, and to shift slightly upward in frequency. This is also seen in experiments carried out by Graf *et al.* [159], where spatially-resolved Raman spectroscopy can distinguish between mono- and bilayer portions of a single flake (Figure 24b). Also noticeable in this figure is a dramatic increase of intensity, and a slight downward shift (by $\approx 3\,\mathrm{cm}^{-1}$) of the *G* peak, relative to the monolayer.

The Raman spectrum of two overlapping monolayer flakes has been investigated by Poncharal *et al.* [160]. Figure 25(a) shows the *G* and *D* band regions of the 633 nm Raman trace of monolayer and overlapping graphene. There is a slight downward frequency shift and narrowing of the *G* peak in the overlapping flakes. Figure 25(b) shows the trace for the 2*D* band in the same flakes, with that of the Bernal stacked bilayer for comparison. The splitting of the 2*D* band into four peaks

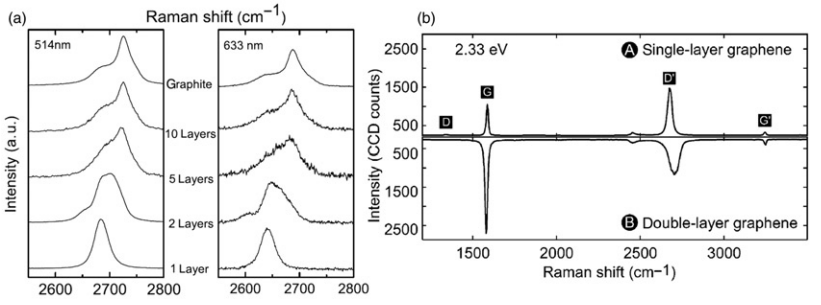

Figure 24. (a) The 2D peak shown in Raman spectra in bilayer graphene (Reprinted figure with permission from A.C. Ferrari *et al.*, Physical Review Letters, 97, 187401, 2006 [23]. Copyright © (2006) by the American Physical Society.). (b) Raman spectra of single- and double-layer graphene (Reprinted with permission from D. Graf *et al.*, Nano Letters, 7, 238, 2007 [159]. Copyright © (2007) by the American Chemical Society.).

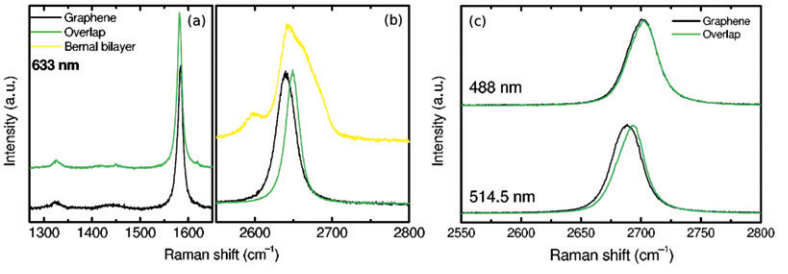

Figure 25. (Colour online) (a),(b) Raman spectra of a single graphene sheet (black lines), Bernal bilayer (yellow lines) and two overlapping misoriented graphene sheets (green lines) at 633 nm. (a) *G* and *D* band range of the graphene and overlapping configuration. Curves have been vertically offset for clarity and normalized on the *G* peak. (b) 2*D* band region for single graphene sheet and overlap compared to the Bernal-stacked bilayer. The overlapping graphene spectrum consists of a single peak clearly shifted compared to monolayer graphene. It strongly differs from the Bernal-stacked bilayer. Its width (19 cm^{-1}) is smaller than the monolayer graphene peak (26 cm^{-1}). (c) Raman spectrum at 488 nm (top) and 514.5 nm (bottom). The difference in Raman shift is reduced compared to the traces at 633 nm in (a, b). The slight asymmetry is due to experimental shortcomings (Reprinted figure with permission from P. Poncharal *et al.*, Physical Review B, 78, 113407, 2008 [160]. Copyright © (2008) by the American Physical Society.).

in the bilayer is completely absent from the overlapping region. Therefore, the authors conclude that the coupling between the two layers in the overlapping region is minimal. However there is an upward shift in the peak frequency, and the peak is ~20% narrower than in the monolayer case. The authors describe why they think (in contrast to other works, [161,162]) that neither the renormalization of the Fermi velocity nor the opening of a gap at the charge neutrality point cause this frequency shift. Instead, they suggest that the weak coupling between the two monolayers causes a modification of the phonon spectrum, which manifests in Raman trace while leaving the electronic spectrum unaltered.

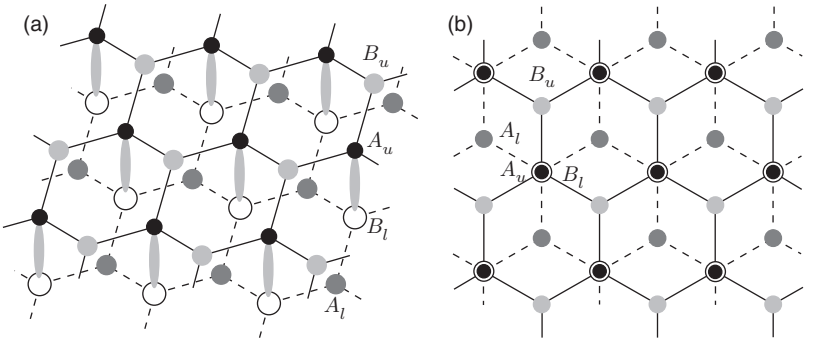

Figure 26. The bilayer lattice in (a) isometric, and (b) top-down projections. The upper (lower) layer is shown in solid (dashed) lines, the interlayer dimer bonds are in grey. The A atoms in the top layer are directly above the B atoms in the lower layer.

3.2. *Tight-binding model*

In this section we introduce the commonly-used tight-binding model for bilayer graphene. It is a natural extension of the model used for the monolayer, although additional complexity is introduced by the various interlayer hopping elements. We shall describe each of these and the effect that they have on the low-energy spectrum. Discussion of the interlayer potential is deferred until Section 3.3.

3.2.1. *Nearest neighbor and next-nearest neighbor models*

The bilayer crystal lattice is shown in Figure 26. The two monolayer lattices are shown as solid lines for the upper lattice (where the two lattice sites are labelled by a subscript '*u*') and the lower lattice in dashed lines (labelled by a subscript '*l*'). The two lattices are offset from each other in the *xy* plane so that the A_u sublattice is directly above the B_l sublattice, and it is between these pairs of atoms that the interlayer dimer bonds are formed. The B_u and A_l atoms are not directly bonded to the opposite layer. This arrangement is known as Bernal stacking, and is the stacking arrangement which is most commonly considered. Other possible arrangements are AA stacking, where the two lattices are directly above each other and bonds form between the same sublattices, and the turbostratic arrangement where the upper layer is rotated with respect to the lower layer and so interlayer bonding is haphazard and noticeably weaker. The AB stacking arrangement was experimentally verified in epitaxial graphene by Ohta *et al*. [163].

In order to construct the tight-binding model for bilayer graphene, we follow the same scheme as for the monolayer. Assuming that the sp^2-hybridized electrons are inert, we consider the p_z electrons only, which form the π bands as in the monolayer.[4] Since there are four atomic sites per unit cell, the wave function can be written as a four component spinor in the following basis:

$$\{\psi_{A_l}, \psi_{B_u}, \psi_{A_u}, \psi_{B_l}\}.$$

The intralayer nearest neighbor hopping elements (characterized by the vectors such as $\vec{R}$ in Figure 27(b)) with the transfer integral t (which was also denoted by γ

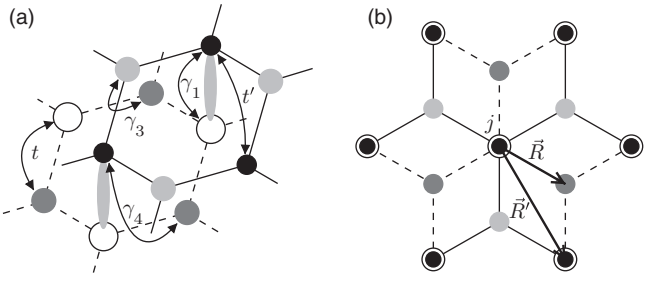

Figure 27. (a) Designation of couplings in the tight-binding model of bilayer graphene. Intralayer couplings are the nearest neighbor ($A \leftrightarrow B$) with energy t, and the next-nearest neighbor ($A \leftrightarrow A$ and $B \leftrightarrow B$) with energy t'. Interlayer couplings are $A_u \leftrightarrow B_l$ with energy γ_1; $A_l \leftrightarrow B_u$ with energy γ_3; and $A_u \leftrightarrow A_l$ and $B_u \leftrightarrow B_l$ with energy γ_4. (b) Illustration of the twelve nearest and next-nearest neighbor lattice sites about site j. The vectors R and R' appear in the tight-binding formalism.

in Section 2.2) and the next-nearest neighbor hops with vectors like $\vec{R}'$ and transfer integral t' are trivially the same as in the monolayer case, so we concentrate on describing the various interlayer couplings, which are illustrated in Figure 27(a). The most important interlayer coupling is the dimer bond between the A_u and B_l lattice sites. The strength of this coupling is parametrized by the transfer integral γ_1, and since there is no projection of the vector connecting these two lattice sites on the xy plane, there is no momentum dependence in the matrix element. The next-nearest neighbor interlayer couplings are the $A_l \leftrightarrow B_u$ hops parametrized by γ_3, and the $A_l \leftrightarrow A_u$ and $B_l \leftrightarrow B_u$ hops parameterized by γ_4. In each case, the momentum dependence is the same function $f(\vec{k})$ as for the intralayer nearest neighbor hops. Finally, the presence of the dimer bond may induce an additional asymmetry between the two sublattices within each layer, which we account for this by including the parameter Δ. Therefore, the tight-binding Hamiltonian for the π bands of neutral bilayer graphene can be written as

$$\mathcal{H}_\pi = \begin{pmatrix} t'g(\vec{k}) & \gamma_3 f(\vec{k}) & \gamma_4 f(\vec{k})^* & tf(\vec{k})^* \\ \gamma_3 f(\vec{k})^* & t'g(\vec{k}) & tf(\vec{k}) & \gamma_4 f(\vec{k}) \\ \gamma_4 f(\vec{k}) & tf(\vec{k})^* & \Delta + t'g(\vec{k}) & \gamma_1 \\ tf(\vec{k}) & \gamma_4 f(\vec{k})^* & \gamma_1 & \Delta + t'g(\vec{k}) \end{pmatrix}, \tag{37}$$

where $f(\vec{k}) = \sum_{i=1}^{3} \exp(i\vec{k} \cdot \vec{R}_i)$, $g(\vec{k}) = \sum_{i=1}^{6} \exp(i\vec{k} \cdot \vec{R}'_i)$, and the superscript asterisk denotes complex conjugation. The values of the transfer matrix elements which appear in the Hamiltonian are still controversial. It seems that they may vary between exfoliated and epitaxial graphene, and theoretical calculations do not currently agree completely with experimental measurement. In Table 1 we collect the values as currently known. The most thorough experimental determination of the tight-binding parameters was carried out by Kuzmenko *et al.* [164], who used infra-red spectroscopy to compare detailed reflection spectra with the predictions of the tight-binding model. They fitted their data to nine free parameters, including the four tight-binding parameters shown in Table 1, the interlayer gap, scattering rate, temperature and position of the charge-neutrality point. The spectrum

Table 1. Tight-binding parameters for bilayer graphene, given in eV.

	$t \equiv \gamma$	γ_1	γ_3	γ_4	Δ
Kuzmenko [147] (IR spec.)		0.378			0.015
		(0.005)			(0.005)
Kuzmenko [164] (IR spec.)	3.16	0.381	0.38	0.14	0.022
	(0.03)	(0.003)	(0.06)	(0.03)	(0.003)
Zhang [165] (IR spec.)	3.0	0.40	0.3	0.15	0.018
Malard [166] (Raman)	2.9	0.30	0.10	0.12	
Malard [167] (Raman)	3.0	0.35	0.13	0.13	
Min [168] (*ab initio*)	2.6	$\approx$0.34	0.3		
Gava [169] (*ab initio*)	−3.4013	0.3963	0.3301	0.1671	

Notes: Methods of determination of the parameters include infra-red spectroscopy (IR spec.), Raman spectroscopy (Raman), and *ab initio* density functional theory calculations (*ab initio*). Note that Min *et al.* claim that γ_1 varies slightly with the interlayer potential U. Bracketed values are stated uncertainties.

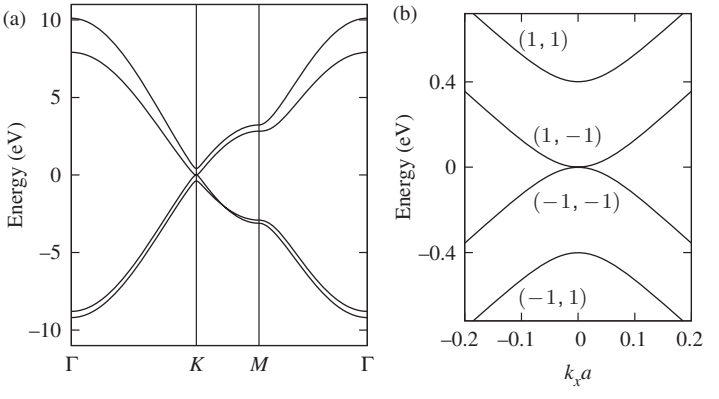

Figure 28. (a) The π bands in bilayer graphene along the high symmetry directions. The tight-binding parameters are taken from Zhang [165]. We have ignored the intra-plane next-nearest neighbor hopping parametrized by t' (i.e. we have set $t' = 0$). (b) The low-energy spectrum for $k_y = 0$ in the nearest neighbor tight-binding model, (i.e. for $\gamma_3 = \gamma_4 = t' = \Delta = 0$). The bands are labelled by the pair of values (χ, α) (Equation (39)). The higher energy bands ($\alpha = 1$) are split by γ_1 from the low-energy bands ($\alpha = -1$), which are degenerate exactly at the K point. In this case, all four bands are isotropic.

associated with this Hamiltonian is shown in Figure 28, where we have taken the tight-binding parameters given by Zhang *et al.* [165].

Mucha-Kruczyński *et al.* [170] have proposed a method for determining the size and sign of various tight-binding parameters by utilizing angle-resolved photoemission spectroscopy (ARPES) data. Variation of the intensity of constant energy maps reveal the wave function symmetry due to trigonal warping, band gaps and intralayer site asymmetry. The location of the bottom of the split band immediately gives the size of the interlayer coupling γ_1, and for energies greater than γ_1, the relative intensity of the signal from the low-energy and split bands determines the sign of this parameter. The magnitude and direction of the trigonal warping of the low-energy band structure are set by the ratio γ_3/γ_1, so once γ_1 is accurately known, the analysis of the constant

energy maps near the charge neutrality point reveals the sign and magnitude of γ_3. The band gaps can also be characterized, and the relative contributions from the intralayer asymmetry Δ and the interlayer bias U can be distinguished.

The Hamiltonian in Equation (37) is valid for the π bands across the whole Brillouin zone. However, the low-energy properties of bilayer graphene are determined by the electrons near the Fermi surface, which (for moderate doping or gating) is located near the six K points. We therefore expand the momentum dependence of $\mathcal{H}_\pi$ near the two inequivalent points, and assign the valley index ξ (such that $\xi = +1$ in the K valley, and $\xi = -1$ in the K′ valley) to be a new quantum number for the system. This causes the basis to expand to contain eight elements, not counting the spin degree of freedom. It is convenient to swap the order of the components in the K′ valley, so that the basis is

$$\{\psi_{A_l}, \psi_{B_u}, \psi_{A_u}, \psi_{B_l}\} \text{ in the K valley, and}$$
$$\{\psi_{B_u}, \psi_{A_l}, \psi_{B_l}, \psi_{A_u}\} \text{ in the K}' \text{ valley.}$$

Using this basis, we can write the low-energy Hamiltonian in valley ξ by expanding the functions of momentum to the leading order about the K points as

$$\mathcal{H}_\xi = \begin{pmatrix} \frac{3}{4}t'a^2|\vec{k}|^2 & \xi v_3\pi & \xi v_4\pi^\dagger & \xi v\pi^\dagger \\ \xi v_3\pi^\dagger & \frac{3}{4}t'a^2|\vec{k}|^2 & \xi v\pi & \xi v_4\pi \\ \xi v_4\pi & \xi v\pi^\dagger & \Delta + \frac{3}{4}t'a^2|\vec{k}|^2 & \gamma_1 \\ \xi v\pi & \xi v_4\pi^\dagger & \gamma_1 & \Delta + \frac{3}{4}t'a^2|\vec{k}|^2 \end{pmatrix}, \tag{38}$$

where $v = \sqrt{3}at/(2\hbar)$ is the Fermi velocity of monolayer graphene, $v_3 = \sqrt{3}a\gamma_3/(2\hbar)$ and $v_4 = \sqrt{3}a\gamma_4/(2\hbar)$ are the velocities associated with the interlayer hops, $\pi = p_x + \mathrm{i}p_y$, and $\vec{p} = \hbar\vec{k} = -\mathrm{i}\hbar\vec{\nabla}$.

In the simplest case (the nearest neighbor approximation), with $\gamma_3 = \gamma_4 = \Delta = t' = 0$, we see that the spectrum near the K point is quadratic:

$$E_{\mathrm{nn}} = \chi\sqrt{v^2p^2 + \gamma_1^2/2 + \alpha\gamma_1\sqrt{v^2p^2 + \gamma_1^2/4}}, \tag{39}$$

where $\chi = \pm 1$ refers to the conduction and valence band, and $\alpha = \pm 1$ to the low-energy and split branches illustrated in Figure 28(b). A cross-over to a linear spectrum occurs at $p \approx \gamma_1/2v$, corresponding to the electron density $n^{\mathrm{lin}} \approx \gamma_1^2/(4\pi\hbar^2v^2) \approx 4 \times 10^{12}\,\mathrm{cm}^{-2}$ [139], which is lower than the density at which the higher energy band becomes occupied: $n^{(2)} \approx 2\gamma_1^2/(\pi\hbar^2v^2) \approx 8n^{\mathrm{lin}}$ [139]. The equivalent energy is approximately $\gamma_1/5$.

The qualitative features of this model have been confirmed in optical experiments by Wang *et al*. [148] and Kuzmenko *et al*. [147,164]. Wang *et al*. spectulated that disagreements between the predicted and observed reflectivity properties could be due to excitonic effects altering the optical spectrum. Kuzmenko *et al*. [147] observed peaks in the reflectivity associated with the onset of various inter-band transitions, and were able to extract parameters for the tight-binding model from them. However there were some features which required additional couplings to be considered in the tight-binding model before they could be explained, and we shall discuss them later.

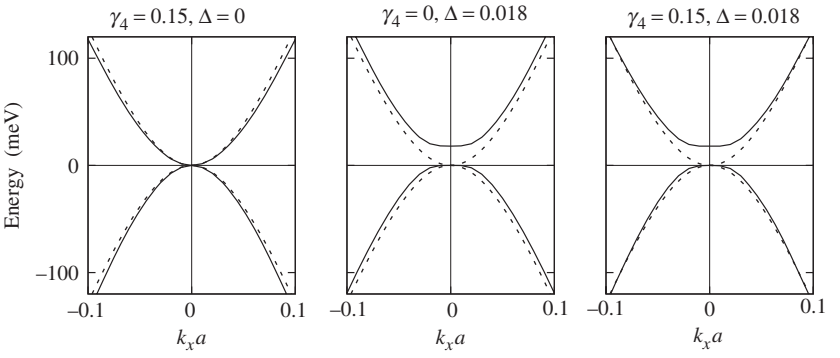

Figure 29. Detail of the effect of γ_4 and Δ (the intralayer site asymmetry induced by the presence of the dimer bond) on the low-energy spectrum near the K point. In each case the solid line represents the labelled tight-binding parameters with $\gamma_3 = t' = 0$, and the dashed lines correspond to $\gamma_3 = \gamma_4 = \Delta = t' = 0$. The k_x momentum is measured from the K point, and $k_y = 0$ throughout.

The effects of the interlayer hop parametrized by γ_4, and the onsite assymmetry Δ is shown in Figure 29, where we plot numerical solutions of the Hamiltonian in Equation (38) with $\gamma_3 = t' = 0$, and various values of γ_4 and Δ. We see that γ_4 introduces a small electron–hole asymmetry, and that Δ increases the conduction band energy near the K point. The combined effect is shown in the third panel of Figure 29. At larger momentum ($k_x a \sim 0.1$), the combined effects of γ_4 and Δ cancel, leaving the bands almost unchanged.

Note that in this section, the overlap matrix has been neglected (see, e.g. Mucha-Kruczyński *et al.* [170], or the book by Saito *et al.* [13]). This has an effect on the band structure, including introducing an asymmetry between the electron and hole bands, although only minimal effect is observed on the low-energy part near the K points.

An analysis of the real space Green's function of bilayer graphene near the K points has been carried out by Wang *et al.* [171]. They derive analytical expressions for the Green's function, and plot the local density of states (LDOS) to compare with experimental scanning tunnelling microscopy images of bilayer flakes. They predict that the lattice sites not involved in the dimer bonds have the highest electron density for electrons with energy below the interlayer coupling γ_1. This is in contrast to monolayer flakes where the two lattice sites are equivalent and the LDOS are identical to each other. The difference in the LDOS, $\Delta\rho_0(\varepsilon)$ is given by

$$\Delta\rho_0(\varepsilon) = \begin{cases} 0 & |\varepsilon| > \gamma_1 , \\ \dfrac{S\gamma_1}{2\pi t^2} & |\varepsilon| < \gamma_1 , \end{cases}$$

where $S = 3\sqrt{3}a^2/2$ is the area of the unit cell in real space.

Lopes dos Santos *et al.* [162] used the continuum limit of the tight-binding formulation to consider the effect on the spectrum of a small rotation (parametrized by the angle θ) between the two graphene layers. The main consequence of the

rotation is that the Dirac cones in each layer are shifted in momentum space, so that the doublet of zero energy states in the lower layer cannot couple via the interlayer dimers to the zero energy states in the upper layer. Instead, they couple to three sets of finite energy states, at $\pm v\Delta K$, where $\Delta K = 2\sin(\theta/2)$. The effect of this altered coupling is that the Dirac cones are preserved, although their energy is shifted downward by an amount $6\tilde{t}_\perp^2 \sin(\theta/2)/(v\Delta K)$. The Fermi velocity is also renormalized so that $\tilde{v}/v = 1 - 9\left[\tilde{t}_\perp/(v\Delta K)\right]^2$, where $\tilde{v}$ is the modified interlayer hopping parameter at the reciprocal lattice vectors, and this reduced velocity constitutes an experimental tool for identifying twisted bilayers. The twist also generates an electric potential difference between the layers, but the absence of coupling between the zero energy states in each layer prevents the opening of a gap at the Dirac point. Finally, an electron–hole asymmetry develops, which shifts the Fermi energy away from the Dirac point at half-filling.

Katsnelson *et al.* [172] showed that, as in the monolayer, the ripples[5] which are intrisic to graphene [24,173] cause the Hamiltonian to be modified by an effective gauge field. This induces zero energy states, which the authors prove (via the Atiyah-Singer theorem) to be topologically protected. The number of these states is determined by the total 'flux' in the sample.

3.2.2. *Trigonal warping*

The next-nearest neighbor couplings may have important effects in the low-energy limit. Chiefly, the direct coupling between atomic sites not involved in the dimer bond (the A_l and B_u sites), which is parametrized by the hopping integral γ_3 causes the low-energy spectrum to become anisotropic. This effect is called trigonal warping, is detectable in ARPES measurements [174,175], and has a significant effect on the weak localization properties of bilayer graphene [176,177]. It is included in the tight-binding formalism with the transfer integral γ_3 which leads to the velocity $v_3 = \sqrt{3}a\gamma_3/(2\hbar)$. The spectrum associated with the nearest neighbor Hamiltonian with the trigonal warping terms was given by McCann [139] as

$$\epsilon_\pm^{(\alpha)} = \pm\sqrt{\frac{1}{2}\gamma_1^2 + \left(v^2 + \frac{1}{2}v_3^2\right)p^2 + (-1)^\alpha\sqrt{\Gamma}}, \tag{40a}$$

where $\alpha = 1, 2$ represents the lower and higher energy bands respectively, and

$$\Gamma = \frac{1}{4}\left(\gamma_1^2 - v_3^2p^2\right)^2 + v^2p^2\left(\gamma_1^2 + v_3^2p^2\right) + 2\xi\gamma_1 v_3 v^2 p^3\cos(3\phi). \tag{40b}$$

In Figure 30(a) we show this spectrum for the parameters given by Zhang *et al.*, but with $\gamma_4 = \Delta = t' = 0$, so that we reveal the effects of the trigonal warping only. Plotting the energy along the line $k_y = 0$, the spectrum is asymmetrical about $k_x = 0$, although electron–hole symmetry is still present since the sublattice symmetry is not broken. For small energies, a Lifshitz transition occurs whereby the Fermi surface breaks into one central region with area $A_c \approx \pi\epsilon^2/(\hbar v_3)^2$ and three elliptical 'leg' regions with area $A_l \approx A_c/3$. The center of the leg regions are at momenta with magnitude $\gamma_1 v_3/v^2$ and angles 0, $2\pi/3$, and $4\pi/3$. The electron density at which this transition in the shape of the Fermi surface will occur is $n_L \approx (v_3/v)^2 \; n^{\text{lin}} \approx 1 \times 10^{11}\,\text{cm}^{-2}$,

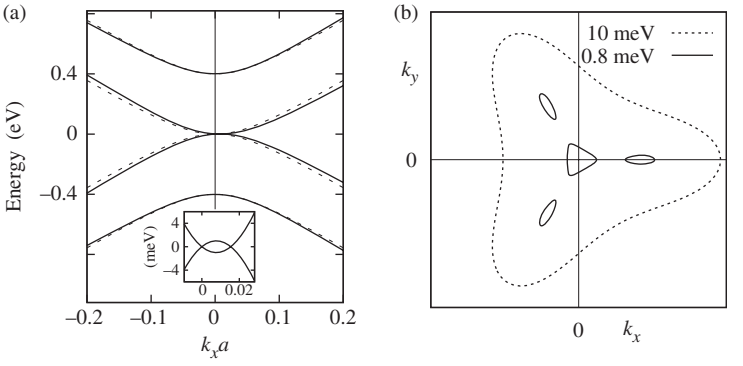

Figure 30. (a) Effect of inclusion of trigonal warping (solid line) in spectrum. The dashed line is for $v_3 = 0$. An asymmetry about $k_x = 0$ is introduced, but electron–hole symmetry persists. The inset shows the very low energy spectrum, and the band overlap of ≈ 2 meV induced by the trigonal warping. (b) Isoenergetic lines in momentum space for $v_3/v = 0.1$. For $E \approx 1$ meV the Fermi surface splits into four pockets.

where n^{lin} is the density corresponding to the cross-over from the quadratic to the linear spectrum, discussed after Equation (39). The trigonal warping has a substantial effect on the low-energy transport properties of the bilayer.

3.2.3. *Effective low-energy theory*

In 2006, McCann and Falko [139] introduced a low-energy effective model for bilayer graphene. In essence, it is an expansion of the Hamiltonian in the parameter ε/γ_1 which effectively excludes the atomic sites involved in the dimer bond. Starting from the Hamiltonian in Equation (38), with $\gamma_4 = t' = \Delta = 0$, and including the interlayer bias U discussed in Section 3.3, four blocks can be identified:

$$\mathcal{H}_{11} = \xi\Big(U\sigma_z/2 + v_3[\sigma_x p_x - \sigma_y p_y]\Big), \quad \mathcal{H}_{22} = -\xi U\sigma_z/2 + \gamma_1\sigma_x,$$
$$\mathcal{H}_{21} = \mathcal{H}_{12} = \xi v(\sigma_x p_x + \sigma_y p_y).$$

The 4×4 Green's function associated with $\mathcal{H}_\xi$ can also be split into 2×2 blocks, and the approach taken by McCann was to compute the block G_{11} involving only the lower band states, and use it to identify the effective low-energy Hamiltonian. In particular, using $G^{(0)}_{aa} = (\mathcal{H}_{aa} - \epsilon)^{-1}$,

$$G = \big(\mathcal{H}_\xi - \epsilon\big)^{-1} = \begin{pmatrix} G^{(0)-1}_{11} & \mathcal{H}_{12} \\ \mathcal{H}_{21} & G^{(0)-1}_{22} \end{pmatrix}^{-1}.$$

Simple evaluation of the equation $GG^{-1} = 1$ gave

$$G_{11}^{-1} + \epsilon = \mathcal{H}_{11} - \mathcal{H}_{12}G^{(0)}_{22}\mathcal{H}_{21}.$$

Now, the low-energy effective Hamiltonian $\mathcal{H}_2$ is identified with the Green's function G_{11} as $\mathcal{H}_2 = G_{11}^{-1} + \epsilon$ so that the Schrödinger equation for this Hamiltonian was written as

$$\mathcal{H}_2\psi = \epsilon\psi \Rightarrow \left[\mathcal{H}_{11} - \mathcal{H}_{12}G_{22}^{(0)}\mathcal{H}_{21}\right]\psi = \epsilon\psi.$$

Making a Taylor expansion of $G_{11}^{(0)}$ in the small parameters ϵ/γ_1 and U/γ_1, substituting in the Schrödinger equation for the 2×2 Hamiltonian, moving all terms containing energy to the right-hand side, and rearranging for $\mathcal{H}_2$ gives

$$\mathcal{H}_2 = -\frac{v^2}{\gamma_1}\begin{pmatrix} 0 & \pi^{\dagger 2} \\ \pi^2 & 0 \end{pmatrix} + \xi v_3 \begin{pmatrix} 0 & \pi \\ \pi^\dagger & 0 \end{pmatrix} + \frac{\xi U}{2}\left[\begin{pmatrix} 1 & 0 \\ 0 & -1 \end{pmatrix} - \frac{2v^2}{\gamma_1^2}\begin{pmatrix} \pi^\dagger\pi & 0 \\ 0 & -\pi\pi^\dagger \end{pmatrix}\right]. \tag{41}$$

This expression is interesting in a number of ways. Firstly, the kinetic energy now comes with factors of π^2, which ensures that the energy dispersion is quadratic in this limit. This corresponds to the electrons gaining a finite effective mass at the bottom (top) of the conduction (valence) band, and the Dirac spectrum disappears. However, the chirality of the electrons persists because the sublattice pseudospin is still a relevant degree of freedom. The linear momentum term now carries the velocity $v_3 \sim v/10$. Therefore, this term is important at low momentum and its effect on the band structure (called trigonal warping) is discussed in Section 3.2.2. The final term in this expression contains contributions to the Hamiltonian from the interlayer asymmetry potential. Since the decoupled lattice sites retained in this model are in opposite layers, the low-energy band structure keeps its dependence on U via the first term in the bracket as it was in the four band case. Further discussion of this term is deferred until Section 3.3. The second term in the bracket is sometimes called the kinetic asymmetry, and is due to the depletion of charge on the A_u, B_l dimer sites. Using a more compact notation, this equation can also be written as the final result of McCann and Falko [139]:

$$\mathcal{H}_2 = -\frac{1}{2m}(\vec{\sigma}\cdot\vec{p})\sigma_x(\vec{\sigma}\cdot\vec{p}) + \xi v_3\vec{\sigma}^t\cdot\vec{p} + \frac{\xi U}{2}\sigma_z + \frac{\xi U}{2m\gamma_1}(\vec{\sigma}\cdot\vec{p})\sigma_z(\vec{\sigma}\cdot\vec{p}), \tag{42}$$

where $m = \gamma_1/(2v^2)$ is the effective mass induced by the curvature of the bands, and the superscript t denotes the transpose of the matrix.

3.3. *Band gap in bilayer graphene*

3.3.1. *Band gap in the tight-binding model*

The symmetry governing the degeneracy of the highest valence and lowest conduction bands at the K points in neutral bilayer graphene is the inversion symmetry. If this symmetry is broken, then a gap is expected to appear in the low-energy spectrum [139,178,179]. This breaking of symmetry can be modelled within the tight-binding approximation by assuming that the two layers are at different electrostatic potentials (Figure 31(a)) so that the difference between them is parametrized by the energy U. The Hamiltonian corresponding to the full bilayer

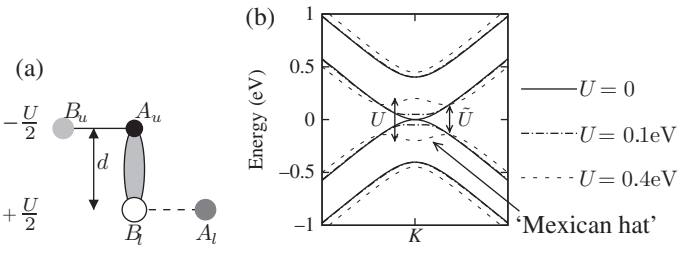

Figure 31. (a) Side-on view of the bilayer lattice, with the interlayer potential U and the interlayer separation d labelled. (b) Low-energy tight-binding bands for three values of the gap U, with $\gamma_3 = \gamma_4 = \Delta = t' = 0$, $t = 3$ eV and $\gamma_1 = 0.4$ eV. The gap at the K point is U, whereas the minimum splitting between the bands occurs at $\tilde{U}$.

system with broken inversion symmetry is given by $\mathcal{H} = \mathcal{H}_0 + \mathcal{H}_U$, where $\mathcal{H}_0$ is discussed fully in Section 3.2, and

$$\mathcal{H}_U = \begin{pmatrix} \xi U/2 & 0 & 0 & 0 \\ 0 & -\xi U/2 & 0 & 0 \\ 0 & 0 & -\xi U/2 & 0 \\ 0 & 0 & 0 & \xi U/2 \end{pmatrix} = \frac{\xi U}{2} \sigma_z \otimes \sigma_z, \tag{43}$$

which corresponds to the lower layer being at potential $+U/2$, and the upper layer at $-U/2$. The factor of ξ is necessitated by the definition of the bases in the two valleys. The effect of the inclusion of this term is illustrated in Figure 31(b) for the nearest neighbor tight-binding model. We see that for moderate values of the interlayer potential (often called the bias potential), a gap does indeed appear at the K point, but the quadratic profile of the low-energy dispersion is retained. For higher values of the bias, the quadratic nature is replaced with the 'Mexican hat' dispersion [180]. The band structure associated with this simplified Hamiltonian is

$$\epsilon^2 = v^2 p^2 + \gamma_1^2/2 + U^2/4 + \alpha \sqrt{v^2 p^2 (U^2 + \gamma_1^2) + \gamma_1^4/4},$$

where $\alpha = 1$ designates the split bands, and $\alpha = -1$ gives the low-energy bands. From this expression, it is straightforward to compute that the gap exactly at the K point is U, and that the minimum separation of the conduction band and valence band is

$$\tilde{U} = \frac{\gamma_1 U}{\sqrt{U^2 + \gamma_1^2}} \quad \text{at momentum} \quad p^2 = \frac{U^2}{4v^2} \frac{U^2 + 2\gamma_1^2}{U^2 + \gamma_1^2}.$$

The two quantities are labelled in Figure 31(b). Therefore, $U \approx \tilde{U}$ for bias up to $U = 0.2$ eV.

In the preceding analysis, the size of that gap was treated as a phenomenological parameter. In a typical experimental setup, the source of the symmetry breaking is either a gating arrangement, or a number of dopants placed on one face of the graphene bilayer. Two studies [178,181] have related the characteristics of the gate or the dopant concentration to the size of the gap in the context of the continuum limit of the tight-binding model. We shall discuss first-principles calculations of these effects in Section 3.3.3. The excess charge density $n = n_1 + n_2$ is distributed between

both layers because of the incomplete screening, so that there is a potential energy difference [178]

$$U = U_0 + e^2 n_2 L^2 / C_b \tag{44}$$

between the two layers. In this expression, U_0 is the bare asymmetry parameter which gives a finite asymmetry at zero density (due to, e.g. uncontrolled doping in the fabrication process, or interactions between the graphene flake and the substrate), L^2 is the flake area and $C_b = \varepsilon_r \varepsilon_0 L^2/d$ is the capacitance of the bilayer with dielectric constant ε_r. The gap is calculated self-consistently, and Figure 32(a) shows the calculated value of the gap for three values of the bare asymmetry. Figure 32(b) shows the densities on the two individual layers for a finite bare asymmetry $U_0 = \gamma_1/5 = 78$ meV. The result of the screening is to reduce the zero density gap so that $U(0) < U_0$. In the limiting case $\gamma_1, \epsilon_F \gg |U|$, an analytic expression for $U(n)$ can be derived. Integrating the wave function amplitudes to find the layer density of the partially occupied bands, the densities are

$$n_{1(2)} \approx \frac{\mathrm{sgn}(\epsilon_F)\, p_F^2}{2\pi\hbar^2} \pm \frac{\gamma_1 U}{2\pi\hbar^2 v^2}\left[\frac{\epsilon_0}{\gamma_1} + \frac{\epsilon_0^2}{\gamma_1^2} - \frac{1}{2}\ln\left(\frac{\epsilon_0}{\gamma_1}\right)\right],$$

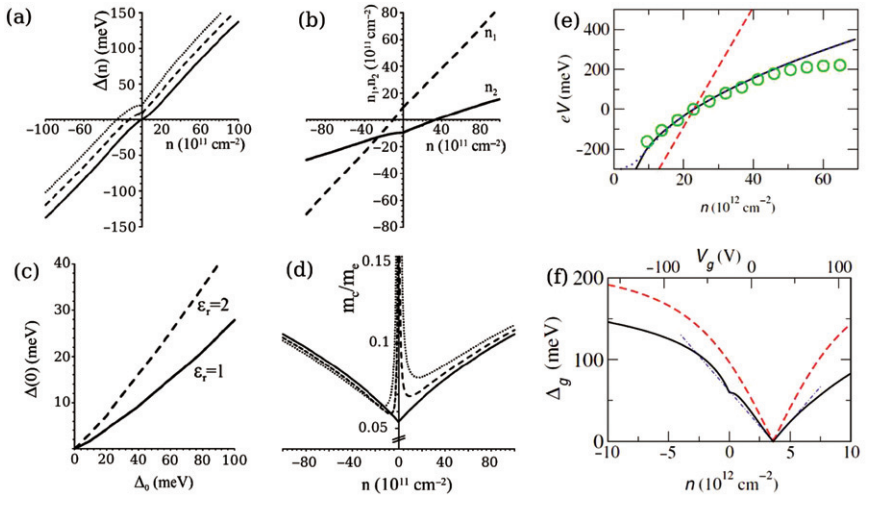

Figure 32. (a) Numerical evaluation of the bilayer asymmetry $U(n)$ for different values of the bare asymmetry: $U_0 = 0$ (solid line), $U_0 = \gamma_1/10 = 39$ meV (dashed line) and $U_0 = \gamma_1/5 = 78$ meV (dotted line), using typical parameter values $\gamma_1 = 0.39$ eV, $d = 3.55$ Å, $\varepsilon_r = 1$ and $v = 8.0 \times 10^5$ m s^{-1}. (b) Layer densities n_2 (solid) and n_1 (dashed) as functions of n for $U_0 = \gamma_1/5 = 78$ meV. (c) $U(0)$ as a function of U_0 for $\varepsilon_r = 1$ (solid line) and $\varepsilon_r = 2$ (dashed). (d) The cyclotron mass in units of the bare electronic mass for different values of U_0 as in (a). (e) $U(n)$, where the solid and dotted lines are the result of the self-consistent procedure for $\gamma_1 = 0.2$ eV and $\gamma_1 = 0.4$ eV, respectively; the dashed line is the unscreened result; the circles represent $U(n)$ measured by ARPES [140]. (f) Band gap $\tilde{U}$ as a function of density (bottom axis) and gate voltage (top axis): solid and dashed lines are for the screened and unscreened cases, respectively. The thin dashed-dotted line is a linear fit to the screened result at small biases. ((a)–(d) Reprinted with permission from E. McCann, Physical Review B, 74, 161403, 2006 [178]. Copyright © (2006) by the American Physical Society); ((e) and (f) Reprinted with permission from E.V. Castro *et al.*, Physical Review Letters, 99, 216802, 2007 [181]. Copyright © (2007) by the American Physical Society.)

where the 'ungapped' energy is $\epsilon_0 = (\gamma_1/2)\left[\sqrt{1+4v^2p_F^2/\gamma_1^2}-1\right]$. In the limit discussed, $v^2p_F^2 \approx \epsilon_F^2 + \gamma_1|\epsilon_F|$ so that ϵ_0 is independent of U and Equation (44) is used to find

$$U \approx \frac{U_0 + e^2L^2n/(2C_b)}{1+\Lambda\left[\frac{\epsilon_0}{\gamma_1}+\frac{\epsilon_0^2}{\gamma_1^2}-\frac{1}{2}\ln\left(\frac{\epsilon_0}{\gamma_1}\right)\right]}.$$

This approximation is valid for intermediate densities $U, \tilde{U} \ll |\epsilon_F| < \gamma_1$ where $\epsilon_F \approx \epsilon_0$. The effectiveness of the screening is given by the parameter $\Lambda = e^2L^2\gamma_1/(2\pi\hbar^2v^2C_b)$, which depends on the model parameters, as illustrated in Figure 32(c). Here $U(0)$ is shown as a function of U_0 for $\varepsilon_r = 1$ (solid line) and $\varepsilon_r = 2$ (dashed line). It is clear that the gap increases with the dielectric constant.

According to Castro *et al.* [181], the screened potential difference between the two layers is given by

$$U = \left(2 - \frac{n}{n_0} + \frac{\Delta n(n,V)}{n_0}\right)\frac{n_0ed}{2\epsilon_0},$$

where $\Delta n(n,V)$ is the induced charge imbalance between the two layers, which is calculated through the weight of the wave functions in each layer. This charge imbalance produces an internal electric field which screens the external one. Figure 32(e) shows the comparison of the screened and unscreened calculations with experimental data taken in ARPES measurements by Ohta *et al.* [140]. The unscreened model cannot accurately describe the experimental data, whereas the results of the self-consistent procedure do. The theoretical dependence of the gap on the electron density is shown in Figure 32(f), along with a linear fit (valid in the small gap regime only). The theory predicts saturation of the gap $U \approx \gamma_1$ at large biases.

Pereira *et al.* [182] performed an analytical study of the effect of a band gap and changing electron density on the length of the interlayer dimer bonds. In their model, the atoms not involved in the bonding are assumed to be static, and a uniform displacement of the A_u and B_l atoms towards each other is considered assuming that the Fermi energy is in the conduction band. The Mexican hat shape of the band structure plays a role by changing the topology of the Fermi surface, and introducing non-monotonicity into the displacement. Two densities,

$$n^* = \frac{g\mathcal{A}_cV^2}{4\pi v^2} \quad \text{and} \quad n^{**} = \frac{g\mathcal{A}_c(V^2+2\gamma_1^2)}{4\pi v^2}$$

characterize the behavior, where $\mathcal{A}_c$ is the area of the unit cell. The quantity n^* designates the density which corresponds to the Fermi level being at the top of the Mexican hat, and sets the scale for the minimum of the lattice displacement. As the density is increased further, the displacement saturates with the onset of saturation being marked by n^{**}. Since there are a number of poorly-known parameters in the model, the quantitative results are unreliable.

3.3.2. *Experimental evidence of gap*

Experimental verification of the predicted band structure of gapped bilayer graphene has been obtained in two ways. Firstly, it has been shown by Ohta *et al.* [140] that

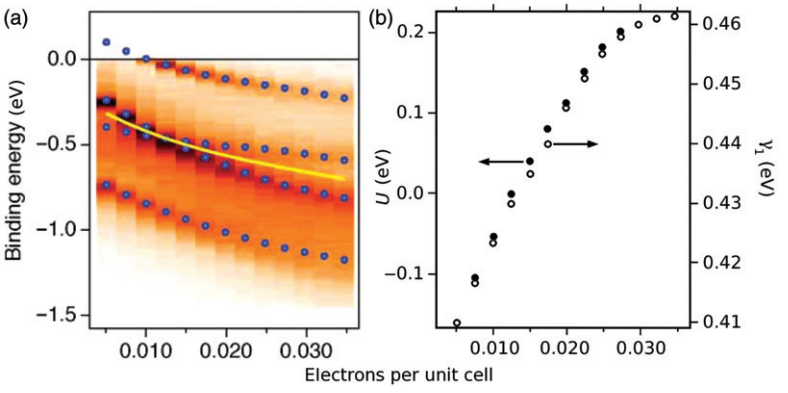

Figure 33. (Colour online) Variation of states at the K point with increasing potassium coverage. (a) The image map shows the energy distribution curve at K as a function of potassium coverage. The blue markers are the fitted positions of the tight-binding π and π^* bands, and the yellow line indicates E_D. The closing and reopening of the gap between π and π^* states are clearly shown. (b) The influence of doping concentration on the band parameters U (filled dots) and γ_1 (open circles) (Reprinted figure with permission from T. Ohta *et al.*, Science, 313, p. 951, 2006 [140]. Copyright © (2006) The American Association for the Advancement of Science.).

n-type doping of a bilayer graphene flake by potassium atoms causes an increase in the total charge density on the upper layer which generates a static electric field which was characterized by U. Since the screening length ($\sim$4 Å) is comparable to the interlayer separation ($d \approx 3.4$ Å), the screening of this charge is incomplete and a net dipole field results between the two layers. Ohta and Bostwick [140,179] used ARPES to determine the low-energy band structure of the bilayer and hence determined the gap and other band structure parameters. Figure 33(a) shows the evolution of the four π bands as the concentration of potassium dopants increases. At minimal doping, the remnant charge asymmetry from the manufacturing process and substrate interactions causes the bilayer to be slightly positively doped and a small gap is seen between the middle two bands. For the doping of approximately 0.012 electrons per unit cell, the bilayer is overall charge-neutral and the gap closes. Increasing the doping further provides overall negative charge density and the gap reopens. Figure 33(b) shows the evolution of the interlayer potential difference U as a function of the dopant concentration (filled dots). For moderate dopant density, the change in the potential is linear and moves through zero at approximately 0.012 electrons per unit cell, precisely coinciding with the closing of the gap. Castro *et al.* [181] also demonstrated the existence of a gap by chemically doping a bilayer in the case of a finite magnetic field.

The second method of producing a gap in the low-energy spectrum is to use electronic gating. Infra-red spectroscopy [183,184] has shown band gaps of up to 250 meV (Figure 35) which have a slight nonlinear dependence on both photon energy and electronic density. An example device is shown in Figure 34(a), where a top gate is fabricated over an AB-stacked graphene bilayer (Figure 34b). The presence of this gate and the back gate allow two electrical displacement fields D_b of the back gate and D_t of the top gate (Figure 34c) to be

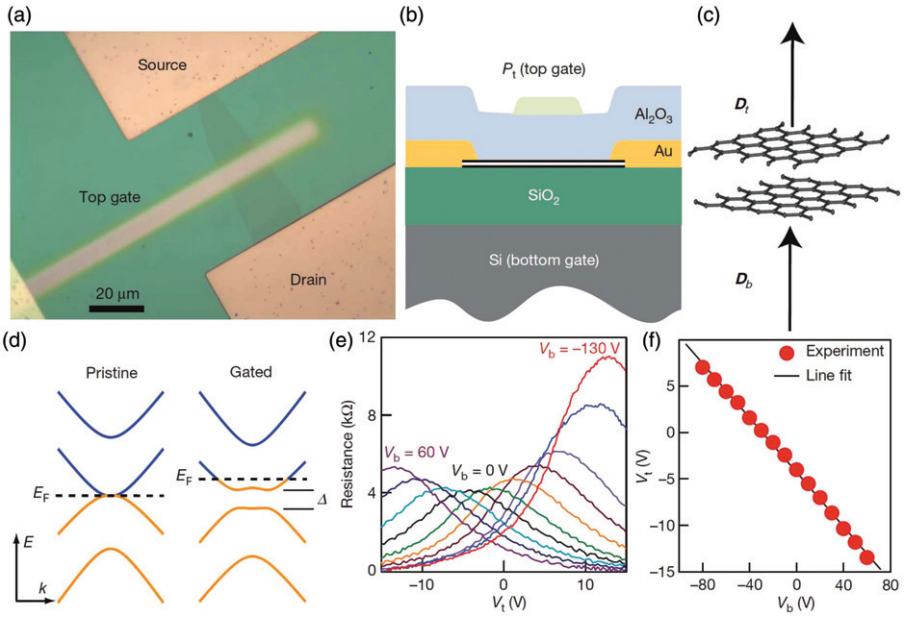

Figure 34. Dual-gated bilayer graphene. (a) Optical microscopy image of the bilayer device (top view). (b) Illustration of a cross-sectional side view of the gated device. (c) Sketch showing how gating of the bilayer induces top (D_t) and bottom (D_b) electrical displacement fields. (d) Left, the electronic structure of a pristine bilayer has zero band gap (where k denotes the wave vector.) Right, upon gating, the displacement fields induce a non-zero band gap U and a shift of the Fermi energy E_F. (e) Graphene electrical resistance as a function of top gate voltage V_t at different fixed bottom gate voltages V_b. The traces are taken with 20 V steps in V_b from 60 V to −100 V and at $V_b = -130$ V. The resistance peak in each curve corresponds to the charge-neutrality point (CNP) where $D_b = D_t$ for a given V_b. (f) The linear relation between top and bottom gate voltages that results in bilayer CNPs (Reprinted figure with permission from Y. Zhang *et al.*, Nature, 459, p. 820, 2009 [184]. Copyright © (2009) Nature Publishing Group.).

independently controlled. The average of these fields breaks the inversion symmetry of the graphene flake and opens the gap at the charge neutrality point. The difference of these fields leads to a net carrier doping, so that the position of the Fermi level and the size of the band gap may be controlled independently (Figure 34d). If the back gate voltage is fixed and the top gate voltage swept, traces such as those in Figure 34(e) are found, showing that the charge-neutrality point (corresponding to the peak in the resistance) shifts, and the magnitude of the peak resistance increases with both increasing positive and negative back gate voltage. This increase in the peak resistance may be linked to an increasing magnitude of the band gap.

The infra-red spectroscopy measurements show that the absorption peak near $\gamma_1 \approx 0.4$ eV associated with the inter-band optical transitions splits into two when the top gate is applied. One peak moves downwards in energy with increasing gate voltage, the other upwards, as in the left-most panel of Figure 35. This behavior is explained by noting that peak 1 is due to transitions between the lower and upper conduction bands, while peak 2 is due to transitions from the upper valence band to the upper conduction band. Therefore, if a gap is present between the upper valence

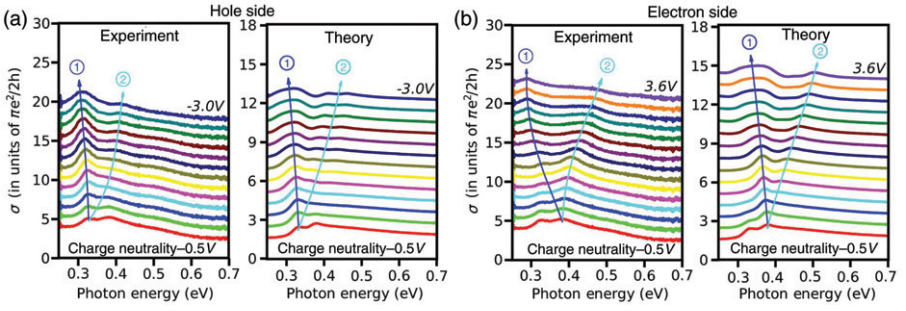

Figure 35. Experimental and theoretical spectra of the IR conductivity in units of $\pi e^2/2h$ for (a) the hole side and (b) the electron side as a function of photon energy. Charge neutrality occurs at $V = -0.5$ V. In the case of hole doping, the traces correspond to $V = -0.5$, -0.8, -1.0, -1.2, -1.4, -1.6, -1.8, -2.0, -2.2, -2.4, -2.6, -2.8 and -3.0 V from bottom to top. In the electron side, the traces are for $V = -0.5$, -0.4, -0.3, -0.2, 0.0, 0.2, 0.4, 0.8, 1.2, 1.6, 2.0, 2.4, 2.8, 3.2 and 3.6 V. The theoretical data is obtained via the Kubo formula (Reprinted figure with permission from K.A. Mak *et al.*, Physical Review Letters, 102, 256405, 2009 [183]. Copyright © (2009) by the American Physical Society.).

and lower conduction bands, and the Fermi energy is located in the conduction band, the energy of the transition associated with peak 1 will decrease, whereas that associated with peak 2 will increase. The energy gap between the two peaks is then precisely the band gap. The left-hand plots in both Figure 35(a) and (b) are experimental data showing exactly this trend. A maximum gap of ~200 meV is seen for a gate voltage of 3.6 V. The peaks also broaden because the bands are not exactly parallel, so a wider range of transition energies are allowed for stronger gating.

As has already been stated, one of the attractive prospects for the utilization of graphene in technological applications is in ballistic field-effect transistors. The external tunability of the band gap in the biased bilayer is particularly exciting in this context, and attempts have been made to implement current-switching devices using this idea [185]. Transport measurements showed a gate-induced insulating state and significantly non-Ohmic current–voltage characteristics at low temperatures, but the band gap revealed by these transport measurements was significantly lower than predicted by theory, and current switching was unobtainable at high temperature. While these experiments may demonstrate the proof of principle for these devices, there are still many challenges to be overcome. In addition, the careful analysis of the low-temperature data revealed that the transport is best described by disorder induced by variable range hopping in an insulating material where impurity states localized in the band gap are the predominant mechanism for transport. Thermally activated transport did not qualitatively explain the experimental results.

3.3.3. Ab-initio *simulations*

Various studies have been carried out on the effect of the interlayer electric field using first principles techniques [168,169,186–188]. There is some confusion in the literature because for the two main approximations for the exchange and correlation potentials, the local density approximation (LDA) and generalized gradient

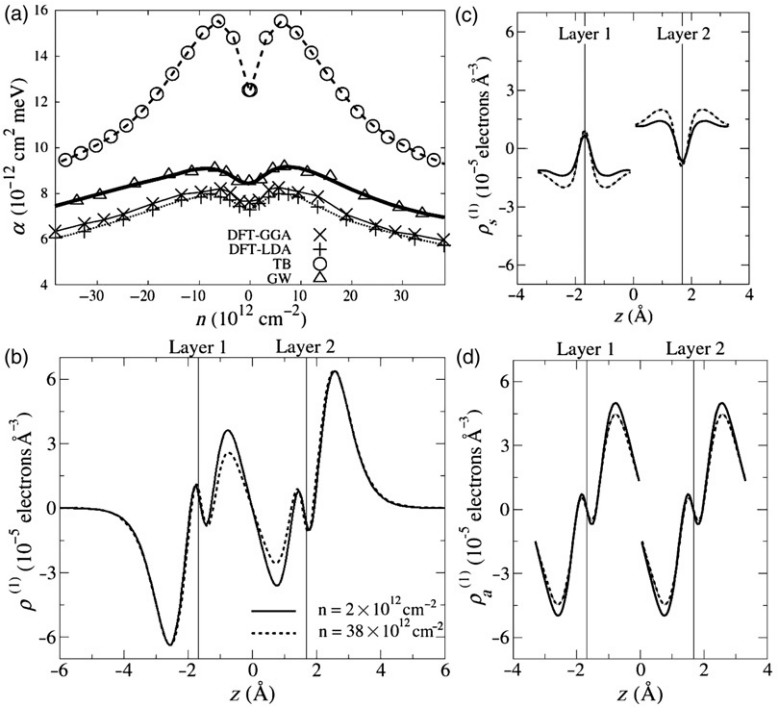

Figure 36. (a) α (as defined in Equation (45)) as a function of doping n, for an electronic temperature of 300 K calculated with DFT-GGA (crosses), and DFT-LDA (pluses), calculated using the TB model with $\gamma_0 = 3.1\,\text{eV}$ and $\gamma_1 = 0.4\,\text{eV}$ (circles) and using the GW correction (up-triangles). The continuous thick line is the fit of the GW result. (b) Planar average of the linearly induced charge (per unit volume) $\rho^{(1)}$ for bilayer graphene in the presence of an external electric field $E_{\text{av}} = 1.6 \times e/(2\varepsilon_0)10^{12}\,\text{cm}^{-2}$ for doping level $n = 2 \times 10^{12}\,\text{cm}^{-2}$ (continuous line) and $n = 38 \times 10^{12}\,\text{cm}^{-2}$ (dashed line). (c) The symmetric component, $\rho_s^{(1)}$; (d) the antisymmetric component $\rho_a^{(1)}$, with respect to each layer, of the linearly induced charge $\rho^{(1)}$ shown in (b) for the same doping levels (Reprinted figure with permission from P. Gava *et al.*, Physical Review B, 79, 165431, 2009 [169]. Copyright © (2009) by the American Physical Society.).

approximation (GGA) have been shown to give quantitatively different results for the optimum interlayer spacing d and the band gap U.

The most thorough study was published by Gava *et al.* [169] in which they describe the size of the gap as a function of the doping and the external electric field. They demonstrate first that the size of the gap is linearly dependent on the charge imbalance between the two layers, and define the linear coefficient as

$$U(n, E_{\text{av}}) = \alpha(n)(n_1 - n_2), \tag{45}$$

where $n_{1,2}$ are the densities on the two layers, and E_{av} is the applied electric field. In the absence of electronic screening, α is independent of the doping, and $\alpha^{\text{bare}} = \frac{de^2}{2\epsilon_0} = 30.3 \times 10^{-12}\,\text{cm}^2\,\text{meV}$. The DFT results within the LDA, GGA and GW approximations are compared to tight-binding results employing a simple electrostatic model to account for the screening in Figure 36(a). It is clear from the

figure that while all four estimations give the same qualitative dependence, the tight-binding approximation gives a significantly higher slope than any of the first principles results. There are two possible reasons for this discrepancy: The crude electrostatic model used in the self-consistent process in the tight-binding model, and systemic differences in the calculated band structures between the first principles and tight-binding results. The authors demonstrate that both factors play a significant role. The differences in charge transfer which lead to the reduced screening between the two models is illustrated in Figure 36(b–d). The linearly induced charge (per unit volume) is

$$\rho^{(1)}(z; n, E_{\mathrm{av}}) = \frac{\partial \rho(z; n, E_{\mathrm{av}})}{\partial E_{\mathrm{av}}} E_{\mathrm{av}} \approx \frac{1}{2}[\rho(z; n, E_{\mathrm{av}}) - \rho(z; n, -E_{\mathrm{av}})],$$

where $\rho(z; n, E_{\mathrm{av}})$ is the planar average of the charge density (per unit volume) at doping n and in the presence of an external average electric field E_{av}. The charge density $\rho^{(1)}$ is antisymmetric with respect to $z = 0$ (which corresponds to the point half-way between the two graphene planes) and is plotted in Figure 36(b). We see that the electronic screening is characterized by the charge transfer between the two layers, and an intralayer polarization (which is also present in the monolayer). The density is decomposed into a symmetric component $\rho_s^{(1)}$ and an antisymmetric component $\rho_a^{(1)}$ with respect to each individual layer defined by

$$\rho_{s/a}^{(1)}(z) = \frac{1}{2}\left\{\rho^{(1)}(z) \pm \rho^{(1)}[\mathrm{sgn}(z)d - z]\right\}.$$

These are shown in Figure 36(c) and (d), respectively. Clearly, these quantities are related to the inter- and intralayer charge transfer, respectively. The antisymmetric contribution is very similar to the induced charge in a single monolayer, and is of the same order of magnitude as the total induced charge in the bilayer. On this basis, the authors conclude that the intralayer polarization gives an important contribution to the screening properties of the system. This contribution is not taken into account in the tight-binding approximation, and is the major contribution to the discrepancy between these two models. The authors also show that the GW correction adds a contribution to the density dependence of the linear parameter α (Figure 36a) which can be explained within a perturbation theory analysis. Also, the temperature dependence of the linear parameters is small.

Other notable works include the comparison of the AB and AA stacking arrangements by Huang *et al.* [188] and Aoki *et al.* [186], in which they demonstrate that AB stacking is energetically favorable over the AA arrangement. Also, Min *et al.* [168] published the first systematic DFT study of the gapped bilayer, showing that the size of the gap saturates with increasing interlayer potential. They also claim that the exchange potential may contribute to the discrepancies between the DFT and tight-binding results, and that the logarithmic divergence of the screening ratio at small gate voltage (demonstrated within the tight-binding model by McCann [178]) is reproduced in their calculations. Yu *et al.* [189] considered the polarizability of graphene stacks within the LDA approximation, and they also found the same qualitative picture sketched above. Specifically, the gap saturation was at approximately 0.25 eV, although the gap size at fields where electric breakdown will start to

occur in SiO_2 was 0.17 eV. They also investigated the distribution of charge between layers and sublattices, finding that an external field induces a significant electron concentration on one layer, with a positive charge cloud on the other, and that the lattice sites not involved in the dimer (γ_1) bonding have higher density. Finally, atomistic calculations have been presented by Fiori *et al.* [187] to assess the practicality of FET devices implemented in gapped bilayer graphene. They claim that there is no conceptual issue, but that the band gap is not wide enough to support a sufficiently high on/off current ratio.

3.4. *Quantum Hall effect*

The quantum Hall effect in bilayer graphene is a fascinating manifestation of the massive chiral nature of the low-energy quasiparticles. When a magnetic field with a large component perpendicular to the graphene plane is applied, the electron spectrum splits into Landau levels (LLs), just as in a traditional two-dimensional electron system, or as in monolayer graphene (Section 2.1). However, the form of the dependence of the energy of these levels on the magnetic field, level index, density and other parameters are qualitatively different from both of these examples. The chiral nature of the electrons is reflected in the presence of zero-energy levels, and the increased Berry's phase manifests in the doubled degeneracy of these levels. The quadratic low-energy dispersion is represented by the linear dependence of the LL spectrum on the magnetic field, and the near-linear dependence on the LL index. We shall begin in this section by presenting the experimental evidence for the novel quantum Hall effect in bilayer graphene. Then, in order to describe the behavior of the low-energy Landau levels, the two band tight-binding model introduced by McCann *et al.* [139] will be used in Section 3.4.2 to demonstrate the main features. The magneto-optical properties are discussed in Section 3.4.3, the trigonal warping is included in Section 3.4.4 and electron–electron interactions and the perculiar properties of the zero modes are reviewed in Section 3.4.5.

3.4.1. *Experimental picture*

The first report of an observation of the quantum Hall effect in bilayer graphene was given by Novoselov *et al.* [141]. Using samples obtained by the microcleavage technique and fashioned into multi-terminal transistor devices, the low-temperature transport properties were measured in strong magnetic fields. Figure 37(a) shows typical traces of the longitudinal and transverse resistivities at fixed electron density as a function of the magnetic field. Plateaus in the Hall resistivity accompanied by dips in the longitudinal resistivity are clearly seen. The sequence of QHE plateaus is described by $\rho_{xy} = h/4ne^2$ (where n is an integer designating the level), as would be expected in a traditional two-dimensional electron system with spin and valley degeneracies. However, a significant discrepancy with this case is manifest at small filling factors, as shown in Figure 37(b): the expected level at zero density is not present, leading to a double-sized step across the zero density point, and indicating a Landau level with doubled degeneracy relative to the higher Landau levels. The absence of a plateau at zero energy resembles the behavior of the massless Dirac fermions observed in the monolayer material (Section 2.2). Figure 37(c–f) shows that

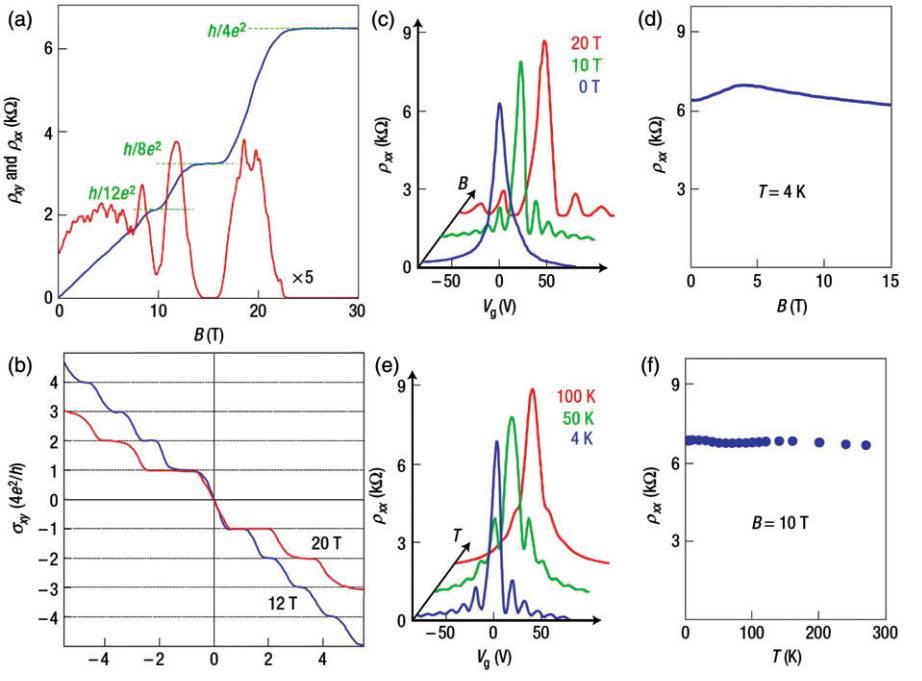

Figure 37. (a) Hall resistivities ρ_{xy} and ρ_{xx} measured as a function of B for fixed concentrations of electrons $n \approx 2.5 \times 10^{12}\,\mathrm{cm}^{-2}$ induced by the electric field effect. The known geometry of the devices allowed the authors to convert the measured resistance into ρ_{xx} with an accuracy of better than 10%. (b) σ_{xy} plotted as a function of n at a fixed B and temperature $T = 4\,\mathrm{K}$. Positive and negative n correspond to field-induced electrons and holes, respectively. σ_{xy} crosses zero without any sign of the zero-level plateau that would be expected for a conventional 2D system. (c–f) Resistivity of bilayer graphene near zero concentration as a function of magnetic field and temperature. The peak in ρ_{xx} remains of the order of $h/4e^2$, independent of B (c,d) and T (e,f). This yields no gap in the Landau spectrum at zero energy (Reprinted figure with permission from K.S. Novoselov *et al.*, Nature Physics, 2, p. 177, 2006 [141]. Copyright © (2006) Nature Publishing Group.).

the height of the ρ_{xx} peak is only weakly dependent on magnetic field and temperature, which again contrasts starkly with the traditional two-dimensional case.

3.4.2. *Tight-binding description of low-energy Landau levels*

The main features of the Landau level spectrum are best exhibited in the low-energy effective model introduced by McCann and Falko [139] and discussed in Section 3.2.3. The leading term in the two-band Hamiltonian for bilayer graphene is

$$\mathcal{H} = -\frac{1}{2m}(\vec{\sigma}\cdot\vec{p})\sigma_x(\vec{\sigma}\cdot\vec{p}),$$

which corresponds to the continuum limit of the nearest neighbor tight-binding theory in the K valley. To account for a magnetic field characterized by the vector potential $\vec{A}$, we employ the generalized momentum operator $\vec{p} - q\vec{A}$, where $q = -e$

such that $e > 0$ is the electron charge. In that case, the matrix form of the Hamiltonian becomes

$$\mathcal{H} = -\frac{1}{2m}\begin{pmatrix} 0 & (p_x + eA_x - \mathrm{i}p_y - \mathrm{i}eA_y)^2 \\ (p_x + eA_x + \mathrm{i}p_y + \mathrm{i}eA_y)^2 & 0 \end{pmatrix}.$$

We shall work within the Landau gauge defined by $\vec{A} = Bx\vec{\ell}_y$ so that the magnetic field $\vec{B} = \vec{\nabla} \times \vec{A} = B\vec{\ell}_z$. In this case, the π and $\pi^\dagger$ operators correspond to lowering and raising operators for the basis of magnetic oscillator functions given by $\varphi_m = \mathrm{e}^{\mathrm{i}k_y y}\,\phi_m(x)$. These functions are defined so that

$$\pi\phi_0 = 0, \quad \pi\phi_m = -\frac{\mathrm{i}\hbar}{l_B}\sqrt{2m}\phi_{m-1}, \quad \pi^\dagger\phi_m = \frac{\mathrm{i}\hbar}{l_B}\sqrt{2(m+1)}\phi_{m+1}, \tag{46}$$

where $l_B = \sqrt{\hbar/(eB)}$ is the magnetic length, and the indices $m \geq 0$ are integers. Using these relations in the Schrödinger equation gives the spectrum of discrete levels $\varepsilon_{\mathrm{n}}^{\pm}$ and associated wave functions $\Phi_{\mathrm{n}}^{\pm}$ as[6]

$$\varepsilon_0 = 0, \quad \Phi_0 = \begin{pmatrix} \phi_0 \\ 0 \end{pmatrix}; \quad \varepsilon_1 = 0, \quad \Phi_1 = \begin{pmatrix} \phi_1 \\ 0 \end{pmatrix};$$

$$\varepsilon^{\pm}_{|\mathrm{n}|\geq 2} = \pm\hbar\omega_c\sqrt{|\mathrm{n}|(|\mathrm{n}|-1)}, \quad \Phi^{\pm}_{|\mathrm{n}|\geq 2} = \frac{1}{\sqrt{2}}\begin{pmatrix} \phi_{|\mathrm{n}|} \\ \pm\phi_{|\mathrm{n}|-2} \end{pmatrix},$$

where $\omega_c = eB/m = \hbar/(\lambda_B^2 m) = 2\hbar v^2/(\lambda_B^2\gamma_1)$ is the cyclotron frequency in bilayer graphene. Each of these levels is four-fold degenerate due to the combined two-fold spin and valley degeneracies. This derivation illustrates the existence of the eight-fold degenerate zero energy state, since the Hamiltonian $\begin{pmatrix} 0 & \pi^{\dagger 2} \\ \pi^2 & 0 \end{pmatrix}$ along with the relations in Equation (46) shows clearly that it is possible to act twice with $\mathcal{H}$ on the wave function $\begin{pmatrix} \phi_1 \\ 0 \end{pmatrix}$ and return a zero eigenvalue. In the monolayer case (Section 2.1), the Hamiltonian contains only linear powers of π, so it is possible to act only once to return the zero eigenvalue. The magnetic field dependence of these levels is contained entirely in $\omega_c = eB/m$, so that the Landau levels depend linearly on the field, in contrast to the monolayer where they show $\sqrt{B}$ dependence. Also, the Landau level spacing (i.e. the dependence on n) shows that the levels are nearly equally spaced, apart from the lowest few where the deviation of $\sqrt{|\mathrm{n}|(|\mathrm{n}|-1)}$ from equal spacing is not small. The eightfold degeneracy in the $\varepsilon = 0$ Landau levels is unusual amongst two-dimensional systems, and suggests that electron–electron interactions in a bilayer could give rise to a number of strongly correlated quantum Hall states. We defer its discussion until Section 3.4.5.

A more complete picture of the behavior of the Landau levels in bilayer graphene is given by the full four-band tight-binding model. In this case, the Hamiltonian in the same basis as used previously, i.e. where the wave function component orders are swapped between the K and K′ valleys is [190]

$$\mathcal{H} = \begin{pmatrix} U_0 - \xi U/2 & 0 & 0 & \xi v\pi^\dagger \\ 0 & U_0 + \xi U/2 & \xi v\pi & 0 \\ 0 & \xi v\pi^\dagger & U_0 + \xi U/2 & \gamma_1 \\ \xi v\pi & 0 & \gamma_1 & U_0 - \xi U/2 \end{pmatrix},$$

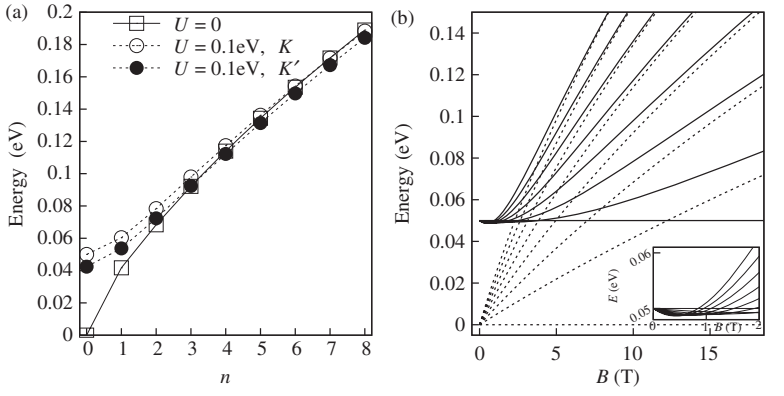

Figure 38. (a) The low-energy Landau levels as a function of level index n for zero and finite gap U at $B = 10$ Tesla. The lifted valley degeneracy is manifest for finite gap. (b) The first eight Landau levels as a function of magnetic field for zero and finite gap U in the K valley only. The gap causes additional level crossings at small magnetic field, and it is clear that the $n = 0$ level is constant as a function of field. The inset shows the LL spectrum for low magnetic field, displaying the additional crossings induced by the interlayer asymmetry. We have taken $\gamma_1 = 0.4\,\text{eV}$, $v = 1.0 \times 10^6\,\text{m s}^{-1}$ and $U_0 = 0$ throughout.

where U_0 is the average potential of the two layers, U is the total energy difference between the two layers, and as before, $\pi = p_x + eA_x + \text{i}(p_y + eA_y)$. The eigenvalues associated with this Hamiltonian are the solutions of the quartic polynomial

$$\left[(E_b(n,B) - U_0 + \xi U/2)^2 - (n+1)w^2\right]\left[(E_b(n,B) - U_0 - \xi U/2)^2 - nw^2\right] - \left[(E_b(n,B) - U_0)^2 - U^2/4\right]\gamma_1^2 = 0,$$

where $w = \sqrt{2}\hbar v/l_B$. Solutions to this equation cannot be written in a simple form (as they could for E^2 in the zero magnetic field case), so we present numerical evaluations of the eigenvalues in Figure 38. In this case, the labels of the Landau levels are defined as follows. The conduction and valence band each have their own ladder of levels, with indices $n = 0, 1, \ldots$. To distinguish one band from another, we use the label $b = c, v$ for the conduction and valence bands, respectively. The presence of a potential difference between the two layers gives rise to the splitting of the zero energy LL. The Mexican hat structure of the zero-field energy relation is replicated in the Landau level spectrum at low fields [175] by the fan of levels which cross each other in a complicated pattern (see the inset to Figure 38b). Pereira *et al.* [190] display a comparison of these levels with those derived from the two band approximation discussed above. They find that the two-band theory underestimates the Landau level energy at moderate field, but that the qualitative features of the levels are the same.

Some particular cases of this equation are easy to evaluate. Firstly, the $U = 0$ case yields the exact eigenvalues

$$E_b(n,B) = \pm\sqrt{\frac{(2n+1)\hbar^2 v^2}{l_B^2} + \frac{\gamma_1^2}{2} \pm \sqrt{\left(\frac{\hbar^2 v^2}{l_B^2} + \frac{\gamma_1^2}{2}\right)^2 + \frac{2n\gamma_1^2\hbar^2 v^2}{l_B^2}}},$$

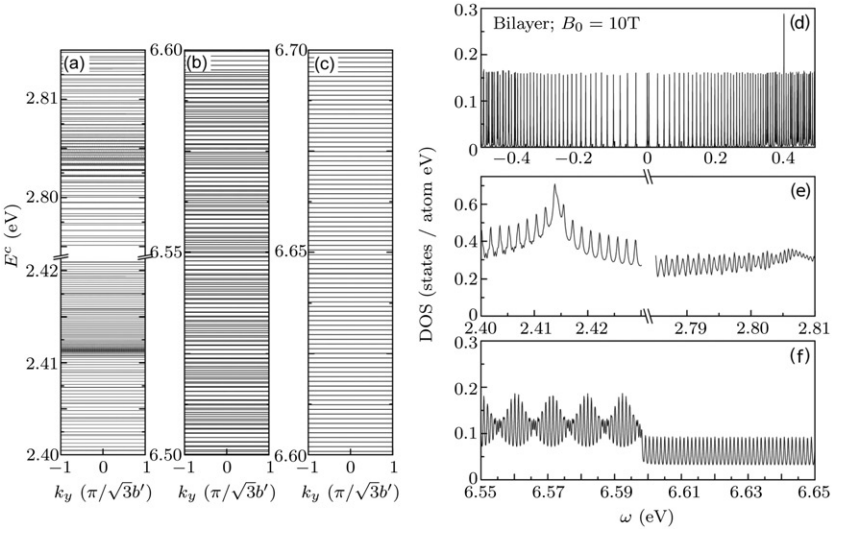

Figure 39. The (a) moderate- and (b,c) high-energy LLs of bilayer graphene at $B = 10$ Tesla. Density of states of bilayer graphene for $B = 10$ Tesla at (d) low, (e) moderate and (f) high energies (Reprinted figure with permission from Y.H. Lai *et al.*, Physical Review B, 77, 085426, 2008 [193]. Copyright © (2008) by the American Physical Society.).

where $b = c$ corresponds to the leading positive sign, and $b = v$ to the negative sign. This expression readily reduces to $E_b(0, B) = 0$, $\pm\sqrt{\hbar^2 v^2/l_B^2 + \gamma_1^2/2}$ for the $n = 0$ levels. In the symmetric case (i.e. when $U = 0$), both bands have $E(0, B) = 0$ as a solution, restoring the doubly degenerate lowest Landau level.

The Hofstadter butterflies for bilayer graphene have been examined by Nemec *et al.* [191], and transport properties in the case where the chemical potential exceeds γ_1 has been investigated by Nakamura *et al.* [192].

The Landau level spectrum for the high-energy bands of bilayer graphene was investigated by Lai *et al.* [193]. They used the tight-binding model without the continuum limit to explicitly diagonalize Hamiltonians corresponding to finite-sized bilayer graphene flakes in a magnetic field. They focused on three energy regions: the low-energy region where the results of analytical solutions of the continuum limit of the model were recovered; the high-energy limit where the Landau levels are composed of electrons originating from the split bands at zero field (Figure 39b and c) and the intermediate regime (Figure 39a). The intermediate regime corresponds to the region where the LL density is largest (Figure 39d–f), where a phenomenological broadening of $\Gamma = 0.5$ meV has been included) because the zero-field density of states is highest at the M point of the Brillouin zone. The non-uniformity of the LLs is due to the unequal spacing of LLs in this energy range (not captured in the low-energy approximation to the tight-binding model described above), and is enhanced by the presence of the second group of LLs arising from the split bands. This analysis also includes the interlayer couplings parametrized by γ_3 and γ_4, and the intralayer next-nearest neighbor hop t'.

3.4.3. *Magneto-optical properties of bilayer graphene*

The magneto-optical properties of bilayer graphene were first discussed theoretically by Abergel and Falko [151] who took the non-interacting picture of electrons in bilayer graphene and calculated the selection rules and optical strengths for inter-Landau level transitions.

The selection rules derived within the two-band low-energy effective theory (with Landau levels labelled by $n \in \{\ldots, -2, 0, 1, +2, \ldots\}$ as explained in the Endnote 6) are stated as follows: transitions between levels for which the magnitude of the LL index differ by one are allowed. For circularly polarized light with right-handed orientation (such that $\vec{\ell}_{\oplus} \propto \vec{\ell}_x - i\vec{\ell}_y$), the allowed transitions increase the magnitude of the Landau level index. For left-handed polarization ($\vec{\ell}_{\ominus} \propto \vec{\ell}_x + i\vec{\ell}_y$), allowed transitions decrease the Landau level index by one. This is illustrated in Figure 40(a), where arrows represent transitions corresponding to the absorption of radiation by the graphene flake. The associated absorption spectrum and a comparison with the monolayer spectrum is shown in Figure 40(b). Several points bear discussion, the first of which being that the LL spectrum is denser in the bilayer, so that the transition energies are smaller and the spectrum of peaks more tightly packed. This is a direct manifestation of the finite zero-field density of states at the charge-neutrality point in bilayer graphene. Secondly, the peak height shows a different pattern from the monolayer. Apart from a significantly larger lowest-energy peak, all peaks have the same height, in contrast to the monolayer peaks which steadily decrease in height. These selection rules also make it possible to distinguish experimentally between two possible ground states of the half-filled quantum Hall system. If the splitting $\hbar\beta\omega_c$ between the $n=0$ and $n=1$ levels is smaller than the Zeeman energy, then the arrangement of electrons between these two levels depends on the details of the correlations between them.[7] It is possible to imagine two model scenarios: first, if the interaction between spins and the magnetic field is strong

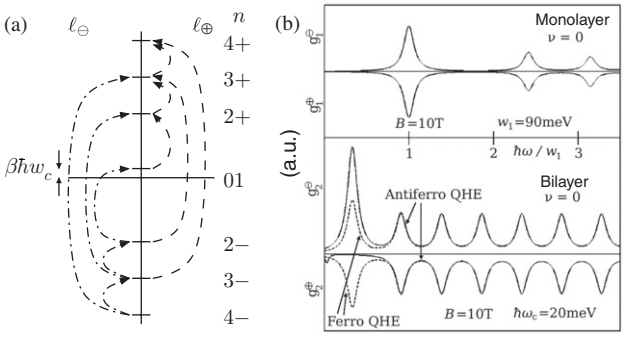

Figure 40. (a) Selection rules for inter-Landau level transitions in bilayer graphene. Allowed transitions in $\ell_\oplus$-polarized light increase the magnitude of the LL index by one, $\ell_\ominus$-polarized light allow transitions which reduce the magnitude of the LL index by one. (b) Monolayer (top) and bilayer (bottom) far infra-red absorption spectra in $\ell_\oplus$ and $\ell_\ominus$ polarizations for $B = 10$ Tesla and filling factor $\nu = 0$. Dashed and solid lines describe absorption by ferro- and antiferromagnetic states, respectively. The energy normalization is with respect to $w_1 = \sqrt{2}\hbar v/l_B$ (from [151]).

enough to overcome the gap between the levels, it will be energetically favorable for electrons to align their spins and fill half the states of both levels. This state is labelled 'ferromagnetic' as a description of the spin ordering. Second, if the correlations or other interactions force the $n = 0$ level to be filled and the $n = 1$ level to be empty, then we label the state 'antiferromagnetic'. The lowest absorption peak is determined by the $2- \rightarrow 1$ and the $1 \rightarrow 2+$ transitions, so the relative shape of this peak in the two polarizations acts as a probe of the electron ordering of these states. If the antiferromagnetic state is formed, there are electrons in only the $n = 0$ level, so the $1 \rightarrow 2+$ transition is not accessible and the peak in the $\ell_{\oplus}$ polarization in absent. On the other hand, if the ferromagnetic state is formed, the $n = 1$ is half-filled, so that both transitions are allowed. Therefore there are peaks in the absorption spectra of both polarizations. Additionally, the very low-energy peak corresponding to the $0 \rightarrow 1$ transition is only present in the $\ell_{\oplus}$ polarization.

The optical transitions in bilayer graphene were also examined within the four-band model in the single particle approximation by Pereira *et al.* [190] as a function of the asymmetry gap and magnetic field. They give analytical expressions for the oscillator strength for transitions, and show the dependence of the transition energy on the magnetic field (Figure 41a). The transition energies are only weakly dependent on the field strength for $B < 5$ Tesla, in contrast with both the monolayer and unbiased bilayer cases. Oscillator strengths for the same transitions are shown in Figure 41(b). There is an asymmetry between the conduction and valence band intra-band transition energies, which increases as the gap size increases, as shown in Figure 41(c). The oscillator strengths also are strongly effected by the gap, as shown in Figure 41(d).

The cyclotron resonance absorption has been studied experimentally, firstly by Sadowski *et al.* [34] who found signatures of the monolayer single particle description in few-layer epitaxial graphene samples, and more recently by Henriksen *et al.* [194]. In the latter work, infra-red spectroscopy was used to

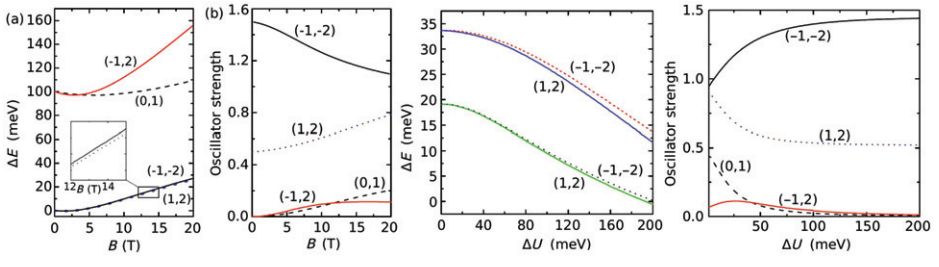

Figure 41. (Colour online) (a) Transition energies in a biased ($U = 100$ meV) graphene bilayer, as a function of the magnetic field B for the dipole-allowed transitions: $0+ \rightarrow 1+$ (black dashed line), $1+ \rightarrow 2+$ (blue dotted line), $1- \rightarrow 2-$ (black solid line), and $1- \rightarrow 2+$ (red solid line), and we use the four-band notation to label the Landau levels. (b) Oscillator strengths as a function of magnetic field for the transitions described in (a). (c) Transition energies as a function of the gap for $1+ \rightarrow 2+$ (blue solid line), and $1- \rightarrow 2-$ (red dashed line) transitions for $B = 20$ Tesla, and $1+ \rightarrow 2+$ (green solid line) and $1- \rightarrow 2-$ (black dotted line) for $B = 10$ Tesla. (d) Oscillator strengths for dipole-allowed transitions in a graphene bilayer as a function of the interlayer potential difference at $B = 5$ Tesla.

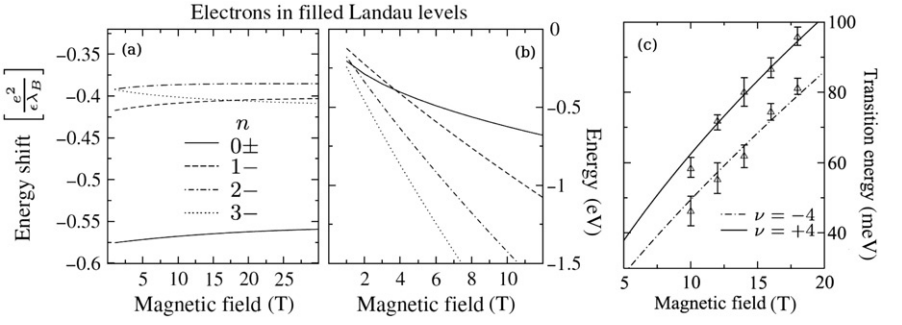

Figure 42. (a) Energy shift per electron of filled LLs. (b) The absolute energy per electron of filled LLs showing the crossing between the $n = 0\pm$ degenerate level and the higher LLs in the valence band. In both plots, $U = 0$. (c) Electron–hole asymmetry in the inter-LL optical transition energy. The experimental data (represented as points) are taken from [194, Figure 2]. The authors take $\gamma_1 = 0.4\,\text{eV}$, and $v = 0.95 \times 10^6\,\text{m s}^{-1}$ (from [195]).

measure the absorption spectrum of bilayer graphene and several significant differences were found between the expected results detailed above and the experimental data. Firstly, a significant (≈20%) electron–hole asymmetry was found for interband transitions. The authors speculated that this asymmetry was either intrinsic, or caused by residual charged impurities. Next, while the transition energies between higher levels follow a roughly $\sqrt{B}$ dependence, those involving the lowest Landau levels were linear in B. Additionally, the authors could not get their data to fit the single particle predictions using a single set of fitting parameters (γ_1 and v).

Several attempts have been made to explain these puzzling data. Firstly, Abergel and Chakraborty [195] used an exact diagonalization scheme [72] to point out that the long-range part of the electron–electron interaction is important in this system. They claim that the shift in the energy of a filled LL is significantly higher for the zero-energy LLs than for the higher energy LLs, as shown in Figure 42(a) and (b). This induces a large asymmetry in the energies of transitions that start in the zero-energy levels compared to those that finish in those levels. As shown in Figure 42(c), a single set of fitting parameters ($\gamma_1 = 0.4\,\text{eV}$, $v = 0.95 \times 10^6\,\text{ms}^{-1}$) describe the transitions involving the $n = 0, 1$ levels well. Mucha-Kruczyński *et al.* [196] calculated the single-particle transition energies including the self-consistent screening, and found that finite zero-bias asymmetry (i.e. $U_0 \neq 0$), combined with the screening could account for the electron–hole asymmetry in higher Landau levels. Huang *et al.* [197] studied wide bilayer nanoribbons numerically, finding Landau levels and optical spectra with many of the same features as the bulk system. Kusminskiy *et al.* [198] also included screening via the Thomas–Fermi approximation as a correction to the Hartree–Fock renormalized Landau levels, and found similar agreement between the experimental data and their theory. It is therefore clear that interlayer screening and many body effects are crucial in this system.

3.4.4. *The effect of trigonal warping on the Landau level spectrum*

The effects of the next-nearest neighbor hops characterized by γ_3 can be ignored for $\hbar/l_B > v_3 m$ [139], however, for a weak magnetic field, the trigonal warping and

associated Lifshitz transition (Section 3.2.2) adds significant complexity to the low-lying Landau levels. Strong γ_3 coupling makes Landau levels with $|\mathfrak{n}| \geq 3$ gain energy, while the $|\mathfrak{n}| = 2$ levels approach zero in energy [151]. The coupling also allows additional inter-Landau level transitions for the low-lying electrons, with transitions between states for which $|\mathfrak{n}| = |\mathfrak{n}'| \pm 2$ and $|\mathfrak{n}| = |\mathfrak{n}'| \pm 4$ now permitted, but with reduced optical strength $(v_3 m l_B/\hbar)^2$. This is reflected in the trace of the absorption spectrum. For example, the new peak present at ω/ω_c corresponds to transitions $3- \rightarrow 1$ and $1 \rightarrow 3+$.

3.4.5. *Electron–electron interactions in the zero-mode Landau levels*

The zero-mode Landau levels are those described in the two-band model by the indices $\mathfrak{n} = 0$ and $\mathfrak{n} = 1$. This model gives their energies as

$$E_0 = \frac{1}{2}\xi U, \quad \text{and} \quad \mathrm{E}_1 = \frac{1}{2}\xi U\big(1 - 2\hbar\omega_{\mathrm{c}}/\gamma_1\big),$$

where, as before, U is a phenomenological parameter which denotes the interlayer gap. The splitting of these two levels due to the kinetic term is $2\hbar\omega_c U/(2\gamma_1) \approx 8.2 \times 10^{-3}\ UB$. Ezawa [199,200] has predicted that the Coulomb interactions will split the eight-fold degeneracy into four two-fold degenerate bands, which are further split by Ising QH ferromagnetism at $\nu = \pm 1, \pm 3$. Therefore, the step in the QHE at zero density will be split into eight plateaus. Misumi *et al.* [201] study the effect of an in-plane electric field on the quartet of states which is split into the positive energy range by the layer asymmetry. In this case, a field-dependent gap $\omega_c\sqrt{(U/\gamma_1)^2 + 2(el_B\mathbf{E}_\parallel/\omega_c)^2}$ is opened between the $(0, K, \pm)$ and $(1, K, \pm)$ levels, which may be detectable in QHE measurements. As the in-plane field strength is increased, the contribution to the dielectric constant and electric susceptibility from these levels enhance those functions around $\nu = 2$. The low-energy excitations and intra-Landau level cyclotron resonance were studied by Barlas *et al.* [202] within the Hartree–Fock approximation. They give Hund's rules for the filling of the octet of levels defined by the $n = 0\pm$ states, where for high field and relatively small gap, the filling order goes such that real spin polarization is maximized, followed by valley pseudospin (which in the $n = 0\pm$ levels is the same as a which-layer pseudospin because of the form of the electron wave functions), followed by the LL pseudospin. This process gives rise to a finite LL pseudospin polarization at any odd-integer filling factor. Within the Hartree–Fock approximation, the low-energy collective modes show a roton minimum at $ql_B \approx 2.3$, there is no contribution to the exciton gap from electron–electron interactions at $q = 0$, and the band splitting approaches the Hartree–Fock theory result as $q \rightarrow \infty$. At odd-integer filling factors, there are intra-Landau level cyclotron resonance modes with frequency $\omega_{\mathrm{LL}} = 2\hbar v^2 U/(l_B\gamma_1)^2$ which may lead to QHE plateaus forming at these filling factors if $\omega_{\mathrm{LL}}\tau > 1$.

Abergel and Chakraborty [195] studied the effects of the long-range Coulomb interaction between electrons in the zero-mode octet within an exact diagonalization scheme [72] which allowed exact evaluation of the Coulomb matrix elements and inclusion of exchange and correlation effects. They found finite valley polarization

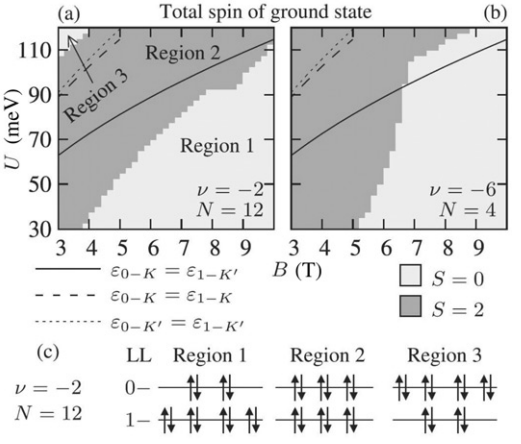

Figure 43. The total spin of the ground state of the (a) $\nu = -2$ and (b) $\nu = -6$ systems. The lines show the crossing points of the single-particle states. The graining is due to the finite interval between data points. (c) The occupancy of the single electron states in the interacting many body ground state for each region of the plot in (a).

at $\nu = -2$, -6 over a wide range of gap sizes and magnetic fields. Also, as shown in Figure 43, there is finite spin polarization for certain ranges of fields, corresponding to the interplay between the exchange energy and the splitting of the Landau levels as influenced by the size of the asymmetry gap. The filling of electron states within the octet explains the appearance of the spin polarization. In region 2 (the darker shaded areas), the pairing of electrons within the same Landau level is incomplete, allowing the exchange interaction to minimize the total energy by aligning the unpaired electrons' spins. In regions 1 and 3, all electrons are paired, so the exchange interaction is unable to rearrange the electrons' spins in this way.

Misumi and Shizuya [201,203] discussed the ground state and collective excitations of the zero modes, and their effects on the electronic susceptibility and dielectric constant. Ando [204] analyzed the coupling of electrons in LLs to optical phonon modes and investigated the shift in energy and mode broadening due to this coupling.

Another manifestation of the electron–electron interactions in the zero energy LLs is the gradual lifting of the eight-fold degeneracy as the magnetic field is increased. Transport measurements have shown that in suspended bilayer graphene [205] and exfoliated bilayer graphene on an SiO_2 substrate [206], quantum Hall plateaus appear for every integer value of the filling factor. The higher mobility of electrons in suspended bilayer graphene (Feldman *et al.* report $\mu = 1.5 \times 10^5\,\mathrm{cm^2\,V^{-1}\,s^{-1}}$ at electron density of $n = 2 - 3 \times 10^{11}\,\mathrm{cm^{-2}}$ compared to the exfoliated samples of Zhao *et al.* who measure $\mu = 1 \times 10^4\,\mathrm{cm^2\,V^{-1}\,s^{-1}}$ at $n = 4 \times 10^{12}\,\mathrm{cm^{-2}}$) mean that the degeneracy lifting happens at smaller magnetic field than in the exfoliated flakes. The heirarchy of degeneracy lifting is shown in Figure 44, where a schematic representation of the evolution of the Landau level degeneracy is given. We have marked the approximate fields at which each new

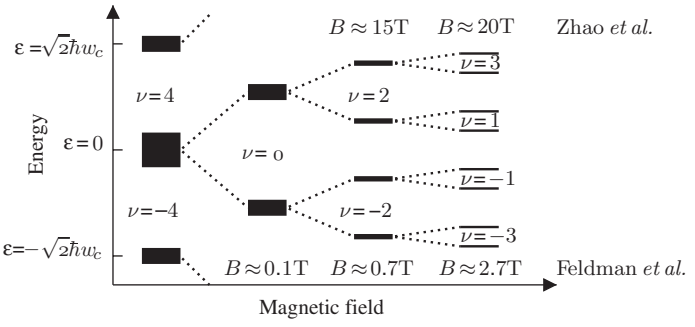

Figure 44. The order of Landau level degeneracy removal as magnetic field strength increases. The thickness of the line marking the Landau level indicates the degeneracy. The dotted lines mark the splitting of degenerate Landau levels. The magnetic field labels refer to the beginning of the emergence of each regime in the suspended case [205] (lower) and exfoliated case [206] (upper).

regime begins to present itself in the two experiments. Both authors note that disorder and Zeeman splitting are unlikely mechanisms for lifting the degeneracy (since the energy scales of these two effects are much smaller than the energy gaps), and interaction with charged impurities is unlikely because the effect is more apparent in the suspended samples. The authors of both papers therefore claim that it is electron–electron interactions which are responsible for this lifting of the degeneracy.

3.5. *Electron–electron interactions in bilayer graphene*

Although the electron–electron interactions do not seem to play an important role in the transport measurements conducted on bilayer graphene, they may have a significant effect on other physical properties of this system, especially the magnetism of the ground state. We therefore review the theoretical work on this topic. A variety of analytical techniques have been applied to this problem, and the key issue which discriminates between them is the role of screening. Screening is always more important in the bilayer than the monolayer, because there is a finite density of states at the K point, but in the gapped bilayer, the density of states shows a square-root divergence at the band edge, meaning that screening is particularly efficient in this case. Therefore, on-site Hubbard models have been considered for the biased bilayer, while the Hartree–Fock approximation, the RPA and variational techniques have been applied to the ungapped bilayer.

Nilsson *et al*. [207] were the first to examine the possibility of a magnetic ground state in bilayer graphene. Using a variational method, they found that a trial ground state with finite-spin polarization at half filling produced a lower total energy than the unpolarized system when the exchange energy associated with the long-range Coulomb interaction was taken into account. The parameter Q describes the 'size' of the electron or hole pockets in the density, and is taken to be the variational parameter. If the variational state is assumed to be such that there is one electron pocket in the up-spin channel, and one hole pocket in the down-spin channel at

each K point, then $n_{1,\uparrow}(p) = \theta(Q-p)$, $n_{1,\downarrow} = 0$ on the first layer, and $n_{2,\uparrow} = 1$, $n_{2,\downarrow} = 1-\theta(Q-p)$ on the second layer. The authors demonstrate that the optimal Q is $Q_{\min} = 0.05\gamma_1$, and that the system favors the formation of spin polarized electron and hole pockets. This calculation does not include the exchange interaction between electrons in opposite K points. Adding this energy favors a state with net ferromagnetism, and lifts the degeneracy between trial ground states with and without the Z_2 symmetry. The induced ferromagnetism is predicted to be up to the order of $10^{-5}\ \mu_B$ per carbon atom. Short-range interactions were also considered in a Hubbard model, and c-axis antiferromagnetism is predicted.

Hwang *et al.* [208] applied the RPA to ungapped bilayer graphene to derive the polarization function, and hence discuss the dielectric properties and associated screening, the Kohn anomaly, Friedel oscillations and the RKKY interaction. Using the two band model, intrinsic (i.e. undoped) bilayer graphene is shown to have a constant polarization function $\Pi^0(q) = \frac{gm}{2\pi}\log 4$ (where $g=4$ is the band degeneracy factor, and m is the effective mass) so that the dielectric function is $\epsilon(q) = 1 + \frac{gme^2}{\kappa q}\log 4$. Also, this constant polarization function means that the Coulomb potential has no oscillatory terms (i.e. no Friedel oscillations), in contrast to the monolayer and traditional 2DES. The asymptotic radial dependence is $1/r^3$, as opposed to $1/r$ in the monolayer.

In extrinsic bilayer graphene, there are contributions to the polarizability from both the intra- and inter-band transitions. This quantity is plotted in Figure 45, where the intra-band, inter-band, and total polarizations are shown separately. In the bilayer, the polarizability is constant for $q < k_F$, but for $q > k_F$ the cancellation between the intra- and inter-band contributions is not exact due to the enhanced backscattering associated with the inter-band transitions. Therefore, the polarization function increases up to $q = 2k_F$. At this point, the chirality-induced enhancement to the wide angle scattering generates a cusp (with discontinuous first derivative): behavior which is in line with the 2DES, but sharply opposed to that of the SLG. In the large momentum limit, the polarization converges to the constant $\frac{gm}{2\pi}\log 4$ because the inter-band processes dominate over the intra-band ones. This is again different from the 2DES, where the polarizability falls as $1/q^2$. The cusp at

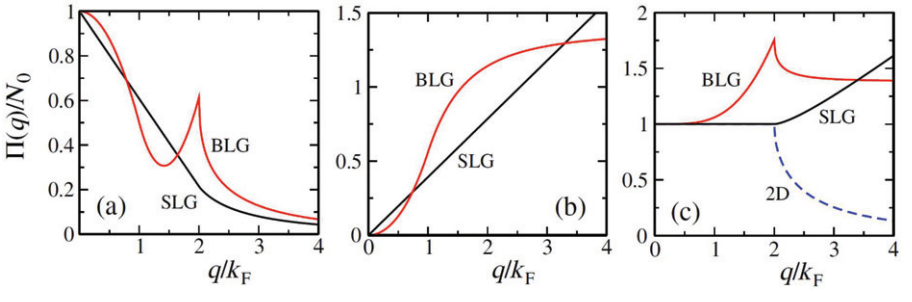

Figure 45. Calculated (a) intraband, (b) interband, and (c) total static polarizability of bilayer graphene. For comparison, the single-layer polarizabilities are shown. In (c), the authors also show the regular 2D static polarizability (dashed line) (Reprinted figure with permission from E.H. Hwang and S. Das Sarma, Physical Review Letters, 101, 156802, 2008 [208]. Copyright © (2008) by the American Physical Society.).

$q = 2k_F$ leads to Friedel oscillations and a strong Kohn anomaly (Section 3.6). Finally, the authors discussed the RKKY interaction between two magnetic impurities. For an intrinsic bilayer, the magnetic moments are not correlated due to the constant polarization function, and there is no net magnetic moment. In doped BLG, the singularity at $q = 2k_F$ restores the oscillatory term in the RKKY interaction, and behavior very similar to the 2DES is recovered.

In the case of the biased bilayer, the presence of the non-trivial Fermi surface at low density causes behaviour which departs from the standard Fermi liquid type. Stauber *et al.* [209] investigated this regime using the first-order correction to the electron self energy which renormalizes the band parameters such that

$$E(k) \approx \Delta_1 - \alpha_1 k^2 + \lambda_1 k^4, \quad \Delta_1 = \Delta - \frac{e^2}{\epsilon_0}\Delta k, \quad \alpha_1 = \alpha + \frac{e^2}{4\epsilon_0}\frac{\Delta k}{k_\times},$$
$$\lambda_1 = \lambda - \frac{3e^2}{64\epsilon_0}\frac{k_{\max}^3 - k_{\min}^3}{k_\times^3},$$

where $\Delta k = k_{\max} - k_{\min}$, and $k_\times = k_{\max}k_{\min}$ and Δ, α, and λ are the bare band parameters. The momenta $k_{\min}$ and $k_{\max}$ are the lower and upper extent of the Fermi ring. This renormalization means that for $\lambda_1 \leq 0$, the spectrum is unbounded and an instability may occur in the non-interacting system. To examine this possibility, the authors include the exchange part of the Coulomb interaction between electrons. When this contribution is considered with the bare band parameters, it is found that the Fermi ring is unstable with respect to ferromagnetism, with a second-order transition. When the renormalization due to the self-energy corrections is included, this tendency is reduced, (although there is a critical density at which the phase transition will occur) and the magnetization is saturated at $n > 5 \times 10^{11}\,\mathrm{cm}^{-2}$. At low densities, the ferromagnetic ordering is not affected by the self-energy corrections and will be present at $T = 0$. The authors also examined the polarization function in the Mexican hat regime, and it was found that the electron gas in the biased bilayer deviates from the standard Landau Fermi liquid theory for intermediate energies, and at low energies, the Fermi liquid result is obtained except at wave numbers which directly connect two parallel parts of the Fermi surface. The presence of two Fermi lines implies that the Friedel oscillations have period π/b (where $2b = k_{\max} - k_{\min}$). Finally, the plasmon spectrum shows features typical of a 2DES, although the energy scale is larger than the traditional systems by virtue of the low electron mass.

The logarithmic divergences which appear within the Hartree–Fock approximation of the band parameter renormalization can be removed by adding Thomas–Fermi screening to the calculation [198]. When this screening is taken into account, the renormalized bands disperse more slowly than in the Hartree–Fock case.

Ferromagnetism has been investigated in the Hubbard model near the band edge by Castro *et al.* [210]. They claim that the high density of states at the band edge, and resulting screening of the long-range part of the Coulomb interaction makes this model applicable in this context. There is a critical value of the gap, U_c above which the ferromagnetism becomes unavoidable because of the change in band parameters for the up-spin and down-spin bands. To illustrate this, Figure 46(a) shows the Hartree–Fock bands for three different values of the gap U. In the case $U < U_c$, there is no splitting between the different spin bands and the magnetization m and

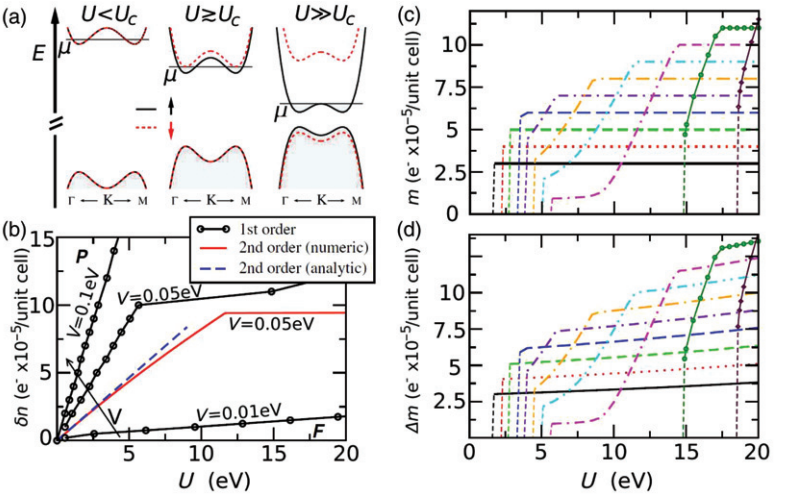

Figure 46. (a) Hartree-Fock bands for ↑ (solid lines) and ↓ (dashed lines) spin polarizations. (b) The U vs δn phase diagram at $T=0$: symbols are inferred from (c) and signal a first-order transition; lines stand for the second-order transition. (c) The $T=0$ solution for magnetization. (d) The $T=0$ solution for the layer difference in magnetization. In (c) and (d), the successive lines represent different layer asymmetry in the electron density, with the lowest magnetization corresponding to the smallest density imbalance (Reprinted with permission from E.V. Castro *et al.*, Physical Review Letters, 100, 187803, 2008 [210]. Copyright © (2008) by the American Physical Society.).

interlayer magnetization difference Δm are both trivially zero. When the gap is a little above the critical value ($U \gtrsim U_c$), the degeneracy of the spin states in the conduction band is lifted which gives rise to a finite magnetization, $m \neq 0$. That the degeneracy in the valence band is not lifted means that $\Delta m \approx m$, as shown in Figure 46(c) and (d). When $U \gg U_c$, the valence band does become non-degenerate, and the magnetization is opposite in the two layers, so that $\Delta m > m$. Finite temperature does not change this picture to any great extent. Also, it is clear that $|\delta n| < |\Delta n|$ implying that the electron density is above the Dirac point in one plane, and below it in the other. This is natural, since the tight-binding model shows that valence band states are located mainly in the layer at low potential, and conduction band states are located mainly in the layer at high potential. Finally, Figure 46(b) illustrates a comparison of the self-consistent analysis (lines with dots) and the approximate analytical estimates assuming a second-order transition. It is clear that the ferromagnetic-paramagnetic transition in this system is actually first order.

The electron compressibility is a physically measurable quantity which reveals much information about the interaction effects in electron gases. The compressibility of the bilayer has been calculated within the Hartree–Fock approximation by Kusminskiy *et al.* [211]. At very small doping, compressibility is negative and divergent, as in a 2DES. The inter-band contribution tends to move the region of negative compressibility to smaller densities, so that this contribution reduces compressibility. However, similar calculations for the compressibility of the monolayer [212] produce a 10–15% renormalization of the electron velocity, similar to that found in experiment [213].

Table 2. Table of phonon frequencies.

Γ-point mode	Yan *et al.* [215]	Saha *et al.* [214]
E_g	1587	1594.1
E_u	1592	1598.9
$E_g \Rightarrow E^*$(low)		35.0
$A_{1g} \Rightarrow A^*$(low)		76.8
$A_{1g} \Rightarrow A^*$(high)		900.8
A_{2u}		903.3
K-point mode		
E	1318	

Note: Units are cm^{-1} throughout.

For more details on the nature of plasmon dispersion and compressibility in monolayer and bilayer graphene, see Section 4.

3.6. *Phonon anomalies and electron–phonon coupling*

Phonons and the electron–phonon coupling are important topics because of the intimate links that the subject has with Raman spectroscopy, a key experimental tool in the study of graphene.

First-principles studies of phonons in mono-, bi- and few-layer graphenes have been carried out [214,215]. Saha *et al.* [214] determine the dependence of the energy of various low-momentum phonon modes on the number of layers and find strong layer dependence for out-of-plane modes, and relatively weak layer dependence for in-plane modes. In Table 2, we summarize the available data for the frequency of the phonon modes discussed. Yan *et al.* [215] show how the E_{2g} peak splits into two modes which are split by approximately $5\,cm^{-1}$.

Various authors have discussed phonon anomalies in bilayer graphene, so a brief outline of the physics is in order. For reference, the original description of phonon anomalies in monolayer graphene was given by Piscanec *et al.* [216], but in this section we describe the phonons in bilayer graphene only. Yan *et al.* [217] show the change of phonon frequency ω_{ph} as a function of the Fermi energy (Figure 47d), with the anomaly occurring when the inter-band electron–hole excitation is in resonance with the phonon mode. The change of phonon frequency with the tuning of the Fermi energy is given by

$$\hbar\omega_{ph}(E_F) - \hbar\omega_{ph}(0) \sim -\lambda \int_0^{2|E_F|} dE_{e-h} \frac{2E_{e-h}}{\hbar^2\omega_{ph}^2 - E_{e-h}^2} \sim \lambda \ln\left|1 - \frac{2|E_F|}{\hbar\omega_{ph}}\right|,$$

where λ is the electron–phonon coupling parameter. This anomaly was observed experimentally by Das *et al.* (Figure 48a), whereas it has not yet been observed in the monolayer. Yan *et al.* speculate that the reason for this is the intrinsic charge inhomogeneity in graphene causes a larger variation in the Fermi energy in the monolayer than it does in the bilayer, and to be qualitative about this idea, the authors show the evolution of the anomaly size as a function of charge non-uniformity. This anomaly was not seen by later experiments [218], and this is probably due to the large

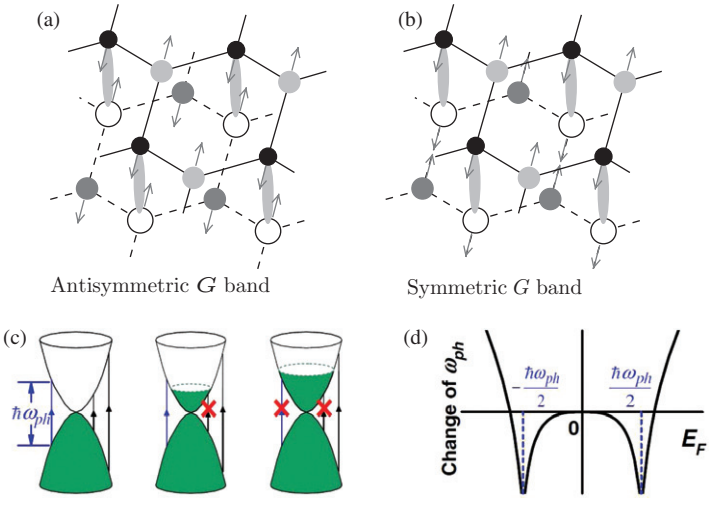

Figure 47. Phonon modes in bilayer graphene where the grey arrows represent the direction of vibration of each atom. (a) The antisymmetric G band mode is a distortion of the zigzag lines where the layers are out of phase. (b) The symmetric G band mode is a distortion of the zigzag lines where the layers are in phase. (c) Vertical ($q=0$) inter-band electron–hole pair transitions in a gapless 2D semiconductor with three different Fermi levels. Shaded regions are filled with electrons, and the transition indicated by the arrow is the resonance with the long-wavelength optical phonon (From [217]). (d) Predicted change of phonon energy as a function of the Fermi energy. The two phonon anomalies show up at $E_F = \pm\hbar\omega_{ph}/2$ (Reprinted figure with permission from J. Yan *et al.*, Physical Review Letters, 101, 136804, 2008 [217]. Copyright © (2008) by the American Physical Society.).

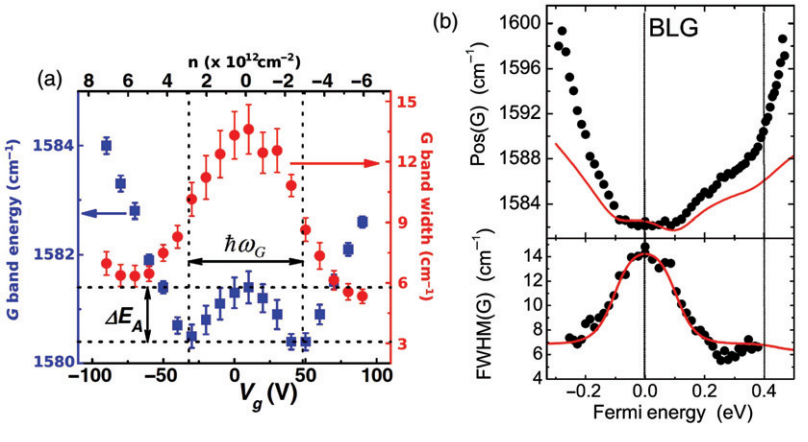

Figure 48. (a) Experimental energy and linewidth of the G band. Two phonon anomalies are clearly resolved in the phonon energy (Reprinted figure with permission from J. Yan *et al.*, Physical Review Letters, 101, 136804, 2008 [217]. Copyright © (2008) by the American Physical Society.). (b) The position of the G peak, and its full width at half-maximum plotted as a function of Fermi energy (Reprinted figure with permission from A. Das *et al.*, Physical Review B, 79, 155417, (2009) [219]. Copyright © (2009) by the American Physical Society.).

charge non-uniformity, and because these experiments were carried out at room temperature. Malard *et al*. measured the phonon frequency shift when a finite interlayer asymmetry potential is applied. The breaking of the layer symmetry allows the antisymmetric mode to become active in Raman spectra, causing the *G* band to split into two peaks (see schematic representation of the displacements associated with each phonon mode in Figure 47a and b). Frequency differences of $\sim 15\,\mathrm{cm}^{-1}$ are observed between the two modes for large negative bias, and comparison with theoretical predictions shows that the measured shift of the symmetric phonon is significantly larger than predicted, while the shift of the antisymmetric phonon is in line with predictions. Symmetry analysis of bilayer graphene phonons in the presence of an external electric field [219] reproduces the qualitative features. Castro Neto *et al*. [220] have used a simple one-loop calculation within the tight-binding model to compute the electronic susceptibility of bilayer graphene, and related it to the frequency shift of the phonon mode due to the electron–phonon coupling. They find that the shift is linear in the electron density *n*, and negative:

$$\delta\omega_{\vec{Q}}^{\mathrm{bil}} \propto -\left(\frac{\partial t}{\partial l}\right)^2 \frac{n}{M_C \omega_{\vec{Q}} \gamma_1},$$

where M_C is the mass of a carbon atom, l is the lattice constant, with $\partial t/\partial l \approx 6.4\,\mathrm{eV\,\AA}^{-1}$, and $\omega_{\vec{Q}}$ is the frequency of a phonon with wave vector $\vec{Q}$.

On the other hand, Das *et al*. [221] report that the *G* peak frequency is renormalized as a function of doping, outside of a the range $-0.1\,\mathrm{eV} < E_F < 0.1\,\mathrm{eV}$, which corresponds to the $\hbar\omega_0/2$ anomaly discussed above. There is also a kink at $E_F \approx 0.4\,\mathrm{eV}$. These results are explained with reference to the doping and dynamic effects, and the presence of the kink is related to the Fermi energy moving to the split band. This phonon anomaly has also been discussed theoretically by Ando [204] within the one-loop approximation for the phonon self energy. The logarithmic singularity in the frequency shift is derived for the symmetric *G* mode when the interlayer potential is zero, but a finite-disorder potential curtails the singularity and broadens the phonon mode. On the other hand, the antisymmetric *G* mode does not display the singularity and the broadening is significantly reduced for $E_F < \gamma_1$ because inter-band transitions are suppressed. In the case of finite-interlayer bias, the screening is taken into account self-consistently by Ando [222]. The presence of the band gap modifies the phonon renormalization, the symmetric and antisymmetric *G* modes mix strongly, and an asymmetry between the phonon frequencies at positive and negative electron concentrations is induced. This asymmetry becomes considerable when the gap size is of the order of the phonon frequency, and in this case, resonant inter-band contributions between the two low-energy bands and the frequency of the low-frequency mode (dominantly symmetric) are reduced strongly, and broadened.

3.7. *Device proposals utilizing bilayer graphene*

In this section we outline some of the devices that have been proposed which utilize bilayer graphene in their operation. Transistor and current switching devices were discussed in Section 3.3, so we do not repeat that material here. We shall describe two proposals for valleytronic devices (utilizing the valley quantum number as a

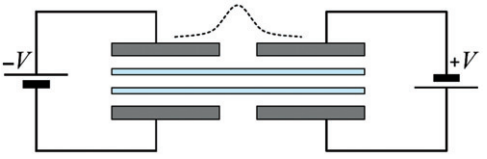

Figure 49. Side view of a gated bilayer graphene configuration with the voltage kink. The region where the interlayer voltage changes sign (the channel) supports bands of chiral zero modes (dashed line). The conventional (non-topological) confinement would correspond to the same polarity of bias on both sides of the channel (Reprinted figure with permission from I. Martin *et al*., Physical Review Letters, 100, 036804, 2008 [223]. Copyright © (2008) by the American Physical Society.).

controllable two-state system), and two for employing the pseudospin (i.e. the sublattice index) in the same way.

Martin *et al*. [223] describe a device which utilizes a split gating arrangement to confine electrons in zero modes in a 1D channel (Figure 49). These electrons are chiral in the valley index, so that their direction of propagation is determined by which valley they are in. A valley filter may be observed by applying a potential difference along the voltage kink, since the resulting current would consist of only one valley species. A valley valve can be implemented by placing two such filters in series. If the polarity of the filters is the same then current will pass, if it is opposite then current will not flow. The polarity of each valve can be reversed by swapping the orientation of the bias potentials on each side of the channel.

Abergel and Chakraborty [224] demonstrated that irradiating gated bilayer graphene with intense, circularly polarized, terahertz frequency light leads to the creation of valley polarized dynamical states in the gapped region of the spectrum. By passing an arbitrary current through these states, the current is polarized into the valley in which the states reside. Swapping the polarization of the top gate, or the orientation of the circular polarization of the light causes the valley in which the dynamical states form to be swapped also. Currents of the order of a tenth of a pico-Amp, and valley polarizations above 99% are predicted to be obtained. These devices can be used individually to generate valley polarized currents, or in series to implement switching devices. The valley-polarized currents exist in the bulk of the bilayer graphene (rather than localized at a sample edge, or in a narrow channel), and may be used as an analogue of spin-polarized currents in spintronics. The fact that this device relies on a bulk effect also gives it the distinct advantage that the details of the edges make no difference to its operation, which makes the device significantly easier to fabricate than those that utilize specific properties of certain edge geometries in their operation.

San-Jose *et al*. [225] propose a pseudospin valve employing gapped bilayer graphene. Their device consists of two-gated regions which are biased so that there is a finite gap at the charge-neutrality point which induces an out-of-plane component of the pseudospin. If the two regions have opposite polarity and the distance between the two regions is small enough, then electron will be unable to rotate its pseudospin quickly enough to allow it to penetrate the region of opposite polarization and reflection will occur at the interface between the two regions. Conversely, if the two regions are arranged with the same polarity, no such reflection will take place.

Pseudo-magnetoresistance of approximately 100% were suggested for optimal device dimensions of a pseudospin transistor.

Min *et al*. [226] proposed pseudospin ferromagnetism in gated bilayer graphene, which may have analogous applications to the real spin in spintronic systems. They demonstrated that high-gate voltage polarizes the pseudospin, and speculate that pseudospin-transfer torques, and easy switching behavior can be accomplished.

4. Many-body and optical properties of graphene

In this section, we discuss some of the novel electronic properties of graphene, where the electron–electron interactions traditionally play an important role. We begin in Section 4.1 with a discussion of the measurement of compressibility in monolayer graphene [213] and the reported theoretical studies [227] to understand the experimental results. In Section 4.2 we discuss the theoretical studies of plasmon dispersion in monolayer and bilayer graphene. We also review the properties of graphene in an intense electromagnetic field (EMF) in Section 4.3.

4.1. *Electronic compressibility*

In an interacting electron system of uniform density, the (inverse) electronic compressibility $\kappa^{-1} \propto \partial\mu/\partial n$ (where μ is the chemical potential and n is the electron density) is a fundamental physical quantity that is intimately related to the strength of inter-electron interactions [228,229]. First measured for a two-dimensional electron gas in 1992 [230], the compressibility provides valuable information about the nature of the interacting ground state, particularly in the strong coupling regime where (in addition to the exchange energy) the Coulomb interaction is known to play a dominant role. In this section, we begin by reviewing the surprising experimental results by Martin *et al*. [213] for the compressibility of monolayer graphene, and continue to describe attempts to understand them from a theoretical point of view. We then review the same physics in the bilayer material, highlighting the intriguing differences between these two systems.

4.1.1. *Monolayer graphene*

A recent report on the measurement of electronic compressibility in monolayer graphene revealed behavior which was totally unexpected [213]. In this work, scanning single-electron transistor microscopy was used to measure the change of local electrostatic potential (and thereby change in local chemical potential) of a graphene sample when the carrier density was modulated [213]. The observed results for the local inverse compressibility were found to be quantitatively described by the kinetic energy alone (with the electron velocity renormalized by 10–15%) and the authors speculated that the exchange and correlation energy contributions to the compressibility either cancel each other out or are negligibly small. This interesting puzzle has remained unsolved because the approximate theoretical schemes adopted by various authors to investigate electron correlations in graphene [231,232] do not find any such cancellations. Similarly, the recently reported Hartree–Fock studies of compressibility [211,212] in monolayer and bilayer graphene do not consider

electron correlations at all, although they do correctly predict the velocity renormalization.

Abergel *et al*. [227] investigated the role of electron correlations in monolayer and bilayer graphene. They showed how in monolayer graphene, two fundamental properties of the system, namely, the linear energy dispersion and chirality conspire to allow complete cancellation of exchange and correlation contributions just as was observed in the experiment [213]. On the other hand, in bilayer graphene where the low-energy quasiparticles are massive chiral fermions, the parabolic dispersion does not allow this cancellation of the two energies, and the kinetic energy retains a dependence on the electron correlation function which manifests in the electron compressibility.

As discussed elsewhere in this review (Sections 1.2 and 5.2), the low-energy charge carriers in monolayer graphene behave as massless Dirac fermions described by a single-particle Hamiltonian which is linear in momentum $\vec{p}$. The eigenstates of the Hamiltonian are uniquely labelled by quantum numbers representing the wave vector $\vec{q} = \vec{p}/\hbar$, the band (conduction/valence) b, valley (pseudospin) ξ and the z-component of the real electron spin σ. The wave functions are of the form, $\psi(\vec{r}) = \mathrm{e}^{\mathrm{i}\vec{q}\cdot\vec{r}}\chi$, where χ is, in the most general case, an eight-component spinor [3]. The wave function can be written in an abbreviated basis by ignoring the spin, and swapping the order of the sublattice components in the two valleys to recover the Hamiltonian given in Section 1.2.

A full analytical study of the many-electron system in graphene is clearly an impossible task. However, most of the clues to the puzzle involving the measured compressibility described above can be found at the level of two electrons, which is amenable to a fully analytic solution. One could therefore start with a two-electron system where the electrons occupy the states ψ_α and ψ_β with α and β corresponding to the full sets of quantum numbers $(\vec{q}_{\alpha,\beta}, b_{\alpha,\beta}, \xi_{\alpha,\beta}, \sigma_{\alpha,\beta})$. Let us denote by φ the antisymmetric non-interacting two-electron wave function

$$\varphi(\vec{r}_1, \vec{r}_2) = \frac{1}{\sqrt{2}}\big[\psi_\alpha(\vec{r}_1)\psi_\beta(\vec{r}_2) - \psi_\beta(\vec{r}_1)\psi_\alpha(\vec{r}_2)\big], \tag{47}$$

where the subscript labels refer to the independent coordinates of the two electrons. The correlations due to the mutual Coulomb interaction are introduced by multiplying the free-particle wave function by a generic correlation factor F as

$$\Psi = F(\vec{r}_1, \vec{r}_2)\varphi(\vec{r}_1, \vec{r}_2). \tag{48}$$

At this stage, a precise definition of F is not necessary. The only requirements are that it should be a real function, and to preserve the antisymmetry of the correlated wave function Ψ it is assumed to be symmetric with respect to exchange of the particle coordinates, i.e. $F(\vec{r}_1, \vec{r}_2) = F(\vec{r}_2, \vec{r}_1)$.

In order to evaluate the two-particle energy we have to normalize the wave function Ψ. A straightforward calculation gives

$$||\Psi||^2 = \langle\Psi|\Psi\rangle = \int \mathrm{d}\vec{r}_1\, \mathrm{d}\vec{r}_2\, F(\vec{r}_1, \vec{r}_2)^2 \left\{1 - \frac{1}{2}\delta_{\xi_\alpha\xi_\beta}\big[1 + b_\alpha b_\beta \cos(\theta_\alpha - \theta_\beta)\big]\cos Q\right\},$$

where $Q = (\vec{q}_\beta - \vec{q}_\alpha)\cdot(\vec{r}_1 - \vec{r}_2)$ and $\theta_{\alpha,\beta}$ are the polar angles of the momenta $\vec{q}_{\alpha,\beta}$.

Evaluation of the expectation value of the kinetic part of the non-interacting two-body Hamiltonian leads us to

$$
\begin{aligned}
T^{\mathrm{mon}} = \frac{1}{2}\hbar v_{\mathrm{F}} \int \mathrm{d}\vec{r}_1\, \mathrm{d}\vec{r}_2\, F \Bigg\{ & \frac{1}{4}\mathrm{i}\delta_{\sigma_\alpha\sigma_\beta}\delta_{\xi_\alpha\xi_\beta}\Big[\mathrm{e}^{\mathrm{i}Q} Z^1_{\alpha\beta}\big(1 + b_\alpha b_\beta \mathrm{e}^{-\mathrm{i}(\theta_\beta-\theta_\alpha)}\big) \\
& + \mathrm{e}^{\mathrm{i}Q} Z^2_{\beta\alpha}\big(1 + b_\alpha b_\beta \mathrm{e}^{\mathrm{i}(\theta_\beta-\theta_\alpha)}\big) + \mathrm{e}^{-\mathrm{i}Q} Z^1_{\beta\alpha}\big(1 + b_\alpha b_\beta \mathrm{e}^{\mathrm{i}(\theta_\beta-\theta_\alpha)}\big) \\
& + \mathrm{e}^{-\mathrm{i}Q} Z^2_{\alpha\beta}\big(1 + b_\alpha b_\beta \mathrm{e}^{-\mathrm{i}(\theta_\beta-\theta_\alpha)}\big)\Big] \\
& - \mathrm{i}b_\beta\Big(\cos\theta_\beta \frac{\partial F}{\partial x_1} + \cos\theta_\beta \frac{\partial F}{\partial x_2} + \sin\theta_\beta \frac{\partial F}{\partial y_1} + \sin\theta_\beta \frac{\partial F}{\partial y_2} + 2\mathrm{i}q_\beta F\Big) \\
& - \mathrm{i}b_\alpha\Big(\cos\theta_\alpha \frac{\partial F}{\partial x_1} + \cos\theta_\alpha \frac{\partial F}{\partial x_2} + \sin\theta_\alpha \frac{\partial F}{\partial y_1} + \sin\theta_\alpha \frac{\partial F}{\partial y_2} + 2\mathrm{i}q_\alpha F\Big)\Bigg\},
\end{aligned}
$$

where we use the shorthand

$$
Z^j_{\alpha\beta} = \big(b_\beta \mathrm{e}^{\mathrm{i}\theta_\beta} + b_\alpha \mathrm{e}^{-\mathrm{i}\theta_\alpha}\big)\frac{\partial F}{\partial x_j} - \mathrm{i}\big(b_\beta \mathrm{e}^{\mathrm{i}\theta_\beta} - b_\alpha \mathrm{e}^{-\mathrm{i}\theta_\alpha}\big)\frac{\partial F}{\partial y_j} + \mathrm{i}q_\beta F\Big(b_\beta + b_\alpha \mathrm{e}^{\mathrm{i}(\theta_\beta-\theta_\alpha)}\Big).
$$

Due to the linearity of the single-particle Hamiltonians in the momentum operators, only first-order derivatives appear in the integrand. Terms in T of the form

$$
\int \mathrm{d}\vec{r}_j\, F\frac{\partial F}{\partial x_j} = \frac{1}{2}\int \mathrm{d}\vec{r}_j \frac{\partial}{\partial x_j} F^2,
$$

clearly vanish due to the antisymmetry of the integrand. Most of the terms left after the volume integration cancel each other as a consequence of the spinor structure of the single-particle wave functions. The only surviving terms sum to

$$
T^{\mathrm{mon}} = \hbar v_{\mathrm{F}}(b_\alpha q_\alpha + b_\beta q_\beta)||\Psi||^2,
$$

that is, the kinetic energy expectation value $\langle \mathcal{T}^{\mathrm{mon}} \rangle$ is simply the sum of the single free-particle kinetic energies,

$$
\langle \mathcal{T}^{\mathrm{mon}} \rangle = \frac{T^{\mathrm{mon}}}{||\Psi||^2} = \hbar v_{\mathrm{F}}(b_\alpha q_\alpha + b_\beta q_\beta) = T_0 = \frac{\langle \varphi | \mathcal{T}^{\mathrm{mon}} | \varphi \rangle}{||\varphi||^2} \tag{49}
$$

and does not depend on the correlation function F at all. Similar cancellations are expected for higher electron numbers, although analytical expressions become intractable even at the level of three electrons. This is a very interesting result since complete cancellation of correlation contributions to the kinetic energy has never been observed in conventional electron systems. It creates an unusual situation with interesting consequences, as described in [227]. In the thermodynamic limit, the potential energy (per particle) $\mathcal{V}$ is usually expressed in the form

$$
\langle \mathcal{V} \rangle = n \int \mathrm{d}\vec{r}\,[\,g(r) - 1]V_{\mathrm{Coul}}(r),
$$

where n is the single particle number density, $V_{\rm Coul}$ is the Coulomb potential and $g(r)$ is the pair correlation function which, for $\vec{r} = \vec{r}_1 - \vec{r}_2$, is given by

$$g(|\vec{r}|) = \frac{N(N-1)}{||\Psi||^2 n^2} \int \mathrm{d}\vec{r}_3 \ldots \mathrm{d}\vec{r}_N \, |\Psi(\vec{r}_1, \vec{r}_2, \vec{r}_3, \ldots, \vec{r}_N)|^2,$$

where N is the total number of electrons. The energy (per particle) functional $\mathcal{E}^{\rm mon}$ is now

$$\mathcal{E}^{\rm mon} = t_0 + \langle \mathcal{V} \rangle = t_0 + n \int \mathrm{d}\vec{r} \, [g(r) - 1] V_{\rm Coul}(r), \tag{50}$$

where $t_0 = T_0/N$ is the kinetic energy per particle. Its variation with respect to $g(r)$ (an essential step in determining the optimal $g(r)$ and hence the optimal F) would yield an unusual Euler–Lagrange equation, $V_{\rm Coul}(r) = 0$, which is clearly not the case in graphene [233]. To resolve this dilemma, Abergel *et al.* noted that the energy functional $\mathcal{E}^{\rm mon}$ is actually not bounded below: one can choose correlations such that the potential energy takes arbitrarily large negative values. This implies that to determine the optimal $g(r)$, the energy functional derived above is not sufficient and additional physical constraints, for example, that $g(r)$ should correspond to the correct number of states in the bands would be necessary[8]. Clearly, determination of the optimal pair-correlation function for massless Dirac fermions in graphene is a challenging problem [234]. However, the expression for the functional $\mathcal{E}^{\rm mon}$ is of the correct form, i.e. once the correct pair-distribution function $g(r)$ is found, one could evaluate the correct energy from the above form of the energy functional.

Let us now turn our attention to the electron compressibility. To that end, we first evaluate the variation $\delta_n \mathcal{E}^{\rm mon}$ of $\mathcal{E}^{\rm mon}$ with respect to n [227]:

$$\delta_n \mathcal{E}^{\rm mon} = \frac{\partial t_0}{\partial n} \delta n + \delta n \int \mathrm{d}\vec{r} \, [g(r) - 1] V_{\rm Coul}(r) + n \int \mathrm{d}\vec{r} \, V_{\rm Coul} \frac{\delta g(r)}{\delta n} \delta n.$$

From this we can read the derivative as

$$\frac{\partial \mathcal{E}^{\rm mon}}{\partial n} = \frac{\partial t_0}{\partial n} + \int \mathrm{d}\vec{r} \, [g(r) - 1] V_{\rm Coul} + n \int \mathrm{d}\vec{r} \, V_{\rm Coul} \frac{\delta g(r)}{\delta n}.$$

The compressibility will then be proportional to

$$\frac{\partial^2 \mathcal{E}^{\rm mon}}{\partial n^2} = \frac{\partial^2 t_0}{\partial n^2} + 2 \int \mathrm{d}\vec{r} \, V_{\rm Coul} \frac{\delta g(r)}{\delta n} + n \int \mathrm{d}\vec{r} \, V_{\rm Coul} \frac{\delta (\delta g(r)/\delta n)}{\delta n}.$$

Deriving the functional dependence of $g(r)$ on n in a closed form is an almost impossible task. Extensive studies of conventional two-dimensional electron systems have indicated that $g(r)$ varies only slightly as a function of density [229], except at very low densities where it starts to develop a prominent peak as a precursor to Wigner crystallization [235]. Since in graphene the Wigner crystallization is not a possibility (in the absence of an external magnetic field) [236], and no other phase transitions expected at the density range of interest, we expect the variation $\delta g(r)/\delta n$ to vanish or to be negligibly small. Alternatively, we could consider a slightly less stringent condition $\int \mathrm{d}\vec{r} \, V_{\rm Coul} \frac{\delta g(r)}{\delta n} = 0$, which implies that the interaction energy

depends linearly on the density of Dirac electrons. The compressibility is then described entirely by the kinetic energy

$$\kappa^{-1} = \frac{\partial^2 \mathcal{E}^{\mathrm{mon}}}{\partial n^2} = \frac{\partial^2 t_0}{\partial n^2},$$

in accordance with the experimental observation [213]. In arriving at this striking result, there are two basic properties of monolayer graphene that play crucial roles: the linear energy dispersion and chirality of massless Dirac electrons [227].

This immediately invites the question: what happens in bilayer graphene, where the low-energy charge carriers behave as massive chiral fermions and as such the Hamiltonian is quadratic in momentum operators near the charge neutrality point?

4.1.2. *Bilayer graphene*

In bilayer graphene, as discussed above, there are four atoms per unit cell, so in principle the basis employed in the tight binding model should be doubled in size. However, a low-energy effective theory is employed which considers only the atomic sites which are not involved in the inter-layer dimer bond, and so reduce the basis to only eight components. The authors of [227] used the effective two band model detailed in Section 3.2.3 and obtained from the Hamiltonian corresponding to the first term of Equation (42). The wave functions associated with this Hamiltonian are

$$\psi_\alpha(\vec{r}) = \frac{\mathrm{e}^{\mathrm{i}\vec{q}_\alpha\cdot\vec{r}}}{\sqrt{2\mathcal{A}}}\begin{pmatrix} -\mathrm{e}^{-2\mathrm{i}\theta_\alpha} \\ 1 \end{pmatrix}.$$

With these basis states, an intermediate expression for the kinetic energy looks as follows:

$$\begin{aligned} T^{\mathrm{bi}} = {} & \frac{1}{2}(\epsilon_\alpha + \epsilon_\beta) \\ & - \int \mathrm{d}\vec{r}_1 \mathrm{d}\vec{r}_2 \, \frac{\hbar^2}{4m} F \mathrm{e}^{-\mathrm{i}Q} \Big\{ \mathrm{i}q_\beta \Big(\big[\cos\theta_\beta + \cos(2\theta_\alpha - \theta_\beta)\big] \frac{\partial F}{\partial x_1} \\ & + \big[\sin\theta_\beta + \sin(2\theta_\alpha - \theta_\beta)\big] \frac{\partial F}{\partial y_1} \Big) + \mathrm{i}q_\alpha \Big(\big[\cos\theta_\alpha + \cos(\theta_\alpha - 2\theta_\beta)\big] \frac{\partial F}{\partial x_2} \\ & + \big[\sin\theta_\alpha - \sin(\theta_\alpha - 2\theta_\beta)\big] \frac{\partial F}{\partial y_2} \Big) \Big\} \\ & - \int \mathrm{d}\vec{r}_1 \mathrm{d}\vec{r}_2 \, \frac{\hbar^2}{4m} F \mathrm{e}^{\mathrm{i}Q} \Big\{ \mathrm{i}q_\alpha \Big(\big[\cos\theta_\alpha + \cos(\theta_\alpha - 2\theta_\beta)\big] \frac{\partial F}{\partial x_1} \\ & + \big[\sin\theta_\alpha - \sin(\theta_\alpha - 2\theta_\beta)\big] \frac{\partial F}{\partial y_1} \Big) + \mathrm{i}q_\beta \Big(\big[\cos\theta_\beta + \cos(2\theta_\alpha - \theta_\beta)\big] \frac{\partial F}{\partial x_2} \\ & + \big[\sin\theta_\beta + \sin(2\theta_\alpha - \theta_\beta)\big] \frac{\partial F}{\partial y_2} \Big) \Big\}, \end{aligned}$$

where terms containing second derivatives of F which are identically zero on integration, and those which trivially sum to zero are already excluded. The integrals

of terms with single derivatives of F are finite:

$$\int \mathrm{d}\vec{r}_1\,\mathrm{d}\vec{r}_2\,\mathrm{e}^{\pm \mathrm{i}Q}F\frac{\partial F}{\partial x_1} = \mp \mathrm{i}\left(q_{\beta x} - q_{\alpha x}\right)\frac{\mathcal{A}^2\tilde{F}^2}{8} = -\int \mathrm{d}\vec{r}_1\,\mathrm{d}\vec{r}_2\,\mathrm{e}^{\pm \mathrm{i}Q}F\frac{\partial F}{\partial x_2}$$

and similarly for terms containing derivatives with respect to y. After some lengthy algebra, one gets [227]

$$T^{\mathrm{bi}} = \frac{1}{2}(\epsilon_\alpha + \epsilon_\beta) + \frac{\hbar^2}{4m}\frac{\mathcal{A}^2\tilde{F}^2}{2}\cos\left(\theta_\alpha - \theta_\beta\right)\left\{\left(q_\alpha^2 + q_\beta^2\right)\cos\left(\theta_\alpha - \theta_\beta\right) - 2q_\alpha q_\beta\right\}. \quad (51)$$

When compared with the kinetic energy in monolayer graphene (Equation (49)), the non-cancellation exhibited in Equation (51) is a feature of the sublattice structure of the electronic wave function in bilayer graphene, resulting from the quadratic nature of the low-energy dispersion relation. On evaluation of the remaining integrals and after some elementary algebra, the energy functional is found to be

$$\mathcal{E}^{\mathrm{bi}} = t_0 + \langle \mathcal{V} \rangle + \frac{\hbar^2}{8m}\frac{\tilde{F}^2}{||\Psi||^2}\cos(\theta_\alpha - \theta_\beta)\left[(q_\alpha^2 + q_\beta^2)\cos(\theta_\alpha - \theta_\beta) - 2q_\alpha q_\beta\right], \quad (52)$$

where $\tilde{F}$ is the Fourier transform of the correlation function. Comparing the case of monolayer graphene, Equation (50), one can easily see that there is a non-zero contribution of electron correlations to the kinetic energy in the above functional (Equation (52)), and therefore taking the derivatives with respect to n yield a compressibility which depends non-trivially on them. It is clear that this additional term will also be present in the many-body energy, as its integral over momentum is manifestly finite. It is also expected that for bilayer graphene where the excess electron density is high enough that the Fermi energy is in the energy range where the linearity of the spectrum is restored, the effect of the correlations in the energy functional will again be suppressed. Quantitative computation of this term requires precise knowledge of the radial dependence of F, and the relation between $F(r)$ and $g(r)$ (where several choices of approximate schemes are available in the literature e.g. [237]). Most importantly, however, an experimental observation of a shift in compressibility from the pure kinetic energy contribution (unlike what was observed for monolayer graphene) would provide a way to directly determine the strength of electron correlations in that system.

4.2. *Plasmon dispersion in graphene*

In this section, we discuss the Coulomb screening properties and collective excitations in monolayer and bilayer graphene. We focus on the work of Wang and Chakraborty [238,239], although some parts of their results were previously calculated by Wunsch *et al*. [240]. Later papers which contain analytical results for the plasmon spectrum and other dynamical properties of graphene include references [208,209,241–246].

4.2.1. *Monolayer graphene*

In the pseudospin space, the zero-magnetic-field Hamiltonian of a spin-up electron which experiences a non-negligable SOI that is parameterized by a momentum

$\vec{p} = \hbar\vec{k}$ measured from the K point is [238,247,248] $\mathcal{H} = v_F\vec{p}\cdot\vec{\sigma} + \Delta_{so}\sigma_z$ with $\vec{\sigma} = (\sigma_x, \sigma_y, \sigma_z)$ the Pauli matrices. Here Δ_{so} is the strength of the SOI[9]. The eigenstates of the Schrödinger equation are readily obtained as

$$\Psi^{\lambda}_{\vec{k}}(\vec{r}) = e^{i\vec{k}\cdot\vec{r}}\begin{pmatrix} 1 + \sin(\alpha_{\vec{k}} + \lambda\pi/2) \\ -e^{i\phi_{\vec{k}}}\cos(\alpha_{\vec{k}} + \lambda\pi/2)\end{pmatrix},$$

with energy $E^{\lambda}_{\vec{k}} = \lambda\sqrt{\Delta^2_{so} + \hbar^2 v_F^2 k^2}$ for $\lambda = +1$ denoting the conduction band and $\lambda = -1$ the valance band. Here $\tan\phi_k = k_y/k_x$, $\tan\alpha_k = \hbar v_F k/\Delta_{so}$, and $k = \sqrt{k_x^2 + k_y^2}$.

The RPA Coulomb interaction in the Fourier space $U(q,\omega)$ obeys the equation [250,251]

$$U(q,\omega) = v_0 + v_0\hat{\Pi}_0(q,\omega)U(q,\omega) \tag{53}$$

with the electron–hole propagator

$$\hat{\Pi}_0(q,\omega) = 4\sum_{\lambda,\lambda',\vec{k}} |g^{\lambda,\lambda'}_{\vec{k}}(\vec{q})|^2 \frac{f[E^{\lambda'}_{\vec{k}+\vec{q}}] - f[E^{\lambda}_{\vec{k}}]}{\omega + E^{\lambda'}_{\vec{k}+\vec{q}} - E^{\lambda}_{\vec{k}} + i\delta}, \tag{54}$$

as illustrated by the Feynmann diagram in Figure 50. Here $v_0 = e^2/(2\epsilon_0\epsilon_i q)$ is the two-dimensional Coulomb interaction (in Fourier space) with the high-frequency dielectric constant [252] $\epsilon_i = 1$ and $g^{\lambda,\lambda'}_{\vec{k}}(\vec{q})$ is the interaction vertex.

The factor of four in Equation (54) comes from combined degeneracy of the spin (two-fold) and valley (also two-fold) quantum numbers; the vertex factor reads

$$|g^{\lambda,\lambda'}_{\vec{k}}(\vec{q})|^2 = \frac{1 + \lambda\lambda'\cos\alpha_{\vec{k}+\vec{q}}\cos\alpha_{\vec{k}} + \lambda\lambda'\sin\alpha_{\vec{k}+\vec{q}}\sin\alpha_{\vec{k}}(k + q\cos\theta)}{2|\vec{k}+\vec{q}|},$$

with θ being the angle between $\vec{k}$ and $\vec{q}$. Since the chiral property of the system prohibits the intra-band backward scattering at $\vec{q} = 2\vec{k}$ and the inter-band vertical transition at $\vec{q} = 0$ under the Coulomb interaction, we have $|g^{\lambda,-\lambda}_{\vec{k}}(0)|^2 = |g^{\lambda,\lambda}_{\vec{k}}(2\vec{k})|^2 = 0$. The collective excitation spectrum is obtained by finding the zeros of the real part of the dielectric function $\hat{\epsilon}(q,\omega) = 1 - v_0(q)\hat{\Pi}_0(q,\omega)$.

In the presence of the SOI, an energy gap opens between the conduction and valence bands and the semimetal electronic system is converted into a narrow gap semiconductor system. At the same time, a gap is opened between its intraband single-particle continuum $\omega \le \omega_L \equiv \hbar v_F q$ and its interband single-particle continuum $\omega \ge \omega_H \equiv 2\sqrt{\Delta^2_{so} + \hbar^2 v_F^2 q^2/4}$. However, the system differs from a normal narrow gap semiconductor due to its peculiar chiral property. Here we have chosen the magnitude of the SOI strength to be around 0.08–0.1 meV [247,253]. The result

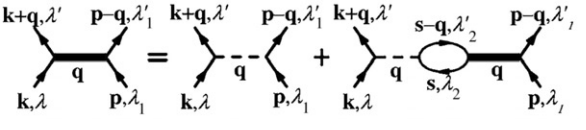

Figure 50. Diagrammatic illustration of the RPA dressed Coulomb interaction.

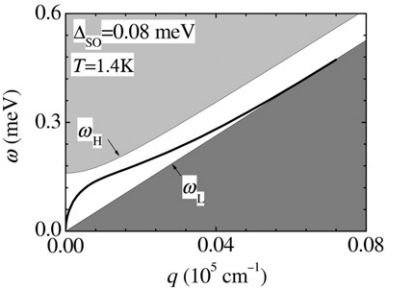

Figure 51. Plasmon spectrum (thick curve) of an electron gas in intrinsic graphene ($E_F = 0$) at temperature $T = 1.42$ K with $\Delta_{SO} = 0.08$ meV. Intra- (dark shaded) and inter- (light shaded) band single-particle continuums are also shown. ω_L and ω_H are the lower and upper borders separating the white (EHC gap) and shaded areas, respectively (see also [240]).

can be easily applied to Dirac gases with different Δ_{so} by scaling the energy and wavevector in units of Δ_{so} and $k_{so} = \Delta_{so}/(\hbar v_F)$, respectively.

At zero temperature or for $T \ll \Delta_{so}$, the intraband transition is negligible and $\epsilon_r > 0$. There is no plasmon mode in the system. With an increase in the temperature, holes appear in the valence band and electrons in the conduction band. The intraband transitions are enhanced and contribute to the electron–hole propagator of Equation (54) and a dip in ϵ_r at the intra-band electron-hole excitation continuum (EHC) edge ω_L. This dip in ϵ_r results in plasmon modes above ω_L. For $\Delta_{so} = 0$ where $\omega_H = \omega_L$, the intraband (interband) single-particle continuum occupies the lower (upper) part of the ω–q space below ω_L (above ω_L) and the plasmon mode are Landau damped. In the presence of the SOI, i.e. for $\Delta_{so} \neq 0$, a gap of width $\omega_H - \omega_L$ is opened between the intra- and interband single-particle continuum and an undamped plasmon can exist in this gap, as shown in Figure 51. This plasmon mode may perhaps be observed in experiments.

The appearance of the undamped plasmon mode in the presence of the SOI is a result of the interplay between the intra- and inter-band correlations which can be adjusted by varying the temperature of the system in experiments. To show the temperature range in which an undamped plasmon mode exists, Figure 52 shows $\epsilon_r(\omega_L)$ (dotted curve) and $\epsilon_r(\omega_H)$ (solid curve) as functions in the temperature T at $q = 0.05 \times 10^5\,\mathrm{cm}^{-1}$. For $\Delta_{so} = 0.08$ meV, an increase of the temperature from $T = 0$ leads to an increase in the ratio of the intra- to the inter-band correlation while ϵ_r in the EHC gap ($\omega_L \leq \omega \leq \omega_H$) decreases and crosses zero. There is no undamped plasmon mode when the inter-band correlation dominates at $T \leq 1.1$ K and when the intra-band correlation dominates at $T \geq 3.3$ K. In the temperature regime 1.1 K $\leq T \leq 3.3$ K or $T \approx 2\Delta_{so}$ when the intra- and inter-band correlations match, however, $\epsilon_r(\omega_L) < 0$ while $\epsilon_r(\omega_H) > 0$ and one undamped plasmon mode exists.

Therefore, the SOI converts the Dirac electronic system into a narrow gap semiconductor with chiral properties. As a result, an undamped collective excitation was found to exist in the spectral gap of the single-particle continuum and is perhaps observable in the experiments. There have been a steady flow of reports in the literature on the electronic properties of graphene. Interestingly, the SOI-dependent

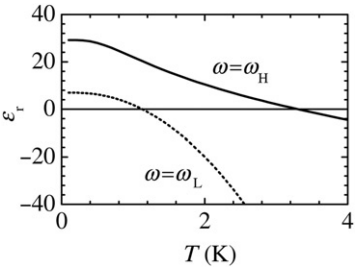

Figure 52. Temperature dependence of the real part of the dielectric function at the edges of the intra- and intersubband single-particle continuum ω_L (dotted curve) and ω_H (solid curve) at $q = 0.05 \times 10^5\,\mathrm{cm}^{-1}$.

dielectric function derived in [238] was employed by other authors to explore the possibility of Wigner crystallization in graphene [236].

After Wang and Chakraborty [238] reported their study of Coulomb screening and plasmon spectrum in monolayer graphene with zero or finite gap and doping at zero or finite temperature, a series of works have been reported on the many-body effects in graphene. Analytical results for dynamical polarization of graphene were reported within the RPA [240,241]. Instead of considering only the spin-orbit introduced energy gap, Qaiumzadeh and Asgari [242] assumed an unspecified energy gap of arbitrary width for doped monolayer graphene and studied the corresponding ground-state properties in the RPA. They concluded that the conductance and the charge compressibility decrease with the band gap. Almost during the same time, Pyatkovskiy [243] also derived analytically the dielectric function of gapped graphene at zero temperature and repeated the plasmon spectrum result of Wang and Chakraborty. In addition, the effect of plasmons on the energy band in graphene has been estimated and compared with the experimental result [254–256]. Hill, Mikhailov and Ziegler [246] have recently reported results on the dielectric function and plasmon dispersion based on the tight-binding band structure and take the non-Dirac effect of graphene dispersion band into account, including the anisotropy and the nonlinearity of the energy band. Those effects influence the plasmon spectrum, in terms of the anisotropic plasmon spectrum and extra plasmon mode. Coulomb screening and collective excitations spectrum in monolayer graphene using the RPA was also reported by other authors [257,258]. The magneto-optical excitations in monolayer graphene has also been investigated [259]. Finally, a THz source has been proposed based on the stimulated plasmon emission in graphene [260] and the absorption of THz electromagnetic radiation in gapped graphene has been estimated [261].

4.2.2. *Bilayer graphene*

While monolayer graphene has quasiparticles described by a chiral Dirac gas, bilayer graphene is best thought of as a chiral Fermi gas near the K points [139,140,207,262] (Section 3). Consequently, a comparison of their physical properties would offer new understanding and provide interesting predictions about the different behaviors between these two fundamental systems. Wang and Chakraborty [239] were the first

to employ the RPA to address some of the interesting properties of the Coulomb screening and the collective excitations in bilayer graphene.

In the effective-mass approximation [139,262], the electrons in the K valley are described by a Hamiltonian with a mixture of linear and quadratic terms in the wave vector k (see the first two terms of Equation (42) in Section 3.2.3). The eigenfunction of the above Hamiltonian is $\Psi_{\vec{k}}^{\lambda}(\vec{r}) = \frac{e^{i\vec{k}\cdot\vec{r}}}{\sqrt{2}}\left(ce^{i\phi_{\vec{k}}}\lambda\right)$ with the energy $E_{\vec{k}}^{\lambda} = \lambda\hbar^2 k\sqrt{k^2 - 2k_0 k\cos 3\varphi + k_0^2}/2m$ and the pseudospin angle $\lambda\phi_{\vec{k}}$. Here $\varphi = \arg(k_+)$, $\phi_{\vec{k}} = \arg(ke^{-2i\varphi} - k_0 e^{i\varphi})$ with $\arg(z)$ being the argument θ of a complex $z = |z|e^{i\theta}$, $k_0 \approx 10^8/\sqrt{3}\mathrm{m}^{-1}$ is the wave vector difference between the central pocket and any of the three 'leg' pockets in the same valley (Section 3.2.2.), and $\lambda = 1(-1)$ for the conduction (valence) band.

Just as for the case of the monolayer graphene [238] and other spin systems [251], we find that the dielectric matrix of a graphene bilayer is a unit matrix multiplied by a dielectric function

$$\hat{\varepsilon}(q,\omega) = 1 - v_q\hat{\Pi}_0(\vec{q},\omega), \tag{55}$$

with the bare Coulomb interaction $v_q = e^2/(2\varepsilon_0 q)$ and the electron–hole propagator is written explicitly in Equation (54). Near the central Dirac point at $k = 0$, the intraband backward scattering and interband vertical Coulomb scattering are forbidden and $|g_{\vec{k}}^{\lambda,-\lambda}(0)|^2 = |g_{\vec{k}}^{\lambda,\lambda}(-2\vec{k})|^2 = 0$. The same rules also hold for the three satellite Dirac points. For a large k ($k \gg k_0$), $|g_{\vec{k}}^{\lambda,-\lambda}(0)|^2 = |g_{\vec{k}}^{\lambda,-\lambda}(-2\vec{k})|^2 = 0$, but $|g_{\vec{k}}^{\lambda,\lambda}(-2\vec{k})|^2 = 1$, i.e. the intraband backward transition is allowed but both the interband backward and vertical transitions are forbidden. The above selection rules together with the energy dispersion of the carriers indicate that the electrons (holes) close to the bottom (top) of the conduction (valence) band have very different behaviors from those away from the bottom (top).

The Coulomb screening is dictated by the response of the electron liquid to a pertubation. The static dielectric function at zero temperature versus q is plotted in Figure 53(a). Its long wavelength limit is given by the properties of the four pockets around each of the Dirac points. The central point has an isotropic velocity $v_0 = \hbar k_0/(2m) = 10^5\,\mathrm{m\,s^{-1}}$ (with energy $E_0 = \hbar^2 k_0^2/2m = 3.9$ meV) while the satellite ones have the elliptic form of equi-energy lines with a minimum velocity equal to v_0 along their radial direction and a maximum of $3v_0$ along the azimuthal direction. The static dielectric constant at $q = 0$ is estimated to be $\varepsilon_s = 1 + 3e^2/(8\varepsilon_0\hbar v_0) \approx 105$. This value is much bigger than that of the monolayer graphene (4.5) [238]. This means that the long-range Coulomb interaction is much more strongly screened for the bilayer system, using a much bigger density of states near the Fermi energy in a bilayer graphene.

Another characteristic of bilayer graphene is its screening anisotropy, especially for scattering at a distance range of about 10 nm. This is shown by the difference between the solid and the dotted curves in Figure 53(a) and (b), corresponding to the directions of $\vec{q}$ pointing to any satellite from the central Dirac points ($\alpha = 0$) or connecting any two satellites ($\alpha = \pi/6$). Here α is the angle between $\vec{q}$ and the x-axis. At $q = \sqrt{3}k_0 = 10^8\,\mathrm{m}^{-1}$, the wavevector distance between any two satellite Dirac points, the anisotropy of ε_s reaches its maximum with a mismatch of 20% along the different directions. The shoulder near $q = k_0 = 0.58 \times 10^8\,\mathrm{m}^{-1}$ in the solid curve

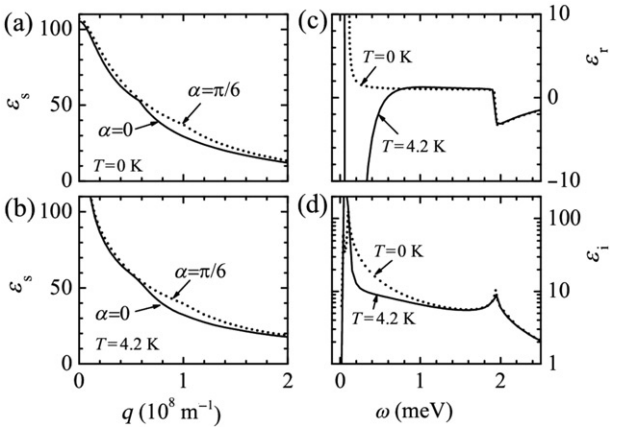

Figure 53. (a) The static dielectric function ε_s versus the wavevector q along the direction $\alpha=0$ (solid) and $\pi/6$ (dotted) at $T=0$. (b) The same as (a) but at $T=4.2$ K. (c) The real part of the dielectric function ε_r versus frequency ω at $T=0$ (dotted) and at $T=4.2$ K (solid). (d) The imaginary part of the dielectric function ε_i versus ω at $T=0$ (dotted) and at $T=4.2$ K (solid). In (c) and (d), $q=0.005\times10^8\,\mathrm{m}^{-1}$ and $\alpha=0$. In the limit $\omega\to\infty$, ε_r gradually approaches to one while ε_i approaches to zero.

reflects the strong scattering between the carriers in the central and the $\varphi=0$ satellite Dirac points. At a finite temperature, the energy pockets near the Dirac points are partially occupied and the intraband scattering strength is greatly enhanced. As a result, the static dielectric function near $q=0$ increases rapidly, as shown in Figure 53(b) at $T=4.2$ K. The effect of finite temperature is shown in Figure 53(c) and (d) for $q=0.005$ along $\alpha=0$, at $T=0$, 4.2 K.

For $\omega > E_0/2$, the dielectric function of bilayer graphene is similar to that of a normal Fermi gas and its temperature dependence is weak. The step of ε_r and the peak of ε_i near $\omega=E_0/2=2$ meV correspond to the single-particle excitations coupling states with vanishing group velocity and wavevectors equal to half of the vector from the central pocket to a satellite pocket. For small ω, however, the dielectric function becomes more sensitive to the temperature and shows characteristics of the Dirac gas. One sign of the Dirac gas is the lack of Coulomb screening ($\varepsilon_r\approx1$) in the energy window between 1 and 2 meV. Another sign is that a low-energy plasmon mode appears only at a finite temperature. As shown in Figure 53 (c), ε_r has no negative value for the energy $\omega < E_0/2$ at $T=0$ but evolves into a deep negative dip at a finite temperature $T=4.2$ K, when the energy pockets near the Dirac points are partially occupied. As a result, one observes a weakly Landau damped plasmon mode of dispersion $\omega\sim\sqrt{q}$ at $T=0$ and a couple at finite temperatures.

The collective excitations of the electronic liquid in bilayer graphene are also a subject of interest. Figure 54(a) shows the plasmon spectrum of intrinsic bilayer graphene ($E_F=0$). The dispersion of the weakly Landau-damped mode is indicated by the thick curve and has $\sqrt{q}$ dependence. Interestingly, the plasmon mode exists only at energy higher than $E_0/2$, i.e. double the depth of the energy pockets in the

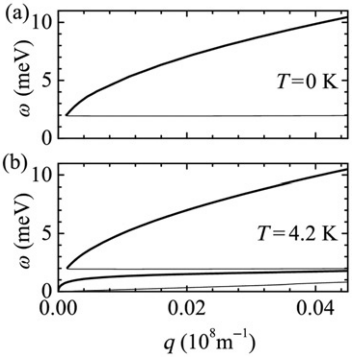

Figure 54. The plasmon spectrum of an undoped bilayer graphene at $T=0$ (a) and at $T=4.2\,\mathrm{K}$ (b). The thick curves indicate the weakly Landau damped modes while the thin curves represent the strongly damped modes.

Dirac points. At a finite temperature $T=4.2\,\mathrm{K}$, another weakly damped plasmon mode shows up at the energy lower than $E_0/2$ and also has a dispersion of $\sqrt{q}$ near $q=0$, as illustrated in Figure 54(b). The plasmon mode of higher energy that exists at $T=0$ is not sensitive to the temperature. This temperature dependence of the low- and high-energy plasmon spectra represents a marked difference between electron gases having linear (without the collective excitations) and quadratic (with the collective excitations) energy dispersion at $T=0$. The electronic states in bilayer graphene are similar to the Fermi type at high energies but revert to Dirac type at low-energy.

The carrier density of the system can be changed by doping [140]. For a typical doping density of $10^{12}\ \mathrm{cm}^{-2}$ [140,262], the Fermi energy is high enough above the bottom of the conduction band that the linear k term in the Hamiltonian can be neglected. The electrons then have quadratic dispersion but with chirality and $\phi=-2\varphi$. Near $q=0$, the plasmon dispersion in doped bilayer graphene has $\sqrt{q}$ dependence, as shown by the solid curve in Figure 55, and shares the same dispersion $\omega_p^{2D}=[n_e e^2 q/2\varepsilon_0 m]^{\frac{1}{2}}$ with a normal two-dimensional Fermi gas. To see the effect of the chirality, for comparison we plot as a dotted curve the plasmon dispersion of a normal two-dimensional Fermi gas with two valleys. The two curves overlap for the small q but separate as q increases. The maximum difference in the dispersion appears near $q=\sqrt{2}k_{\mathrm{F}}$ when $\vec{k}$ and $\vec{k}+\vec{q}$ form a right angle in the Fermi plane and the corresponding transition is forbidden in the bilayer graphene due to the chiral scattering properties.

The bilayer plasmon frequency is smaller than that of the monolayer because the dielectric properties of the monolayer are weaker. Hwang and Das Sarma [208] derived analytical expression of static dielectric function for bilayer graphene with moderate doping when the linear Hamiltonian term can be neglected. With the analytical expression, they could estimate the screened static Coulomb potential and show the Kohn anomaly near $q=k_{\mathrm{F}}/2$, the Friedel oscillation and the form of RKKY interaction in bilayer graphene. See Section 3.5 for a description of this work.

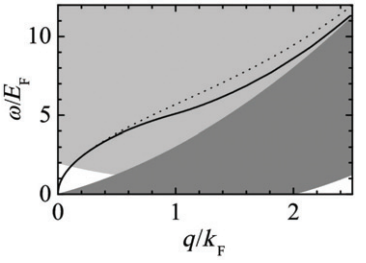

Figure 55. The plasmon spectrum of a doped bilayer graphene (solid curve) with a typical carrier density of $10^{12}\,\mathrm{cm}^{-2}$. Correspondingly, $E_F = 36.3\,\mathrm{meV}$ and $k_F = 1.77 \times 10^8\,\mathrm{m}^{-1}$. The plasmon spectrum in the same system but without chirality is plotted as a dotted curve for comparison. Intra- (dark shaded) and inter- (light shaded) band single-particle continuums are also shown.

The magneto-plasmons in bilayer graphene were considered in a self-consistent analytical framework by Tahir *et al*. [263]. They derived expressions for the plasmon frequency, and compared their results to those for monolayer graphene and traditional 2DESs. The light effective mass of the electrons in the bilayer, and the relatively weak dielectric properties of graphene ensures that the plasmon frequency is approximately two times higher than that of, for example, GaAs–AlGaAs heterojunctions. The magnetoplasmon and Weiss oscillation has been studied in mono- and bilayer graphene [264,265]. The Boltzman equation has been used to study the electronic transport in bilayer graphene [266]. Then the effects of site dilution disorder on the electronic properties, such as self-energies, the density of states, the spectral functions and both DC and AC transport properties, in graphene multilayers have also been studied [267].

Theoretical approaches described in this section were recently employed by Wang and Chakraborty to investigate the Coulomb screening and plasmon spectrum in a bilayer graphene under a perpendicular electric bias [268]. The potential bias applied between the two graphene layers opens a gap in the single-particle energy spectrum and makes the semimetal bilayer graphene into a semiconductor. As a result, the dielectric function for the Coulomb interaction and the propagator function were found to be modified significantly [268]. The potential bias also opens a gap in the single-particle excitation spectrum and softens the collective modes. This may result in undamped collective modes that are observable in experiments. Experimental observation of plasmon modes with long lifetime might prove to be beneficial for future device applications.

4.3. *Graphene in a strong electromagnetic field*

Graphene also displays unique and intriguing properties when it is irradiated by strong electromagnetic fields (EMFs), such as laser light. Floquet theory (the temporal analogue of Bloch theory) has been applied [224,269] to determine the quasienergy spectrum and dynamical density of states, in this situation.

The time-periodic EMF is represented by a vector potential, and the minimal coupling substitution made in the Hamiltonian. The Floquet theory is then applied,

so that the overall wave function of Floquet state α is written as $\Psi_\alpha(t) = e^{-i\varepsilon_\alpha t}\Phi_\alpha(t)$ where $\Phi_\alpha(t+T) = \Phi_\alpha(t)$, with $T = 2\pi/\Omega$. The Floquet Hamiltonian may be diagonalized numerically to produce the spectrum of quasienergies ε_α and the wave functions $\Phi_\alpha(t)$, which may then be used to calculate physical quantities such as the density of states, or the electronic current. As an example, Oka *et al.* [269] showed that an intense, circularly polarized EMF parametrized by frequency Ω and intensity F generates spectral gaps at $\omega = \pm\Omega/2$, and at the Dirac point. The gap at the Dirac point is initially quadratic in the intensity: $2\kappa \sim 2A^2/\Omega$, but takes the asymptotic behavior $2\kappa \sim 2A - \Omega$. Here $A = F/\Omega$, where F is the field strength (intensity). This gap exists both in bulk monolayer graphene, and in graphene nanoribbons. The authors then use the Keldysh approach to calculate the current through a finite-sized, irradiated monolayer graphene sample and find that a dc Hall current in induced in the ribbon.

Fistul *et al.* [270] have shown that an intense EMF may mitigate the Klein effect in a *n-p* junction and allow electrostatic confinement of electrons. It does this by creating a dynamical band gap, which forbids the tunnelling of quasiparticles through the potential barrier via hole states, as in the Klein effect. Instead, electrons may only tunnel via interband processes which are strongly suppressed. The size of the gap is dependent on the intensity and frequency of the radiation, so the authors claim that structures such as QDs or *n–p–n* transistors may be engineered by this technique. Photon-assisted tunnelling was also considered in the context of bilayer graphene by Shafranjuk [271]. López-Rodríguez and Naumis describe analytical results within the Floquet formalism [272] and Wright *et al.* [273] have shown that bilayer ribbons show enhanced optical conductivity in the terahertz and far infra-red frequency ranges.

Abergel and Chakraborty [224] considered irradiated bilayer graphene, both with and without the gap-generating bias potential. When the bilayer was unbiased, a similar picture was found to that of the monolayer, with dynamical gaps being generated at the charge-neutrality point, and at $\omega = \pm n\Omega/2$, with n an integer. These gaps are manifest in the density of states, as shown in Figure 56. In the case when there is a finite gap at zero energy (evidenced by the low density of states), the radiation may cause dynamical states to be created in the gapped region (see, e.g. the finite density of states for $\omega < 5\,\text{meV}$ in the K valley for $F = 5\,\text{kV/cm}$ in Figure 56(a)). The most fascinating observation to be made from Figure 56 is that for $U \neq 0$, the density of states is not the same in each valley, since the orientation of the circular polarization of the irradiating field couples more strongly to electrons in one valley than in the other. If the polarization of the radiation is reversed, or the direction of the bias potential U is swapped, then the strong and weak couplings are also reversed. In particular, the radiation-induced density of states in the gapped region is, in some cases, only present in one valley. For example, for $F = 1\,\text{kV cm}^{-1}$ and $U = 10\,\text{meV}$, there is finite density of states in the K valley for $\omega < U/2$, but not in the K′ valley. The authors go on to show how irradiated bilayer graphene may be used as a valley filter for an electron current. By irradiating one part of a graphene flake, and attempting to pass current through this section, electrons will only pass if there is a finite density of states through which they can propagate. Therefore, tuning the radiation so that the density of states is in one valley or the other immediately yields a valley-polarized current. This effect was demonstrated theoretically by

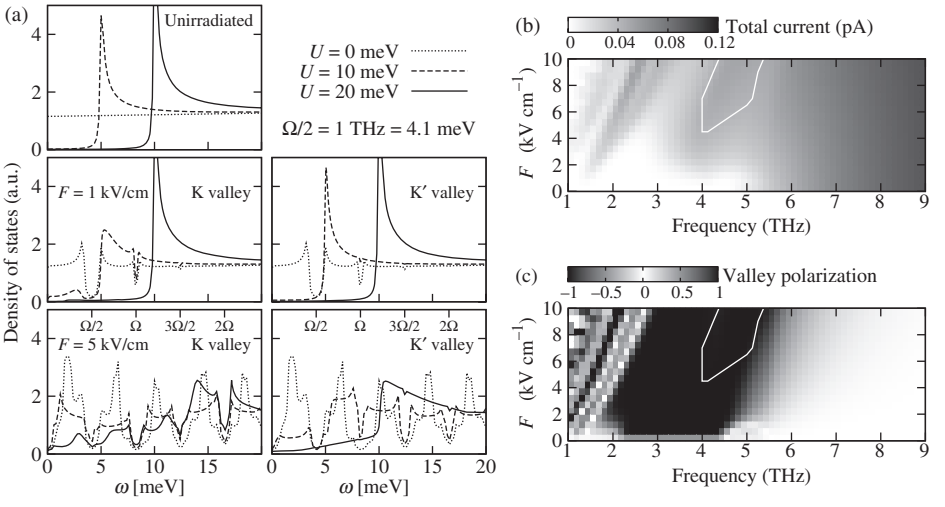

Figure 56. (a) Density of states in irradiated bilayer graphene for three field intensities and three gap sizes. (b) The total current, and (c) the valley polarization of electron transport through an irradiated bilayer graphene device. In (b) and (c), $U = 20$ meV, and the transverse (current-driving) bias is 12 meV. The white contours denote the region of simultaneous high valley polarization (>98%) and significant current flow (>0.08 pA).

computing the current through the device via a tunnelling approach. The two graphitic 'leads' are described by appropriate Hamiltonian for unirradiated bilayer graphene. The central (irradiated) region is linked to the leads via coupling Hamiltonians which assume that the momentum and energy of the electron must be conserved at the boundary. The valley component of the charge current in the right-hand (outgoing) lead is $J_\xi = -\langle \mathrm{d}N_R^\xi/\mathrm{d}t\rangle$, where N_r^ξ stand for the number operator of ξ-valley electrons in the right lead. A nonequilibrium Green's function method is used to compute the current of electrons in the ξ valley, which is

$$J_\xi = -\frac{2e}{h}\int \frac{d^2\vec{k}}{(2\pi)^2}\sum_{\alpha_\xi} \mathrm{Tr}\{\bar{\Gamma}_{\alpha_\xi}\Im\bar{G}^r(E_{\alpha_\xi})\}[f_c(E_{\alpha_\xi}) - f_R(E_{\alpha_\xi})],$$

where $f_{c,R}$ is the occupation of electrons in the central region or right-hand lead, G^r is the full retarded Green's function in the central region, Γ contains the inter-region coupling parameters, α labels the Floquet states, E is the energy of an electron in the lead and Tr denotes the trace over the matrix structure (designated by the overbar). The Green's function is calculated using the Floquet states, and includes the self energy due to the two graphitic leads.

This filter device can produce electrons in either valley, simply by reversing the polarity of the incident light, or the sign of the bias potential U. In Figure 56(b) and (c), the total current through irradiated bilayer graphene is shown, along with the simultaneous valley polarization. The area where the polarization is greater than 98%, and the current is greater than 0.08 pA is shown by the white contour.

5. Zero-field transport in graphene

Transport properties in graphene and bilayer graphene are among the most exciting observations in these new materials. What is so special about them? First of all, graphene is a genuine two-dimensional electronic system. Second, it is a semimetal at the charge neutrality point and a metal away from the charge neutrality point. This means that the Fermi surface, responsible for transport at low temperatures, consists either of two (slightly deformed) circles away from the charge neutrality point which shrink to two Dirac points exactly at charge neutrality. Moreover, the fact that graphene has two bands, touching each other only at the two Dirac points (Section 1), provides intra- and interband scattering, where the latter leads to a number of interesting features such as Klein tunnelling and a constant optical conductivity.

Transport processes can be distinguished by the type of scattering of the (quasi) electrons in the material. First of all, the electrons are scattered by the honeycomb lattice, which leads to the formation of Bloch states if the lattice is perfectly periodic. This case is also known as ballistic transport, in which the boundary conditions play a crucial role. Then there can be scattering by non-periodic structures (impurities, lattice defects and lattice deformations). This leads to diffusion of the electrons, under certain conditions also to Anderson localization. And finally, there is scattering between the electrons themselves due to Coulomb interaction and electron–phonon interaction.

The basis for calculating quantum transport properties is either the linear response theory (Kubo formalism) or the evaluation of transmission coefficients (Landauer–Büttiker formalism). Both approaches have been used frequently for graphene and gave the same results for comparable quantities. In the following, we will employ the Kubo formalism because it provides more flexibility for calculating general physical properties such as thermal effects and optical conductivities. Away from the neutrality point a classical (Boltzmann) approach was successful [274–276] and will be discussed briefly.

5.1. *Basic experimental facts*

Already the first experiments on graphene by Novoselov *et al.* [17] and Zhang *et al.* [85] revealed very characteristic transport properties in graphene. Graphene as well as a stack of two graphene sheets (i.e. a graphene bilayer) are semimetals with remarkably good conducting properties [1,17,85]. These materials have been experimentally realized with external gates, which allow a continuous change of charge carriers.

Besides the quantum Hall effect (Section 2), it was found that the longitudinal conductivity changes linearly as a function of gate voltage V_g with a negative slope for holes and a positive slope for electrons. There is a minimal conductivity $\sigma_{\min}$ near the charge neutrality point (cf. Figure 57). The latter has attracted some attention because its value seems to be very robust in terms of sample quality and temperature [1,27,277,278]. More recent experiments by Du *et al.* [26] on suspended graphene, however, indicated that below $T \approx 150\,\mathrm{K}$ the minimal conductivity decreases linearly with decreasing T and reaches the extrapolated value $\sigma_{\min} \approx 2e^2/h$ at $T = 0$. A similar result was found by Danneau *et al.* [279]. This clearly

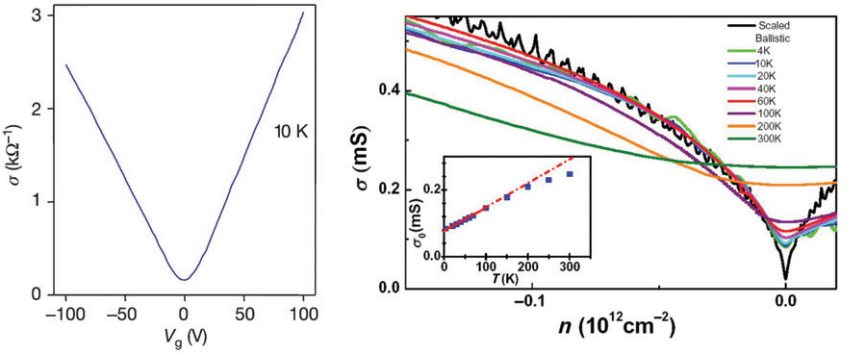

Figure 57. Measured conductivities in graphene. The linear behavior of the conductivity as a function of the gate voltage is shown for graphene on a substrate at fixed temperature $T = 10$ K (left panel) (Reprinted figure with permission from K.S. Novoselov *et al.*, Nature, 438, p. 197, 2005 [17]. Copyright © (2005) Nature Publishing Group.) and for suspended graphene at several temperatures (right panel) (Reprinted figure with permission from X. Du *et al.*, Nature Nanotechnology, 3, p. 491, 2008 [26]. Copyright © (2008) Nature Publishing Group). The inset on the right panel shows the behavior of the minimal conductivity.

indicates that the main mechanism of transport in graphene at the NP is diffusion, possibly with a very large mean-free path. Away from the NP the linear behavior has not always been observed but also a sublinear behavior. One possible reason is that the linear behavior is due to long-range scattering by charged impurities, which may not be present in suspended graphene [26].

Role of disorder – Disorder might play an important role in the physics of graphene. First of all, a two-dimensional lattice is thermodynamically unstable. It is known that this is the origin of the strong corrugations in graphene in the form of ripples. Another source of disorder are (charged) impurities in the substrate, which probably affect the transport properties substantially. Recent experiments on suspended graphene have been able to eliminate this type of disorder. Experimental evidence of strong effects of disorder comes from the observation of puddles of electrons and holes at the charge neutrality point [213]. In a recent experiment with hydrogenated graphene (graphane), disorder is added by an inhomogeneous coverage by hydrogen atoms. This leads to the formation of localized states which causes a non-metallic behavior characterized by a variable-range hopping conductivity [280].

Role of electron–electron interaction – There is no clear evidence for an effect of electron–electron interaction on transport properties. This is supported by recent theoretical findings, based on perturbative renormalization group calculations [232,281,282], that Coulomb interaction provides only a correction of 1–2% for the optical conductivity [283]. This is in good agreement with the experiments on the optical transparency of graphene [146,284].

Role of electron–phonon interaction – Although there is a remarkable electron–phonon interaction [217,285,286] in graphene, its effect on transport properties has not been investigated in detail. Some experimental findings of a gap opening was associated with electron–phonon interaction [287] but in most samples the conductivity is explained by non-interacting particles. The optical conductivity might be affected by the electron–phonon interaction of gated graphene before

interband scattering can dominate transport (i.e. when the frequency ω is less than $E_F/\hbar$) [284].

5.2. *Low-energy approximation and random fluctuations*

The linear approximation of the tight-binding model for monolayer graphene was introduced in Section 1.2. Here we focus on the low-energy properties near the nodes of neutral graphene, taking into account also random scattering caused by ripples and impurities. Moreover, a random gap can appear. The reason in the case of monolayer graphene is that fluctuations appear in the coverage of the monolayer graphene by additional non-carbon atoms [280,288]. In the case of bilayer graphene with a dual gate [140,185] the random gap is caused by the fact that the graphene sheets are not planar but create ripples [24,289,290]. As a result, electrons experience a randomly varying gap along each graphene sheet.

The two bands in monolayer graphene and the two low-energy bands in bilayer graphene represent a spinor-1/2 wave function. This allows us to expand the corresponding Hamiltonians in terms of Pauli matrices σ_j as

$$\mathcal{H} = h_1\sigma_1 + h_2\sigma_2 + \sum_{j=0}^{3} v_j\sigma_j. \tag{56}$$

Near each node the coefficients h_j read in low-energy approximation [291]

$$h_j = \mathrm{i}\nabla_j \quad \text{(monolayer graphene)}, \tag{57a}$$

$$h_1 = \nabla_1^2 - \nabla_2^2, \quad h_2 = 2\nabla_1\nabla_2 \quad \text{(bilayer graphene)}, \tag{57b}$$

where (∇_1, ∇_2) is the 2D gradient, v_1 is a random scalar potential, $v_{2,3}$ the two components of a random vector potential and v_3 a random gap. This is a gradient expansion of the monolayer graphene and bilayer graphene tight-binding Hamiltonians around the nodes K and K′.

It is assumed here that randomness scatters only at small momentum such that intervalley scattering, which requires a large momentum at least near the nodes [292], is not relevant and can be treated as a perturbation. Then each valley contributes separately to the density of states and to the conductivity, and the contribution of the two valleys is additive. This allows us to consider the low-energy Hamiltonian in Equations (56), (57) for each valley separately, even in the presence of randomness. Within this approximation the gap term $v_3 \equiv m$ is a random variable with mean value $\langle m_r\rangle = \bar{m}$ and variance $\langle (m_r - \bar{m})(m_{r'} - \bar{m})\rangle = g\delta_{r,r'}$. The following analytic calculations will be based entirely on the Hamiltonian of Equations (56) and (57). In particular, the average Hamiltonian $\langle\mathcal{H}\rangle$ can be diagonalized by Fourier transformation and is

$$\langle\mathcal{H}\rangle = p_1\sigma_1 + p_2\sigma_2 + \bar{m}\sigma_3 \tag{58}$$

for monolayer graphene with eigenvalues $E_p = \pm\sqrt{\bar{m}^2 + p^2}$. For bilayer graphene, the average Hamiltonian is

$$\langle\mathcal{H}\rangle_m = (p_1^2 - p_2^2)\sigma_1 + 2p_1p_2\sigma_2 + \bar{m}\sigma_3, \tag{59}$$

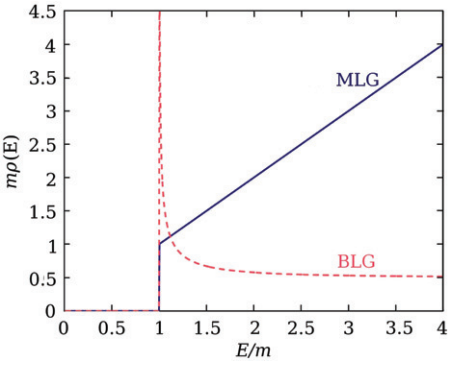

Figure 58. Density of states for monolayer graphene and bilayer graphene with a uniform gap (from [293]). Bilayer graphene has a singularity at the gap edge.

with eigenvalues $E_k = \pm\sqrt{\bar{m}^2 + p^4}$. In order to apply results from these calculations to monolayer graphene or bilayer graphene we must include a degeneracy factor $\gamma = 4$, referring to the two valleys K and K′ and the two-fold spin degeneracy of the electrons.

5.2.1. *Density of states*

Transport properties at temperature $T = 0$ are connected to the density of states $\rho(E_F)$ at the Fermi level E_F and the diffusion coefficient D through the Einstein relation for the conductivity:

$$\sigma(\omega = 0) \propto D\rho(E_F). \tag{60}$$

In the absence of disorder, the density of states of 2D Dirac fermions opens a gap, as soon as a nonzero term m appears in the Hamiltonian of Equation (56), since the low-energy dispersion is $E_p = \pm\sqrt{m^2 + p^2}$ for monolayer graphene and $E_p = \pm\sqrt{m^2 + p^4}$ for bilayer graphene (cf Figure 58). At low energies, the density of states of monolayer graphene is

$$\rho(E) = |E|\Theta(|E| - m), \tag{61}$$

where $\Theta(x)$ is the Heaviside function. For bilayer graphene the density of states is

$$\rho(E) = \frac{|E|}{2\sqrt{E^2 - m^2}}\Theta(|E| - m). \tag{62}$$

The density of states for both cases are shown in Figure 58. Random fluctuations of m can fill the gap with states by band broadening and by the development of Lifshitz tails, as shown in Figure 59.

5.3. *Theory of transport*

Transport properties, such as electric and thermal conductivities, can be calculated within either the classical Boltzmann or within the Kubo formalism. The former is

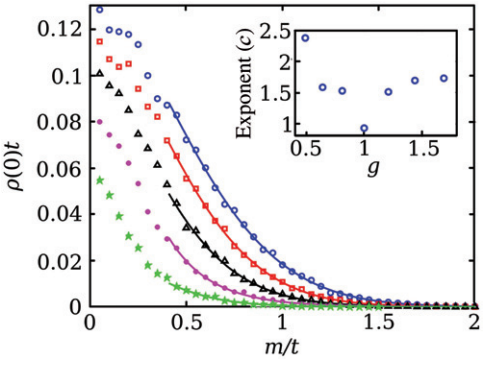

Figure 59. The density of states calculated numerically at the neutrality point for Gaussian random gap for a 200×200 honeycomb lattice for $g = 0.9^2$, 1, 1.1^2, 1.2^2 and 1.3^2 from bottom to top after 400 averages. The symbols denote the numerical data, solid lines are fits using $a\exp(-bm^c)$. The inset shows the obtained exponents, c, as a function of g, which is close to 1.5 (from [293]).

very successful for providing results away from the nodes. At the nodes quantum effects are crucial, so the Boltzmann approach fails and the Kubo formalism must be employed. An alternative to the Kubo formalism is the Landauer formalism. Both formalisms, however, lead to similar results [294]. Therefore, we will restrict the subsequent study on the Kubo formalism after a brief discussion of the Boltzmann approach.

5.3.1. *Boltzmann approach*

From the classical Boltzmann theory, where quantum effects are included by choosing a Fermi distribution for the otherwise classical electrons [229], we get for the conductivity the expression

$$\sigma = \frac{1}{2} e^2 v_F^2 \rho(E_F)\tau, \tag{63}$$

where τ is the scattering time and v_F the Fermi velocity. This relation is very similar to the Einstein relation of Equation (60). In the case of Dirac fermions ($\mathcal{H} = v_F \vec{p}\cdot\vec{\sigma}$), where the density of states is linear in E_F, we obtain

$$\sigma = 2\frac{e^2}{h}\frac{E_F\tau}{\hbar}. \tag{64}$$

The scattering time τ is determined by the distribution of random scatterers. Thus a major problem of calculating transport properties is to evaluate τ, and one possible way to do that is provided by the Boltzmann approach. The latter, based on the classical Boltzmann equation, has been a very successful concept for the discussion of transport in solid-state physics. It is more difficult to apply in graphene, however, as we will discuss next.

When τ is roughly a constant with respect to E_F, as in normal metals, the conductivity in Equation (64) would change linearly with E_F. The latter, on the other hand, is related to the density of charge carriers n as $E_F \propto \sqrt{n}$, as a consequence of the linear density of states:

$$n \propto \int_0^{E_F} \rho(E)\mathrm{d}E \approx \int_0^{E_F} E\,\mathrm{d}E = E_F^2/2.$$

Therefore, σ would change with $\sqrt{n}$ for monolayer graphene. This is not in agreement with experimental observations on gated graphene on a substrate, where it was found that σ changes linearly with n [17]. For bilayer graphene the density of states is constant near the nodes, which is a consequence of the parabolic dispersion. Then we have $n \propto E_F$, and a constant τ leads to a linear behavior in gated bilayer graphene, in agreement with the experimental observations [27]. From this point of view, bilayer graphene has a more conventional transport behavior than monolayer graphene.

To get a linear behavior also for monolayer graphene, the assumption of a constant τ must be replaced by a density-dependent τ that changes linearly with E_F: $\tau \sim k_F$. Such a behavior was obtained from the Born approximation of τ by assuming $V \sim \hbar v\pi/2k_F$ [98]. However, two problems remain within this result: one is the vanishing minimal conductivity, in contrast to the experimental observation of a minimal conductivity at the neutrality points [17]. The other is the absence of a finite offset (i.e. the linear conductivity curves of the holes and the electrons do not meet at $E_F = 0$). This behavior was observed in the experimental curves [278].

At the nodes the Fermi surface are just points and the density of states of monolayer graphene vanishes (i.e. there are no states at the Fermi energy). This implies that a statistical concept, which uses the distribution of charges, may experience some difficulties. Nevertheless, the Boltzmann approach can be applied away from the Dirac point and then the Dirac point is approached at the end. Perturbation theory with short-range scatterers gives for the scattering time [274–276]

$$\tau \propto k_F^{-1} \sim \infty. \tag{65}$$

According to Equation (64), including the Dirac dispersion $E_F \propto k_F$, this leads to a constant nonzero conductivity. Thus, the Boltzmann approach gives us a nonzero minimal conductivity when we consider short-range scatterers. Unfortunately, a divergent scattering time at the Dirac point does not describe a realistic situation because quasiparticles are scattered, e.g. by the ripples or charge inhomogeneities. Moreover, the conductivity is constant also away from the nodes $E_F = 0$ because the wavevectors k_F always cancel each other. Unfortunately, this is again in disagreement with the linearly increasing conductivity of the experiment [17].

In conclusion, the classical Boltzmann approach describes the transport properties qualitatively correct. However, it needs two different types of scattering to obtain the conductivity near the Dirac point and away from the Dirac point properly. The divergent scattering time at the Dirac point cannot be correct though, at least for strong disorder. The subsequent discussion focuses on a more microscopic approach, based on the Kubo formula for linear response to an external

electric field, where we start from the Hamiltonian in Equation (56). This will allow us to recover the Einstein relation Equation (60) with a disorder dependent diffusion coefficient D, a non-divergent scattering time and the robustness of the minimal conductivity.

5.3.2. *Kubo formalism*

A quantum approach to transport starts from a Hamiltonian $\mathcal{H}$ (here for independent electrons) and the corresponding current operator

$$j_k = -\mathrm{i}e[\mathcal{H}, r_k],$$

where r_k is a component of the position operator of the electron. The average current, induced by a weak external electric field E, is obtained in terms of linear response as Ohm's law

$$\langle j_k \rangle = \sigma_{kl} E_l,$$

with conductivity σ_{kl}. The general form of the conductivity in the Kubo formalism can be expressed as a product of one-particle Green's functions $G(z) = (\mathcal{H} + z)^{-1}$ at different energies z [295]. In the following, we exclude an external magnetic field. This leads to a vanishing Hall conductivity $\sigma_{kl} = 0$ for $k \neq l$. Following the notation of [296], there are two contributions to the real part of the longitudinal conductivity as $\sigma = \sigma^I + \sigma^{II}$ with

$$\sigma^I_{kk}(\omega) = -\frac{e^2}{2h}\omega \int \sum_r (r_k - r'_k)^2 \times \mathrm{Re}\left\{\left\langle \mathrm{Tr}_2\left[G_{rr'}\left(\frac{1}{2}\omega - \epsilon - \mathrm{i}\delta\right) G_{r'r}\left(-\frac{1}{2}\omega - \epsilon - \mathrm{i}\delta\right)\right]\right\rangle\right\} \kappa_\beta(\epsilon)\mathrm{d}\epsilon$$

and

$$\sigma^{II}_{kk}(\omega) = \frac{e^2}{2h}\omega \int \sum_r (r_k - r'_k)^2 \times \mathrm{Re}\left\{\left\langle \mathrm{Tr}_2\left[G_{rr'}\left(\frac{1}{2}\omega - \epsilon - \mathrm{i}\delta\right) G_{r'r}\left(-\frac{1}{2}\omega - \epsilon + \mathrm{i}\delta\right)\right]\right\rangle\right\} \kappa_\beta(\epsilon)\mathrm{d}\epsilon$$

with

$$\kappa_\beta(\epsilon) = f_\beta(\epsilon + \omega/2) - f_\beta(\epsilon - \omega/2)$$

and with the Fermi distribution function $f_\beta(x) = (1 + e^{\beta(x-\mu)})^{-1}$ at temperature $T = 1/k_B\beta$. The brackets $\langle \ldots \rangle$ refer to disorder average and ω is the frequency of the external electric field. The spinor structure of monolayer graphene and bilayer graphene is taken into account by the trace Tr_2 over 2×2 matrices.

The expressions of the conductivity are rather complicated which make them difficult to handle. Therefore, for practical calculations it is useful to study certain limits and to apply approximations.

DC conductivity: the standard approach to the DC conductivity (i.e. $\omega \to 0$) is to neglect σ^I, since for this expression the poles of the Green's functions are in the same half plane. Therefore, any amount of disorder will lead to an exponential decaying Green's functions. Then the summation over the lattice sites r is finite and the prefactor ω gives a vanishing DC limit $\omega \to 0$. This allows us to write

$$\sigma_{kk} \approx \sigma_{kk}^{II} = \frac{e^2}{h}\frac{\omega}{2}\int C'(\epsilon,\omega)\kappa_\beta(\epsilon)\mathrm{d}\epsilon, \tag{66}$$

where $C'(\varepsilon, \omega)$ is the real part of

$$C(\epsilon,\omega) = \lim_{\delta\to 0}\sum_r r_k^2\langle \mathrm{Tr}_2[G(r,0;\epsilon-\omega/2-\mathrm{i}\delta)G(r,0;\epsilon+\omega/2+\mathrm{i}\delta)]\rangle. \tag{67}$$

A substantial simplification is possible in the zero-temperature limit $T=0$ which restricts the integration over particle energies ϵ to a small interval, given by the frequency ω:

$$\sigma_{kk} = -\frac{e^2}{h}\frac{\omega}{2}\int_{\mu-\omega/2}^{\mu+\omega/2} C'(\epsilon,\omega)\mathrm{d}\epsilon. \tag{68}$$

A further simplification comes from the approximation by pulling out the integrand at $\epsilon=\mu$:

$$\sigma_{kk} \approx -\frac{e^2}{2h}\omega^2 C'(\mu,\omega). \tag{69}$$

This expression can be directly compared with the result of the Boltzmann approach in Equation (63).

We begin with a clean sample by ignoring the disorder average in Equation (67) and introduce the pure two-particle Green's function (2PGF)

$$C_0(\mu,\omega) = \lim_{\delta\to 0}\sum_r r_k^2 \mathrm{Tr}_2[G(r,0;\mu-\omega/2-\mathrm{i}\delta)G(r,0;\mu+\omega/2+\mathrm{i}\delta)], \tag{70}$$

which is for Dirac fermions without scattering and with infinite cutoff [297]

$$C_0(\mu,\omega) = -\frac{1}{8\omega\pi}\left[\frac{8}{\omega}+\frac{1-4\mu^2/\omega^2}{\mu}\ln\left(\frac{(1+2\mu/\omega)^2}{(1-2\mu/\omega)^2}\right)\right]. \tag{71}$$

This becomes at the Dirac point $\mu=0$ the simple expression

$$C_0(0,\omega) = -2/\pi\omega^2 \tag{72}$$

and with Equation (69) we obtain the well-known DC result [298–300] for the conductivity:

$$\sigma_{kk} = \frac{1}{\pi}\frac{e^2}{h}. \tag{73}$$

AC conductivity: for $\omega > 0$ and $T > 0$ the conductivity is a function of ω/T. Therefore, we must keep T finite for the AC conductivity. Moreover, now we must take into account also σ^I. This gives for Dirac fermions, where we ignore

the additional factor 4 that comes from the valley and from the spin degeneracy, the expression [301,302]

$$\sigma_{kk} \sim \frac{\pi}{8}\frac{e^2}{h}\frac{\sinh(\beta\omega/2)}{\cosh(\beta\omega/2)+\cosh(\beta\mu)}.$$

Here the frequency ω is restricted to the bandwidth of the underlying lattice Hamiltonian. For $\beta\mu \ll \beta\omega \sim \infty$ this becomes a frequency-independent expression [301,303–306]:

$$\sigma_{kk} \sim \frac{\pi}{8}\frac{e^2}{h}.$$

Including the spin and valley degeneracy, this agrees with the experimentally observed plateau of the optical conductivity of $\pi e^2/2h$ [146,284]. There is a correction factor due to Coulomb interaction [281–283]

$$1+\frac{c_1}{1+\alpha\ln(\lambda/\omega)/4},$$

where λ is the cut-off of the Dirac spectrum and $\alpha = e^2/\hbar v \approx 2.2$ is the effective fine structure constant. The numerical coefficient c_1 has been debated in a number papers, where the most recent value is $c_1 = 0.0125$ [283] that agrees with the previous result in [282].

Another possible correction is due to disorder, always present in realistic graphene samples in the form of ripples and impurities. Disorder leads to an effective scattering of the quasiparticles that can be characterized as a scattering rate. A conventional way of including scattering by random impurities is to introduce a scattering rate η in the form of an imaginary term $i\eta$ through the substitution $\omega \to \omega + 2i\eta$ in $C_0(\mu, \omega)$ such that

$$C(\mu,\omega) \approx C_0(\mu, \omega + 2i\eta). \tag{74}$$

There are several options to determine the phenomenological parameter η (scattering rate or inverse scattering time), for instance, by the Born approximation [229] or the self-consistent Born approximation [229,262,275,276,307–309] which will be discussed in Section 5.5.1. It implies that

$$C_0'(0,\omega+2i\eta) = -2\mathrm{Re}\left(\frac{1}{\pi(\omega+2i\eta)^2}\right) = -\frac{2}{\pi}\frac{\omega^2-4\eta^2}{(\omega^2+4\eta^2)^2}, \tag{75}$$

and with Equation (69) we obtain the following for the conductivity:

$$\sigma_{kk} \approx \frac{e^2}{\pi h}\frac{\omega^2(\omega^2-4\eta^2)}{(\omega^2+4\eta^2)^2}. \tag{76}$$

This is the well-known DC result $e^2/\pi h$ only when the scattering rate η is much smaller than the frequency, i.e. in the weak-disorder limit. The reason for this behavior is simply related to the fact that for any $\eta > 0$ the 2PGF decays exponentially on the scale $1/\eta$, always leading to a vanishing DC conductivity. It is not caused by Anderson localization but just by the incorrect evaluation of the

2PGF. This can be cured by introducing an accurate description of the average 2PGF in Equation (67) instead of the product of two averaged one-particle Green's functions.[10]

In the following we will discuss in more detail the effect of disorder on the transport properties, since this is important for applying the theory to the physics of realistic graphene samples. Moreover, in this field there are number of open questions which might be a challange for future studies.

5.4. *Perturbation theory for disorder*

The fact that for weak disorder (i.e. for $\eta \ll \omega$) the semiclassical approximation in Equation (76) gives reasonable values for the conductivity suggests that transport properties can be evaluated in terms of perturbation theory with respect to disorder. Since the scattering rate η vanishes with vanishing disorder, this quantity might also be available in perturbation theory. Here we use the low-energy Hamiltonian of Equation (56) and treat the random variables v_j as perturbations. A simple case is uncorrelated Gaussian randomness with zero mean and variance

$$\langle v_{jr} v_{j'r'} \rangle = g_j \delta_{jj'} \delta_{rr'} \quad (j = 0, \ldots, 3).$$

The perturbation theory is studied for a finite system of size L and a smallest scale l (e.g. lattice constant or mean free path). Then the change of the perturbed system under a change of the scale $\xi = \ln(L/l)$ can be calculated, for instance, in terms of a one-loop approximation. This perturbative renormalization group (PRG) has been employed for two-dimensional random Dirac fermions of Equation (56) in a large number of papers [298,310–312]. For instance, the solution of the PRG equations for a random gap ($g_3 > 0$, $g_0 = g_1 = g_2 = 0$) indicates that the variance of the random variable and its averaged value $m \equiv \langle m \rangle$ scale to zero, whereas the energy ϵ is running away on large scales ξ:

$$g_3(\xi) = \frac{g_3}{1 + (2g_3/\pi)\xi}, \quad m(\xi) = \frac{m_0}{\sqrt{1 + (2g_3/\pi)\xi}}, \quad \epsilon(\xi) = \epsilon_0 \sqrt{1 + (g_3/2\pi)\xi}. \tag{77}$$

Therefore, the one-loop PRG breaks down on a length scale

$$L_c \sim \mathrm{e}^{\pi/g_3} l, \tag{78}$$

which has also been discussed in the literature [299,313]. Nevertheless, the PRG result can give us some useful insight in the transport properties if we restrict the system to a size L smaller than L_c. For instance, the density of states is then obtained as [314]

$$\rho(E) \sim \frac{|E|}{2\pi} [1 + 2(g_3/\pi) \ln(L/l)].$$

Thus the density of states always vanishes linearly at the Dirac point $E = 0$, no matter how strong the disorder is. However, the slope of the linear behavior increases with system size L logarithmically. The normalization of the density of states implies that this one-loop result can only be valid for system sizes L up to L_c. It can be shown that this characteristic length scale, which appears here only as a limiting case for the

calculational method, also plays an important (physical) role for the scattering rate: The scattering rate vanishes for systems smaller than L_c.

Transport properties have been studied within this PRG scheme for all $g_j > 0$ [311]. The transport quantities can either be expressed in terms of the length scale L, like the density of states above, or in terms of the wavevector k, representing an inverse length scale. The wavevector is proportional to the energy and inversely proportional to the wavelength λ through the Dirac dispersion $E = v_F k \propto v_F \lambda^{-1}$. Therefore, the one-loop PRG breaks down for wavelengths larger than $\lambda \sim L_c$ which implies for energies E smaller than the critical energy scale

$$E_0 \sim \mathrm{e}^{-\pi/g_0} t,$$

where g_0 is the bare variance of the random scalar potential and t is the hopping rate. Then for $|E| \geq E_0$ the conductivity reads [311]

$$\sigma(E) = \frac{8e^2}{\pi h} \ln(|E|/E_0). \tag{79}$$

The diffusion coefficient D and the scattering rate η are

$$D = \frac{g_0'}{2\eta\pi} \ln(|E|/E_0), \quad \eta = \pi g_0' \rho(E),$$

where g_0' is essentially the variance of the random scalar potential g_0. These results satisfy the Einstein relation $\sigma \propto D\rho$.

The one-loop PRG calculation of random Dirac fermions was also extended to include Coulomb interaction [312]. These calculations indicate a run-away RG flow from the unperturbed fixed point. The search for new fixed points has not been successful yet. Earlier hopes that a specific conformal-invariant field theory could control all the physics of the random Dirac fermions near $E \sim 0$ have also not been fulfilled so far.

The perturbative approach can be extended by the summation over infinitely many subdiagrams for the 2PGF [315]. The result is known as weak localization and describes diffusion in disordered systems. A related idea is the $1/N$ expansion of the 2PGF [316]. This concept has also been applied to graphene [307]. It is a flexible approach that also allows us to study the effect of inter-valley scattering. According to the weak-localization studies by Suzuura and Ando [292], scattering between different valleys (i.e. different nodes of the low-energy spectrum) has a strong effect on the transport properties. The behavior changes from anti-localization, when only intra-valley scattering is included, to localization for inter-valley scattering. This means that, at least for weak disorder, the conductivity is reduced in comparison to the pure system. However, this does not necessarily mean that this type of disorder leads to Anderson localization.

A closer inspection of the weak-localization approaches reveals that these self-consistent results approaches have a deeper physical meaning, namely the appearance of diffusion due to spontaneous symmetry breaking. Therefore, it is easier to start directly from the symmetry analysis and to avoid the complicated diagrammatic calculations, as we will discussion in the next section.

The summation over infinitely many subdiagrams is not only useful for disorder but can also be applied to a perturbation theory for electron–electron [257] or to electron–phonon interaction [305]. It provides self-consistent equations of the Hartree–Fock–Bogoliubov type (i.e. it represents the best fit of the many-body problem by single-particle approximations). Such approximations usually lead to a gap opening, just as in the BCS theory, for arbitrarily weak interaction. It remains a question, however, whether these gaps are real or just artifacts of the single-particle approximation. This problem has been studied in great detail in the case of strongly correlated systems [317].

5.5. *Self-consistent approach: scattering rate and diffusion*

The evaluation of the scattering rate in the self-consistent Born approximation (SCBA) reads as the self-consistent equation

$$\eta = 2\mathrm{i}g(\langle\mathcal{H}\rangle + z + \mathrm{i}\eta)^{-1}_{rr}, \tag{80}$$

where η can be interpreted as the imaginary part of the self-energy (cf. [309]). A similar equation can be derived from the saddle-point approximation of the average 2PGF [296,318]. This approach avoids the unphysical behavior of the factorized 2PGF in Equation (75) for $\omega < 2\eta$. As a consequence, instead of the single scalar parameter η, the corresponding self-consistent equation determines a 4×4 matrix $\hat{Q}$:

$$\hat{Q} = g(\langle\hat{\mathcal{H}}\rangle + z - 2\gamma_j\hat{Q})^{-1}_{rr}\gamma_j, \tag{81}$$

where $\gamma_j = \mathrm{diag}(\sigma_j, \sigma_j)$, and $\hat{\mathcal{H}} = \mathrm{diag}(\mathcal{H}, \mathcal{H})$ is a 4×4 block diagonal Hamiltonian. $j=0$ is for a random scalar potential, $j=1, 2$ for a random vector potential and $j=3$ for a random gap potential. A special solution of Equation (81) could be of the form

$$\hat{Q}_0 = -\mathrm{i}\frac{\eta}{2}\gamma_j, \tag{82}$$

where η is the scattering rate, since it shifts the energy in the Green's function $(\langle\hat{\mathcal{H}}\rangle + z)^{-1}$ by $\mathrm{i}\eta$, like in the semiclassical approach of Section 5.3.2. Now we can insert our special solution in Equation (81) and multiply it by γ_j. This reduces the matrix equation to a scalar equation (80), the equation of the SCBA. It should be noticed that this equation is the same for all types of randomness, the model specific properties have dropped out. This is a first hint that the reduced equation is not sufficient to describe the physics of disordered monolayer graphene or bilayer graphene. The reason is that with the special ansatz (82) we have completely lost the 4×4 matrix structure of the equation. A more careful inspection of Equation (81) reveals that $\hat{\mathcal{H}}$ is invariant under a continuous transformation for $j=1,2,3$ (but not for $j=0$), depending on the type of randomness [296,318]. A consequence of these symmetries is that for $z=0$ the saddle-point equation is invariant under the global symmetry transformation, and the transformation creates a whole manifold of solutions $\hat{Q}$ with $\hat{Q}^2 = -\eta^2\gamma_0/4$ (γ_0 is the 4×4 unit matrix). This is the origin of the

nonlinear sigma model, which describes diffusion of particles. We will briefly return to this point in the discussion of the average 2PGF in Section 5.5.1.

It is crucial to notice that the manifold collapses to a single solution if $\eta = 0$. Such a vanishing solution exists, for instance, for a finite monolayer graphene if its linear size L is too small, namely $L < L_c$.[11]

5.5.1. *Scaling relation of the two-particle Green's function*

After integration over the manifold of saddle-point solutions, both for monolayer graphene and bilayer graphene, the average 2PGF

$$K_g(q,z) = \sum_r \mathrm{e}^{-\mathrm{i}q\cdot r} \lim_{\delta\to 0} \langle \mathrm{Tr}_2[G(r,0;-z/2-\mathrm{i}\delta)G(r,0;z/2+\mathrm{i}\delta)]\rangle,$$

which is related to $C(\epsilon,\omega)$ in Equation (67) for $\epsilon = 0$ by

$$C(0,\omega) = -\left[\frac{\partial^2 K_g(q,\omega)}{\partial q_k^2}\right]_{q=0},$$

can also be evaluated. For instance, for a random gap with variance g there is a simple relation between the 2PGF of the pure system

$$K_0(q,z) = \sum_r \mathrm{e}^{-\mathrm{i}q\cdot r} \lim_{\delta\to 0} \mathrm{Tr}_2[G_0(r,0;-z/2-\mathrm{i}\delta)G_0(r,0;z/2+\mathrm{i}\delta)],$$

with the one-particle Green's function $G_0(z) = (\langle\mathcal{H}\rangle + z)^{-1}$, and the average 2PGF as [318]

$$K_g(0,\omega) = \frac{(\omega+2\mathrm{i}\eta)^2}{\omega^2} K_0(0,\omega+2\mathrm{i}\eta) \equiv \omega^{-2} F(\omega+2\mathrm{i}\eta). \tag{83}$$

The right-hand side does not depend on the disorder strength g explicitly, only through the scattering rate η. This is a scaling relation for $K_g(0,\omega)$, where we have pulled out the divergent term ω^{-2} and introduced the scaling function $F(z) = z^2 K_0(0,z)$ with $z = \omega + 2\mathrm{i}\eta$. The expression for the conductivity in Equation (69) then reads

$$\sigma = -\frac{e^2}{2h} F'(\omega+2\mathrm{i}\eta), \tag{84}$$

where $F'(z)$ is the real part of $F(z)$. Thus, the conductivity depends only on the variable $\omega + 2\mathrm{i}\eta$ through the scaling function. This is a generalization of the classical Drude formula, where the scaling function of the latter would be $F_{\mathrm{Drude}} \propto i/z$.

The relation in Equation (83) can be compared with the semiclassical approximation in Equation (74). They do not agree except for the trivial case $\eta = 0$ due to the prefactor $(\omega+2\mathrm{i}\eta)^2/\omega^2$, obtained from the integration over the saddle-point manifold. For $\eta > 0$ it is important to notice that the average 2PGF always diverges like ω^{-2}, whereas the pure 2PGF is finite for $\eta > 0$. This cures the problem which we have had with the expression in Equation (76) if $\omega < \eta$.

5.6. *Numerical simulations*

Analytic calculations are limited because they are either based on a truncated perturbation series or they employ an approximative scheme. Therefore, it is important to use numerical calculations of finite systems as a complementary approach. There are a number of works in which the transport properties have been studied numerically, usually based on the transfer-matrix (or Landauer) approach [321,322]. An interesting result is that the conductivity increases with the system size in the presence of a single valley and potential disorder [323,324]:

$$\sigma(L) \sim \frac{2e^2}{h}\left[\sigma_0 + s\ln(L/\xi)\right], \tag{85}$$

with σ_0 and s of the order of unity. This logarithmic behavior agrees remarkably well with the one-loop PRG calculation in Equation (79). From the numerical results it is not clear whether or not the logarithmic increase of the conductivity saturates at some finite value, as it is suggested by the breakdown of the PRG, or increases asymptotically. Since it is obvious from the PRG that the behavior must change qualitatively beyond the scale L_c, it cannot be ruled out that this scale has not been reached in the numerical calculations.

In contrast to the growing behavior of the conductivity, a random gap term instead of the potential disorder gives a size-independent conductivity [325]

$$\sigma(L) = \frac{1}{\pi}\frac{e^2}{h}, \tag{86}$$

for any strength of the random gap fluctuations but with vanishing average gap. For any non-zero gap, however, the conductivity decays with increasing size L. Moreover, the conductivity increases with the strength of the random gap fluctuations for fixed L and fixed average gap. This indicates that the unusual behavior is not related to conventional Anderson localization, since for the latter we expect a decreasing localization length for increasing random fluctuations.

Additionally, Schomerus [326] considered the impact of the leads on transport through weakly doped graphene. He showed that graphitic leads and quantum wires give qualitatively the same transport properties, which can be characterized by a single parameter which is determined by the measurement of the conductance and shot noise of a rectangular undoped graphene strip. This duality is the result of the mode selection mechanism originating from the conical points of undoped graphene, and holds even though the different types of wire support different numbers of propagating modes.

5.7. *Metal–insulator transition*

Recent experiments on hydrogenated graphene (graphane) (Section 8.2.3) have revealed that a gap is opened by the adsorption of hydrogen such that graphene can undergo a transition from metallic to insulating behavior [280,288]. The gap opening by hydrogen adsorption is also supported by density-functional calculations [327]. An interesting question in this context is how the transport properties change when we add gradually hydrogen to graphene [280], creating randomly gaps in the

graphene sheet [140,185]. The random gap is characterized by two parameters, the average gap $\bar{m}$ and the variance g of the spatial gap fluctuations. If we begin with weak disorder, i.e. $\sqrt{g} \ll \bar{m}$, the minimal conductivity $\sigma_{\min}$ will be zero because there are either no states at the node $E=0$ or these states are localized. Thus the system is insulating with a vanishing conductivity at low temperatures. The spatial gap fluctuations around the mean value $\bar{m}$ have two effects: First, they can close the effective gap by broadening the particle and hole bands and, second, they can create new states inside the gap, such as midgap states [328–330]. Those states are either localized for large $\bar{m}$ (e.g. Lifshitz tails) [280,288,293] or delocalized for small $\bar{m}$ [318]. As we increase the spatial fluctuations of δm, local regions are formed in which $\delta m \approx 0$ with reasonable probability. Increasing g further, these local regions with $\delta m \approx 0$ start to form a percolating network. It is not necessary to close these gaps completely, since a local gap only reduces the local density of states. Therefore, a quantum percolation transition can take place in the presence of sufficiently large fluctuations of δm. This is similar to the percolating network picture of charged puddles [331]. A perturbative renormalization-group analysis supports such a transition indirectly. Starting from Equation (77), the term $\bar{m}$ always flows to zero under renormalization. The corresponding fixed point is a free massless Dirac Hamiltonian with DC conductivity $e^2/h\pi$. In other words, the system always flows to a clean metal for sufficiently large system size. However, this renormalization-group analysis is only valid for weak disorder. In case of strong disorder another behavior may appear in which the gap can survive.

More detailed analytic and numerical studies of the metal–insulator transition due to a random gap have revealed that for a vanishing average gap graphene is always metallic [318,325,332]. However, the situation is less clear for a nonzero $\bar{m}$. First, we have the result of the perturbative renormalization group that indicates a metallic behavior, at least for small g, and no metal–insulator transition. Moreover, the scaling relation of Equation (84) allows us to obtain the conductivity from the pure 2PGF, where the latter gives the scaling function as

$$F(z) = \frac{2a}{\pi} \frac{z^2}{\bar{m}^2 - z^2} \Theta(m_c^2 - \bar{m}^2)$$

with $a=1$ ($a=2$) for monolayer graphene (bilayer graphene). Thus the conductivity vanishes when the average gap $\bar{m}$ exceeds a critical value m_c. Here m_c depends on whether we consider monolayer graphene or bilayer graphene. Its value for a given variance g is much smaller for monolayer graphene than for bilayer graphene [318]:

$$m_c = \begin{cases} \dfrac{2}{l\sqrt{e^{2\pi/g} - 1}} \sim \dfrac{2e^{-\pi/g}}{l} & \text{(monolayer graphene)} \\ g/2 & \text{(bilayer graphene)} \end{cases}. \tag{87}$$

The scattering rate η is obtained from Equation (80) for both, monolayer graphene and bilayer graphene, as [318]:

$$\eta^2 = (m_c^2 - \bar{m}^2)\Theta(m_c^2 - \bar{m}^2)/4. \tag{88}$$

Inserting these results into the expression for the DC conductivity of Equation (84) gives us a simple power law

$$\sigma = \frac{a}{\pi}\frac{e^2}{h}\left(1 - \frac{\bar{m}^2}{m_c^2}\right)\Theta(m_c^2 - \bar{m}^2). \tag{89}$$

The factor $a = 2$ of the bilayer may be connected to the fact that the conductivity doubles for the bilayer graphene because of the two conducting sheets. However, in our approach it is related to spectral properties at low energies (linear vs. parabolic). Experiments do not show this doubling in the DC limit but indicate that the minimal conductivity of bilayer graphene is more sensitive to temperature (i.e. it increases strongly with temperature), whereas the minimal conductivity of monolayer graphene is almost independent of temperature [27] or changes linearly with T [26].

The results in Equations (87) and (88) indicate that the effect of disorder is much stronger in bilayer graphene. For monolayer graphene as well as for bilayer graphene, the critical gap value m_c increases with disorder. Thus, a random gap allows diffusive motion of the electrons, provided that the average gap is not too large. This reflects the percolation picture, as mentioned at the beginning of this section. The corresponding phase diagram includes two gapped phases (one for $\bar{m} > m_c$ and one for $\bar{m} < -m_c$) and an intermediate diffusive (metallic) phase with a nonzero minimal conductivity $\sigma_{\min}$ [318] (cf. Figure 60). These results are in qualitative agreement with the numerical simulations for related network models by Cho and Fisher [333] and by Chalker *et al.* [334]. However, more recent numerical simulations by Bardarson *et al.* [325] have questioned the power law in Equation (89) for monolayer graphene: although the prefactor $e^2/\pi h$ agrees very well, the critical value m_c is smaller than the one calculated in Equation (87). Since the latter is a result for an infinite graphene sample, we have also calculated m_c for finite samples and found qualitatively the same finite-size behavior such as the decay of $\sigma(L)$ with increasing size L [332]. Nevertheless, the actual value of m_c for different types disorder remains an open problem. Moreover, the simple power law in Equation (89) may have a different exponent because the self-consistent evaluation of the

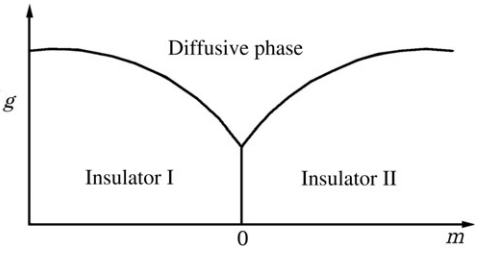

Figure 60. Schematic phase diagram of random-gap Dirac fermions (monolayer graphene) for average gap $\bar{m}$ and disorder strength g, obtained from numerical and analytic calculations [318,325,333,334]. There are two gapped phases for $m < -m_c$ and for $m > m_c$ with an intermediate metallic phase. According to Equation (87) the vertical line has a width of $2m_c = 2e^{-\pi/g}$ which is too small to be visible in this plot. The metallic phase for large g has not been observed in recent numerical simulations [325] because m_c was smaller than the value obtained in Equation (87).